Chem Soc Rev

ROYAL SOCIETY OF CHEMISTRY

REVIEW ARTICLE

View Article Online
View Journal | View Issue

Cite this: *Chem. Soc. Rev.*, 2025, **54**, 6652

Bridging the molecular mechanism and industrial process of zeolite-catalyzed methanol conversion to olefins and ethanol using advanced solid-state NMR spectroscopy†

Jing Niu,‡[ab] Xinzhi Ding,‡[abc] Shutao Xu,*[abc] Yingxu Wei[abc] and Zhongmin Liu*[abc]

Received 31st March 2025

DOI: 10.1039/d5cs00341e

rsc.li/chem-soc-rev

Zeolite-catalyzed methanol-to-olefin (MTO) and methanol-to-ethanol (MTE) reactions have achieved significant breakthroughs in both industry and academia, proving to be mature alternative pathways for producing basic chemicals from non-oil resources. The successful transition of these catalytic processes from laboratory to industrial implementation has been propelled by fundamental breakthroughs in the comprehensive understanding of reaction mechanisms. In this context, solid-state nuclear magnetic resonance (ssNMR) spectroscopy has emerged as an indispensable tool for elucidating catalyst structures, catalytic reaction mechanisms, and the interactions and dynamics of reactant molecules in these industrially important processes. This review specifically focuses on the application of ssNMR spectroscopy in industrially mature MTO and dimethyl ether (DME) carbonylation processes, which serve as representative examples of zeolite-catalyzed industrial processes. Based on this molecular-level information from spectroscopic observations combined with theoretical methods, this review aims to bridge the fundamental understandings of reaction mechanisms with practical applications, including the rationalization of catalysts, the optimization of catalytic performance, and the improvement of industrial processes.

---

[a] *National Engineering Research Center of Lower-Carbon Catalysis Technology, Dalian Institute of Chemical Physics, Chinese Academy of Sciences, Dalian 116023, China. E-mail: xushutao@dicp.ac.cn, liuzm@dicp.ac.cn*

[b] *State Key Laboratory of Catalysis, Dalian Institute of Chemical Physics, Chinese Academy of Sciences, Dalian 116023, China*

[c] *University of Chinese Academy of Sciences, Beijing 100049, China*

† Electronic supplementary information (ESI) available. See DOI: https://doi.org/10.1039/d5cs00341e

‡ Jing Niu and Xinzhi Ding contributed equally to this work.

Jing Niu

Jing Niu obtained her PhD in Chemistry from Lanzhou University in 2023 under the supervision of Prof. Wei Wang. She subsequently joined the research team of Prof. Zhongmin Liu under the guidance of Prof. Shutao Xu at the Dalian Institute of Chemical Physics (DICP), Chinese Academy of Sciences (CAS), as a postdoctoral researcher. Her research interests focus on elucidating the reaction mechanisms of zeolite-catalyzed processes through advanced Nuclear Magnetic Resonance Spectroscopy (ssNMR), with emphasis on alcohol conversion pathways over acidic zeolites.

Xinzhi Ding

Xinzhi Ding is currently pursuing her PhD at the Dalian Institute of Chemical Physics (DICP), Chinese Academy of Sciences (CAS), under the supervision of Prof. Shutao Xu. Her research interests focus on applying advanced Nuclear Magnetic Resonance Spectroscopy (ssNMR) methods to investigate the reaction mechanisms in zeolite catalysis.

1. Introduction

Zeolites are essential catalysts in the petrochemical industry due to their highly ordered framework structures, well-defined micropores, tunable acidic properties, excellent thermal and hydrothermal stabilities, and unique shape-selective properties arising from the structure confinement effect.[1–7] In light of the diminishing availability of petroleum and severe environmental pollution issues, the conversion of one-carbon (C1) molecules (representative as methanol, carbon monoxide, carbon dioxide, and methane) into value-added chemicals and fuels has garnered significant attention in both industry and academia.[4,8–14] As proposed by George A. Olah,[15] methanol, which can be manufactured from a variety of non-oil resources, including coal, natural gas, organic waste, biomass, and even renewable CO_2 sources, offers a viable alternative to petroleum in the chemical industry.[16] It serves as a bridge between current fossil resource-based economic systems and future renewable energy frameworks (Fig. 1). As a platform chemical, methanol can be converted into a wide range of derivatives, such as acid-catalyzed generation of hydrocarbons (MTHs),[17–19] specifically olefins (MTOs),[19–24] gasoline (MTG),[25] aromatics (MTAs),[26,27] and ethanol (MTE)[28–31] *via* carbonylation and hydrogenation.

In particular, zeolite-catalyzed MTO and MTE processes have been industrially commercialized, with large-scale production occurring in commercial plants in China in recent years. Typical techniques were developed by the Dalian Institute of Chemical Physics (DICP), including the fluidized-bed DMTO process and the fixed-bed DMTE process, using methanol originating from coal as the raw material. Thus far, DMTO technology has evolved through three generations and has been licensed for 36 commercial units. Among these, 18 licensed units have commenced commercial-scale MTO operations, delivering a total olefin output exceeding 13 Mt a^{-1}. Here, it is particularly necessary to provide a brief introduction to the DMTE process. The DMTE process involves the dehydration of methanol to produce dimethyl ether (DME), followed by the carbonylation of DME with carbon monoxide over the H-MOR zeolite to generate methyl acetate (MA), which is subsequently hydrogenated to yield ethanol. Thus far, DMTE technology has been licensed for 14 commercial units, with an annual ethanol production capacity of 4.55 Mt a^{-1}. Since the core reaction of the DMTE process is the carbonylation of DME on the H-MOR zeolite, we focus on elucidating this key reaction mechanism within the MTE process. Notably, DME carbonylation discussed here specifically refers to the zeolite-catalyzed DME carbonylation. This industrialization not only develops novel, efficient pathways for the oriented production of fuels and chemicals,

Shutao Xu

Shutao Xu received his PhD from the Dalian Institute of Chemical Physics (DICP), Chinese Academy of Sciences (CAS), in 2011. He then joined Prof. Zhongmin Liu's team at the National Engineering Research Center of Lower-Carbon Catalysis Technology, DICP, as a research assistant. He became a professor in 2017. His research interests are the development of various solid-state Nuclear Magnetic Resonance Spectroscopy (ssNMR) methods including in situ/operando techniques, 2D ssNMR spectroscopy, Hyperpolarized (HP) ^{129}Xe MRI and Pulse Field Gradient (PFG) NMR, as well as applying these advanced NMR methods to the study of the structure, acidity and reaction mechanism of catalytic materials.

Yingxu Wei

Yingxu Wei received her PhD from the Dalian Institute of Chemical Physics (DICP), Chinese Academy of Sciences (CAS), in 2001. During her service at the DICP, she conducted a postdoctoral study at the University of Namur (Belgium) from 2003 to 2004. She has been the group leader of Catalysis and New Catalytic Reactions in National Engineering Laboratory for Methanol to Olefins since 2009 and was promoted to professor in 2011. Over the years, Prof. Wei has undertaken a number of key academic research projects commissioned by NSFC, CAS, MOST, PetroChina and other organizations. Over 100 academic papers have been published and more than 60 patents have been applied and granted.

Zhongmin Liu

Prof. Zhongmin Liu is the Director of the Dalian Institute of Chemical Physics (DICP), Chinese Academy of Sciences (CAS), since 2017. He has long been working with the catalysis research, process development, and technology transfer in energy conversion and utilization, and made significant achievements. Prof. Liu led his team to successfully commercialize two of the most representative industrial processes, methanol to olefins (MTO) and methanol to ethanol (MTE), in 2010 and 2017, respectively, which are important advances in the conversion of coal to chemicals. He has published more than 430 research papers and got 600 authorized patents or more.

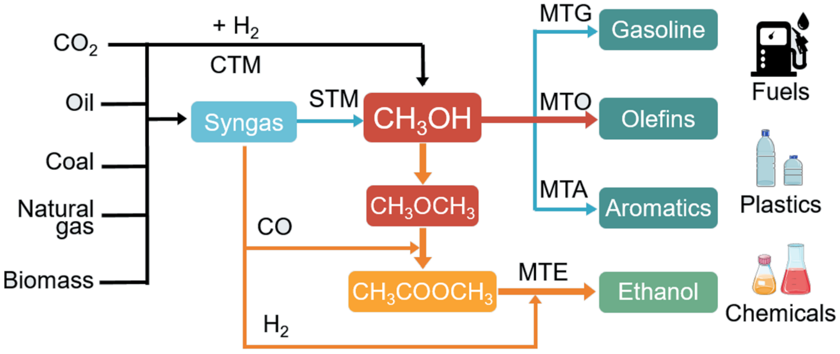

Fig. 1 Schematic of the technical roadmap for methanol conversion processes.

but also provides typical examples of heterogeneous catalysis systems that involve complex multi-step reactions catalyzed by zeolite acidic sites within confined pores or cavities. Despite this progress, the relationship between MTO and DME carbonylation reactions remains underexplored. Notably, both MTO and MTE reactions are based on the same precursors, methanol or methanol-derived DME, but differ in catalysts (MTO: SAPO-34 *vs.* MTE: MOR) and operating conditions (temperature, pressure, and process techniques). In both reactions, the evolution of surface methoxy species (SMS) is crucial for the coupling of C–C bonds for the upgrade of the products. Specifically, in DME carbonylation reactions, the incorporation of CO into the C–O bond of SMS (a process known as the Koch-carbonylation) is proposed as the key step in the initial C–C bond formation in MTO reactions.[32,33] However, the MTO reaction was considered as a side reaction that mainly contributes to the catalyst deactivation in DME carbonylation.[34,35] Therefore, understanding the fundamental mechanisms of these two methanol-mediated reactions is critical for designing of high-performance catalysts, improving heterogeneous catalysis efficiency, advancing industrial applications, and enriching catalytic theories in the field of zeolites.

Significant progress has been made in elucidating the molecular mechanisms of these catalytic reactions, driven by the unprecedented development of *in situ*/*operando* characterization techniques, including X-ray diffraction analyses, imaging techniques, infrared spectroscopy, and solid-state nuclear magnetic resonance (ssNMR).[36–38] Among various characterization techniques, ssNMR spectroscopy is a routine and powerful tool for characterizing both zeolite frameworks (primarily containing ^{29}Si, ^{27}Al, and ^{17}O, with surface hydroxyl groups represented by ^{1}H,) and organic reactants (predominantly composed of ^{1}H and ^{13}C) on zeolite catalysts. SsNMR spectroscopy provides comprehensive insights into catalytic processes by offering accurate characterization of catalyst structure and acidity, *in situ* monitoring of the dynamic reaction processes, atomic-level measurement of both weak and strong interactions, and determination of diffusion properties of zeolites.[39–41]

This review focuses on MTO and DME carbonylation reaction, aiming to bridge the gap between the fundamental mechanistic insights and industrial advancements in catalytic process development. Over the past decade, several excellent reviews on the MTO process have highlighted key topics, including industrial process development,[21,42] catalyst synthesis,[21,22,43] reaction mechanisms (such as shape selectivity, and catalyst deactivation),[17–19,32,35,44–48] through the integration of experimental methods with quantum chemistry and molecular dynamics simulations. However, a critical gap persists in the literatures: systematic reviews that bridge molecular-scale reaction mechanisms and industrial process optimization remain notably absent. This critical gap significantly diminishes the engagement of applied researchers and industrial practitioners who seek actionable guidance from fundamental studies. Several reviews have attempted to link fundamental research with catalyst design and MTO performance. For instance, the seminal review by Weckhuysen and Gascon[19] summarized the mechanistic insights into MTH and promoted the rational design of catalysts based on these insights. Additionally, contributions from Deng,[40,41,49,50] Ivanova,[51,52] Hou,[39] Ramamoorthy,[53] and Kong[54] have systematically reviewed their development and application in ssNMR spectroscopy, focusing on technical advancements, structural and acidic characterization of zeolites, synthesis/crystallization mechanisms, host–guest interactions, and reaction mechanisms in zeolite-catalyzed processes. While these reviews offer valuable insights into mechanistic understanding through spectroscopic techniques, opportunities remain to further clarify their translational relevance for guiding industrial process optimization strategies. Two perspectives from our group in 2015[20] and 2025[55] historically traced the transition of laboratory-scale research into commercial technology in DICP and elucidated fundamental chemical issues concerning the essence of the dynamic evolution of the MTO reaction and the cross-talk mechanisms among diffusion, reaction, and catalyst (coke modification), which are crucial for technology development and process optimization. However, the systematic use of *in situ* spectroscopy to obtain molecular-scale mechanistic insights and their connection to practical industrial processes has not been thoroughly elaborated. Moreover, comprehensive reviews on the mechanistic understanding of the carbonylation of DME over zeolites, particularly concerning catalyst design and industrial process optimization, remain scarce.[29,31] Notably, the inherent correlation between the catalytic mechanisms of MTO and DME carbonylation has yet to be thoroughly explored. The ultimate goal in catalysis is correlating these mechanistic insights with practical applications such as catalyst design and process engineering. Over the past decade, substantial progress has been achieved in both fundamental research and industrial process development of MTO and MTE, alongside the advancements in advanced ssNMR spectroscopy. A systematic review integrating these fundamental and applied advances is therefore critically needed to bridge mechanistic insights with industrial implementation and inspire future innovations.

In this review, we specifically focus on the role of ssNMR spectroscopy in the industrially mature MTO and DME carbonylation processes, both of which represent important hydrocarbon conversion processes involving comprehensive acid-catalyzed mechanisms. Taking account of the rapid advancements in both MTO and DME carbonylation processes, it is essential to review the achievements covering the full spectrum of research in this field in the last decade. In industrial processes, ssNMR has been proven invaluable for characterizing zeolite structures and acidity, elucidating reaction mechanisms, and bridging the gap between fundamental research and industrial development. To achieve this aim, this review begins with a summary of recent advancements in ssNMR techniques applied to zeolite-catalyzed reactions in Section 2. Building on these insights, we review the application of advanced ssNMR techniques in MTO and DME carbonylation reactions in Sections 3 and 4, and discuss how these fundamental understandings are associated with the industrial process. Finally, Section 5 emphasizes the current challenges and further perspectives for broader applications of ssNMR in zeolite-catalyzed processes. We anticipate this review will establish a methodological framework, bridging advanced characterization techniques with practical implementations in heterogeneous catalysis, while propelling the innovation of zeolite materials.

2. Advanced solid-state NMR techniques

SsNMR has proven indispensable for characterizing catalysts and probing reaction mechanisms in heterogeneous catalysis. This technique uniquely deciphers atomic-level structural features including local coordination environments, intermolecular interactions, and molecular dynamics through simultaneous detection of nuclear chemical environments in both catalysts and adsorbed species, while establishing critical spatial correlations between nuclei. Because of the dynamic nature of catalytic reactions, it is critical to develop *in situ* techniques that enable monitoring of the catalyst structure and reaction process and observing the intermediates under working conditions. The development of ssNMR techniques has been extensively documented in excellent research articles, reviews, and books, which provide a comprehensive introduction to the basic theories, novel methods, and applications in the characterization of catalytic materials and reaction mechanisms.[40,41,49–51,53,56,57] In this section, we briefly summarize the widely used methods in the study of the zeolite-catalyzed methanol conversion process.

2.1. *In situ* ssNMR techniques

The *in situ* ssNMR technique has become a pivotal tool for investigating catalytic reaction mechanisms due to the ability of real-time observation of catalytic reactions under working conditions, capturing intermediates and elucidating the dynamic interactions among catalysts, reactants, intermediates, and products at the molecular level.[58] To address varying operational requirements, two specialized *in situ* magic angle spinning (MAS) NMR configurations have been established: (1) batch-like conditions for closed-system analyses and (2) continuous-flow conditions for real-flow system analyses (Fig. 2).

Under batch-like conditions, glass ampoules or gas-tight rotors were designed as microreactors that allow direct loading and sealing of catalysts and reactants under vacuum and avoid exposure to external environments. These microreactors can withstand high pressures up to 22.5 MPa and a wide range of temperatures from 273 to 973 K.[59] The evolution of the batch-like mode in ssNMR techniques has progressively narrowed the gap between laboratory analysis and industrial reaction

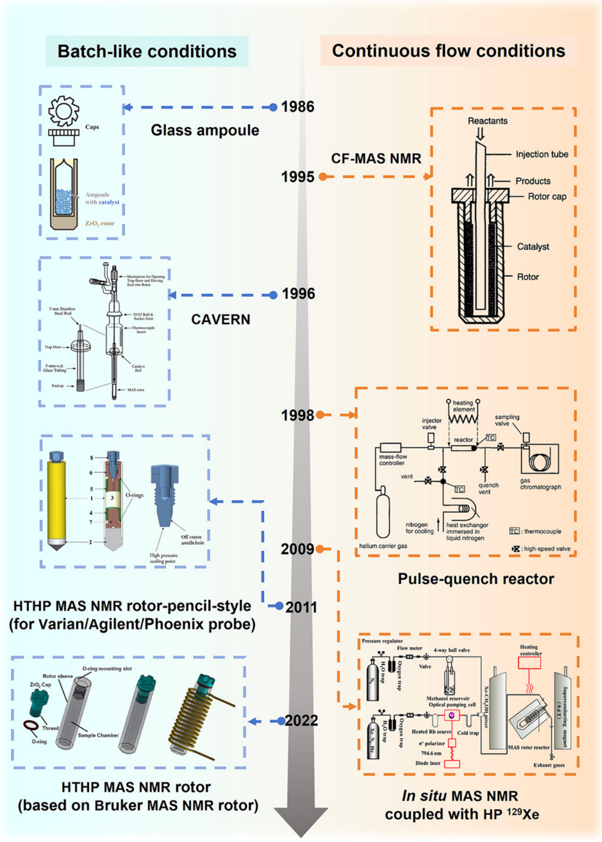

Fig. 2 Historical timeline of *in situ* ssNMR techniques. HTHP denotes high temperature high pressure. Reproduced with permission from ref. 50, 61, 62, 68, 71, 74 and 77. Copyright 2023 Elsevier, 1997 Springer Nature, 2011 Elsevier, 2023 American Chemical Society, 1998 John Wiley and Sons, 1995 Royal Society of Chemistry and 2009 American Chemical Society.

conditions through iterative technological advancements, as evidenced by the capability to achieve harsher reaction conditions involving higher temperatures and pressures. Early methods involving glass ampoule sealing and liquid nitrogen quenching had both advantages and limitations. While commercially available equipment and inserts facilitated the process, and a major drawback was the inability to add reactants or extract products after sealing.[60] Haw *et al.*[61] introduced a major advancement by developing the cryogenic adsorption vessel enabling rotor nestling (CAVERN) system, which facilitated direct *in situ* encapsulation of catalysts and reactants. This innovative design enabled real-time spectral dynamics to be monitored during temperature variations using a variable temperature (VT) probe, although its application remained restricted to ambient-pressure conditions. To meet the pressurization requirements, the modular high-pressure rotor system developed by Hu and collaborators[62–64] achieved controlled pressures of 15–20 MPa through specialized loading chambers and valves. The geometric optimization of plastic valve adapters enhanced pressure tolerance; however, high-temperature sealing continued to depend on adhesives and PEEK materials. Subsequent advancements in materials and component design further enhanced the capability to achieve higher temperatures and pressures. Notable developments include MACOR ceramic-threaded rotors and WHiMS (based on the initials of its designers, Walter, Hoyt, Mehta, and Sears) rotors,[65,66] which enabled breakthroughs in reaction temperature and pressure control (MACOR: 403 K, 1 MPa; WHiMS: 523 K, 22.5 MPa). However, these rotors were only compatible with Varian, Agilent, and Phoenix probes. To overcome this limitation, Zhao and Hou *et al.*[67] developed a rotor specifically designed for Bruker commercial probes. By integrating screw threads onto the ZrO_2 drive cap with a minimal length, the team employed extremely high-precision machining techniques to ensure the high coaxiality for high-speed spinning. The rotor, constructed entirely from ZrO_2 ceramic except for the sealing O-rings, achieves a spinning rate exceeding 8 kHz. By using perfluoro elastomer O-rings, it withstands sealing temperatures up to 523 K and pressures up to 10 MPa. These rotors have been successfully applied to mechanism studies of methanol reforming[68] and syngas conversion.[69,70] Batch-like *in situ* techniques have been extensively applied in studying the mechanism of methanol conversion over zeolite catalysts, facilitating the detection of reaction intermediates, identification of products, and analysis of host–guest interactions. However, these methods remain limited in resolving the initial adsorbing and activating processes of reactants, as well as the characterization of intermediate species under reaction conditions.

Since the pioneering development of the pulsed-quench flow reactor by the research team led by Haw in 1998,[71] *in situ* ssNMR catalysis research has undergone significant technological advancements. The proposed three-step methodology, involving helium-purged catalyst activation, pulsed reactant injection, and millisecond-scale liquid nitrogen quenching ($\Delta t < 200$ ms), enabled rapid thermal quenching from reaction temperatures exceeding 573 K to ambient conditions. This "chemical snap-freeze" technique facilitated the first successful room-temperature capture of high-temperature surface intermediates, such as metal carbene species and protonated cyclic intermediates, providing crucial spectroscopic evidence for elucidating C–H activation mechanisms.[72] Recently, it has also been applied in high-pressure systems to study the mechanism of syngas conversion.[73] Hunger *et al.*[74] modified a commercial Bruker 7 mm MAS NMR probe to develop a continuous-flow magic-angle spinning NMR (CF MAS NMR) microreactor system with structural innovations. The design utilizes a glass tube axially positioned in the MAS rotor, through which reactants are carried by gas flow through the catalyst bed (bottom-to-top direction) and exit *via* an annular gap in the rotor cap. This *in situ* flow technology enables multidimensional characterization when coupled with UV-Vis spectroscopy[75] and gas chromatography (GC).[76] In addition, integration with laser-hyperpolarized ^{129}Xe NMR[77] techniques significantly enhances sensitivity and reduces acquisition time. The CF MAS NMR system has been instrumental in studying methanol adsorption on zeolites and the formation/transformation of methoxy species. However, its open-channel design limits operation to ambient pressure, which is inadequate for higher pressure processes such as DME carbonylation, requiring pressures above ambient pressure. Notably, pressure variations significantly affect methanol conversion mechanisms. Additionally, the high cost of isotopic reagents imposes a financial burden on labelling strategies. Both batch-like and continuous-flow conditions provide complementary mechanistic insights, as demonstrated in studies of MTO and DME carbonylation reactions.[59,78,79]

2.2. Signal enhancement

Due to the inherently limited sensitivity arising from the small population differences in the Boltzmann distribution of nuclear spins under thermal equilibrium, signal enhancement has been a longstanding objective to expand the scope of NMR applications. NMR sensitivity depends on the strength of the magnetic field and the intrinsic properties of nuclei, including the gyromagnetic ratio (γ) and spin quantum number (I). While employing high-field superconducting magnets (*e.g.*, $\geq$14.1 T) and cryogenic probe technology are straightforward methods to enhance the NMR sensitivity, these hardware-based approaches encounter practical limitations due to the bottleneck of superconducting magnetic field strength and high cost. Due to the low natural abundance of ^{13}C nuclei (1.1%), which is crucial for studying reactant molecules in catalytic reactions, isotope labelling is essential for detecting low-concentration species. Additionally, cross polarisation (CP) is widely used to enhance the ^{13}C signal sensitivity by dipolar coupling, transferring magnetization from an abundant nucleus with a high gyromagnetic ratio (such as ^{1}H, ^{19}F) to a less abundant ^{13}C nucleus and theoretically achieving 4-fold signal enhancement. For quadrupolar nuclei in zeolite frameworks (*i.e.*, ^{27}Al: $I = 5/2$; ^{23}Na: $I = 3/2$; and ^{17}O: $I = 5/2$), optimal spectral resolution requires high-field operation ($\geq$14.1 T) to minimize second-order quadrupolar broadening and two-dimensional correlation spectroscopy (*e.g.*, MQMAS and STMAS) to separate isotropic/anisotropic spectral dimensions.[80,81]

The development of hyperpolarization techniques, especially dynamic nuclear polarization (DNP), has effectively enhanced the NMR sensitivity by several orders of magnitude.[82–86] DNP enhances the NMR sensitivity by transferring the large polarization of unpaired electrons or paramagnetic ions to coupled nuclei through the solid effect or cross-effect mechanism, yielding a theoretical enhancement at a maximum fold of 658 for ^{1}H and 2617 for ^{13}C under optimal conditions.[87–91] In a typical DNP experiment for porous solids under MAS conditions, the samples are impregnated with a radical solution to transfer the polarization from radicals and ^{1}H from solvents to solid surfaces (Fig. 3a). The application of DNP in solids has achieved robust sensitivity and resolution for nuclei such as ^{13}C, ^{29}Si, ^{27}Al, and ^{17}O. This enhancement enables the rapid acquisition of two-dimensional (2D) correlation spectra within reasonable timeframes. As a result, DNP-enhanced ssNMR has found widespread applications in precise spatial distribution measurements, elucidation of interfacial structures and surface functionalization, identification of intermediates on surfaces, and detection of weak interactions in solid materials.[92–98] Specifically, the application of DNP facilitates the direct identification of carbenium ions and spatial distribution of hydrocarbons in the MTO reaction.[94,95,99,100] Another hyperpolarization technique employs laser-driven spin-exchange optical pumping (SEOP) to achieve nuclear spin polarization enhancement, particularly for ^{129}Xe nuclei. This methodology typically utilizes a gas mixture composition of Xe (1%), N_2 (1%), and He (98%), where helium acts as both a buffer gas and a thermal transport medium during the optical pumping process.[101–104] In the hyperpolarized (HP) ^{129}Xe NMR method, vaporized Rb is irradiated in a magnetic field by a polarized light, generating polarized Rb spin population (Fig. 3b). This polarization is further transferred to ^{129}Xe atoms through electron-nuclear hyperfine interactions, achieving xenon polarization beyond Boltzmann distribution at 298 K. The (HP) ^{129}Xe NMR exhibits high sensitivity to the local environment arising from its large electron cloud, making (HP) ^{129}Xe NMR widely used to probe the pore structure, pore connectivity, and local chemical environments in the evolution of methanol under flow conditions.[105–108]

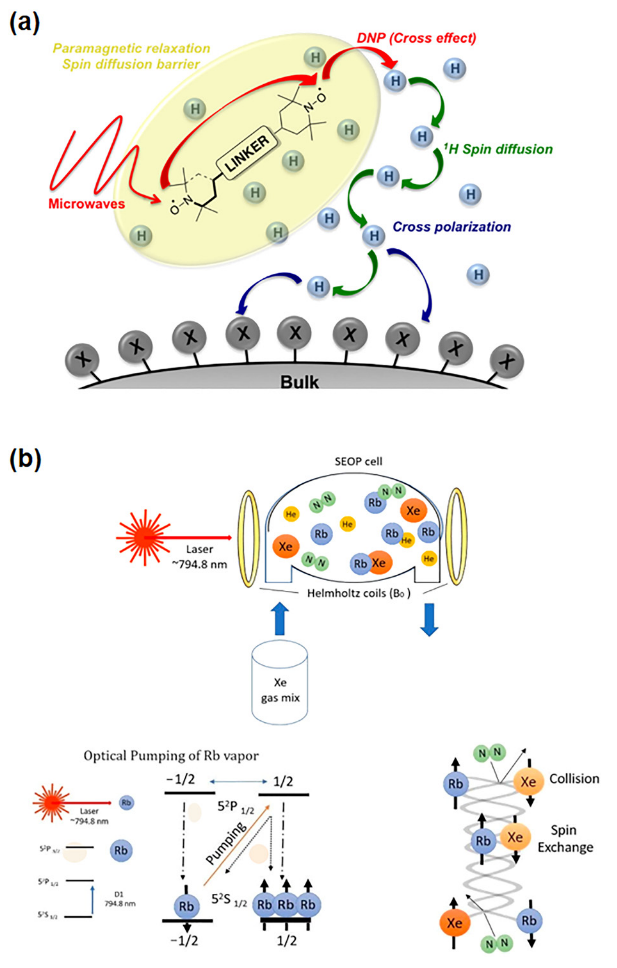

Fig. 3 Schematic of the hyperpolarization technique. (a) Schematic of polarization transfer for cross-effect DNP (SENS). Reproduced with permission from ref. 88. Copyright 2018 Elsevier. (b) Schematic of a hyperpolarized ^{129}Xe production system: spin-exchange optical pumping (SEOP) setup using a high-power semiconductor laser and optical pumping cell with gas mixture of Xe, He, and N_2. Reproduced with permission from ref. 102. Copyright 2024 MDPI.

2.3. SsNMR correlation spectroscopy

SsNMR correlation spectroscopy, which establishes proximity and connectivity between the homonuclear and heteronuclear nuclei *via* dipolar or *J* coupling interactions, has been widely employed in structural determination, species identification, interaction characterization, and dynamic analysis in materials science.[41,109] Unlike liquid-state NMR, ssNMR requires MAS to overcome anisotropic line broadening from interactions like chemical shift anisotropy, dipolar couplings and quadrupolar couplings. Dipolar interactions, arising from through-space interactions between nuclear spins with spatial proximity, are central to ssNMR. To probe these interactions, dipolar recoupling techniques are applied using specific radiofrequency pulse sequences synchronized with the spinning frequency. These sequences effectively reintroduce dipolar couplings, allowing probing molecular structure and dynamics while maintaining high spectral resolution.[110–113] Notably, the dipolar coupling constant (*D*) exhibits an inverse cubic dependence on internuclear distance, enabling precise quantification of atomic spatial proximity and distances. Complementing the through-space interactions, the scalar *J*-coupling interaction mediated by chemical bond electrons manifests between nuclei connected *via* 1–3 covalent bonds, with coupling constants spanning 1–200 Hz.[114] Analogues to liquid-state NMR, advanced methods are employed to probe the internuclear bond connectivity of nuclei, particularly for spin-1/2 nuclei (*e.g.*, ^{29}Si and ^{13}C).

The correlation experiments are classified as either homonuclear or heteronuclear, depending on the observation of the nuclei. Both types have been extensively used in studying the catalytic mechanism and in determining the precise structure

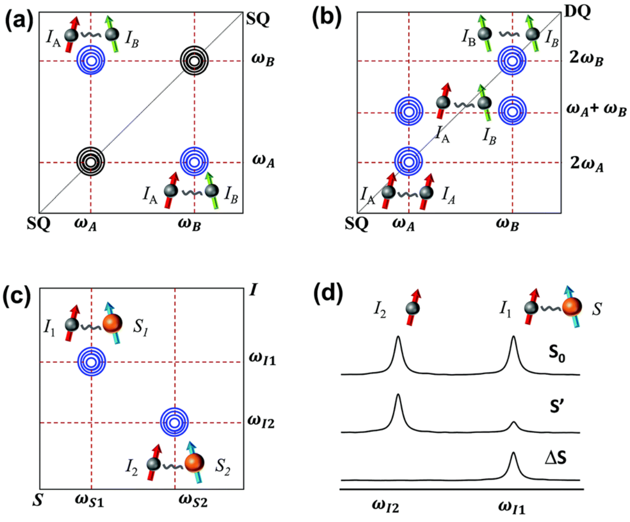

Fig. 4 Schematics of 2D SQ–SQ (a) and DQ–SQ (b) homonuclear MAS NMR spectra, a 2D HETCOR MAS NMR spectrum (c) and a 1D REDOR-like double-resonance MAS NMR spectra (d). Reproduced with permission from ref. 41. Copyright 2021 Royal Society of Chemistry.

of zeolites in MTO and MTE reactions. To provide direct information on selecting the appropriate sequences, this review briefly introduces commonly used methods in methanol conversion, while comprehensive principles of these techniques can be found in relevant reviews.[41,53,111,115,116] Homonuclear correlation experiments are driven by second-order recoupling sequences such as proton-driven spin diffusion (PDSD),[117] combined $R2_n^v$-driven (CORD),[113] phase-alternated recoupling irradiation scheme (PARIS),[118] and long-range spatial proximity information for different carbon atoms *via* single quantum (SQ) correlation (Fig. 4a). These experiments have been utilized to investigate the spatial proximity between various active species/intermediates involved in the conversion of ^{13}C-methanol.[119–121] In 2D double quantum-single quantum (DQ–SQ) MAS NMR correlation spectra (Fig. 4b), the chemical shifts of correlation signals in the DQ dimension correspond to the sum of two signals in the SQ dimension, thereby mitigating the intense diagonal background observed in the SQ correlation spectra. Moreover, the distance between adjacent same nuclei can be quantitatively measured by varying the recoupling time in DQ experiments. DQ correlation experiments have been extensively used to investigate acid site proximity and defect sites (*e.g.*, ^{1}H–^{1}H), accurately identify Al distributions (*e.g.*, ^{1}H–^{1}H and ^{27}Al–^{27}Al), and analyze framework connection (*e.g.*, ^{29}Si–^{29}Si) in zeolites.[122–130] Additionally, for ^{13}C–^{13}C DQ, the through-bond INADEQUATE (incredible natural abundance double quantum transfer experiment) method is used for the identification of the bond connectivity of organic intermediates.[131]

Heteronuclear correlation (HETCOR) MAS NMR experiments are valuable for probing spatial proximity and bond connectivity between different nuclei, *e.g.*, ^{1}H–^{13}C, ^{23}Na–^{27}Al, ^{31}P–^{27}Al, and ^{27}Al–^{31}P depending on whether CP-based, *J*-based, or dipole-based sequences are employed. CP-based schemes are routine methods for investigating spatial proximity between an abundant spin and a dilute spin (Fig. 4c), playing a crucial role in identifying the structure and in probing host–guest interaction between organic intermediates and zeolite frameworks. For spin-1/2 nuclei with large chemical shift anisotropy and for quadrupolar nuclei, refocused insensitive nuclei enhanced by polarization transfer (RINEPT)[132,133] and dipolar-based heteronuclear multiquantum coherence (D-HMQC)[134] MAS NMR experiments are preferred for obtaining through-space information between distant nuclei, and have been applied to investigate the structure of active sites and host–guest information in zeolites. It should be emphasized that INEPT and HMQC can be adapted to probe both through-space (D-INEPT and D-HMQC) and through-bond (*J*-RINEPT and *J*-HMQC) correlations by facilitating magnetization transfer *via* dipolar and *J*-coupling interactions, respectively.[135–137] Additionally, rotational-echo double resonance (REDOR)[138] is widely used for quantitatively measuring dipole interactions between two heteronuclear spins, evidenced by a significant dipolar dephasing in signal intensity, described by the $\Delta S/S_0$ value (defined as $(S_0 - S)/S_0$, where S and S_0 correspond to the signal intensity with and without dipolar dephasing, respectively) (Fig. 4d). For instance, DNP-enhanced ^{29}Si–^{13}C REDOR experiments have been employed to determine host–guest interactions between Si atoms in zeolites and C atoms in organic species by assessing the spatial proximities.[95] For half-integer quadrupolar spins (*e.g.*, ^{1}H–^{27}Al and ^{13}C–^{27}Al), techniques such as TRAPDOR (transfer of population in double resonance),[139] REAPDOR (rotational echo adiabatic passage double resonance),[140,141] and resonance-echo saturation-pulse double resonance (RESPDOR)[142,143] are more efficient for determining the spatial proximity and internuclear distance.

2.4. Diffusion

(HP) ^{129}Xe NMR and pulsed field gradient (PFG) NMR methods are powerful techniques for probing structure–adsorption–diffusion–reaction relationships in zeolite catalysis.[144,145] PFG NMR employs pulsed magnetic field gradients to spatially label nuclear spins, enabling direct observation of guest molecule diffusion within porous materials.[146] This technique quantifies the mass transfer of guest molecules within the crystal at micrometer spatial and millisecond temporal resolutions. With the combination of complementary HP ^{129}Xe NMR spectroscopy, these techniques have been applied to reveal atomic-scale adsorption heterogeneity and structural features in zeolitic materials.[106,147,148] Based on PFG NMR, molecular dynamics (MD) simulations provide microscopic-level insights into diffusion mechanisms, including diffusion pathways, energy barriers, collision frequencies, and even anomalous diffusion phenomena.[149–152] For instance, Zheng *et al.*[151] were the first to report the anomalous diffusion behavior of long-chain molecules, where their movement slows down with the increase in temperature under confinement. Using MD simulations and their self-developed and extremely practical analytical approach, they further revealed that molecular flexibility is a key factor driving this anomalous "thermal resistance effect" within the confined channels of zeolites.

3. Application of ssNMR techniques in the MTO reaction

As one of the most significant industrial processes in C1 chemistry, the MTO process has garnered sustained attention from both industry and academia since its discovery in 1977.[153] This technology represents an epochal technological breakthrough in synfuel research and serves as a prime example of the mutual reinforcement between fundamental research and industrial applications, as illustrated in Fig. 5. The MTO process is a typical autocatalytic reaction network, comprising multiple parallel reaction pathways mediated by diverse reactive intermediates.[154] These pathways are governed by the interplay between the acidic properties of zeolites (*e.g.*, Brønsted acid sites (BAS), Lewis acid sites (LAS), acid strength, and acid amount) and confinement effects. Microporous zeolites, particularly ZSM-5 with MFI framework topology, are commonly used as catalysts for MTP and MTA reactions, due to the ability to control the product distribution by their pore structures. The introduction of silicoaluminophosphate materials (*e.g.*, SAPO-34), which feature a CHA framework topology with cage-like pores and milder acidity compared to ZSM-5, facilitates the selective conversion of methanol to olefins *via* cage confinement, thus marking a significant technological breakthrough.[155]

Over the past 40 years, the development of MTO technology and fundamental research has progressed in tandem, with mutual reinforcement leading to continuous improvement. Notable international petrochemical companies have invested substantial resources in developing commercially viable MTO technologies.[156,157] The commercialization of the MTH process commenced in 1985, marked by the commissioning of the first MTG plant by New Zealand Synthetic Fuels Co.[158] This milestone not only demonstrated the technical feasibility of zeolite-catalyzed C1 conversion but also laid the foundation for subsequent advancements in MTO technology. Currently, four major MTO technologies are the MTO by UOP/Norsk Hydro, MTP by Lurgi, DMTO (including its second and third generations) by DICP, and SMTO by Sinopec Shanghai Research Institute of Petrochemical Technology (SRIPT).[42,159] In 2010, DICP launched world's first industrial-scale coal-to-olefin (CTO) plant in Baotou, China, with a capacity of 1.8 Mt a^{-1}. To further increase the selectivity of light olefins, the second-generation DMTO (*i.e.*, DMTO-II) technology was industrialized with an additional fluidized-bed reactor for cracking C_4^+ byproducts in Pucheng in 2014 (Fig. 6). Furthermore, by using the new-generation catalyst, the third-generation DMTO (*i.e.*, DMTO-III) technology achieved a significant enhancement in methanol feed rate from 1.8 to 4.0 Mt a^{-1} on a single industrial reactor with a selectivity of 85–90% for light olefins. In 2023, the first industrial DMTO-III unit was put into operation in Yinchuan, China. Thus far, 36 DMTO units have been licensed, with 18 units in operation, providing a production capacity of 24 Mt a^{-1} of light olefins.

Fundamental research on the MTO process not only provides theoretical guidance for catalyst optimization and the development of efficient techniques, but also fosters innovation and advances in the basic theories of heterogeneous catalysis on acidic zeolites. Among multiple characterization methods, ssNMR spectroscopy plays an indispensable role in observing reactive intermediates, analyzing reaction pathways under real reaction conditions, monitoring the structural evolution of catalysts throughout the reaction process, and elucidating the host–guest interactions in the complex reaction systems. In this section, we will emphasize the application of ssNMR across every stage of MTO process and the facilitating role of these findings in industrial development processes, focusing mainly on the following areas: (1) revealing the reaction mechanism of methanol conversion to DME and providing spectroscopic evidence for the first C–C bond formation in the induction period, (2) promoting the development of indirect mechanisms governing the high-efficiency stage, (3) understanding the catalyst deactivation induced by coke formation, and (4) investigating the influence of water through the process.

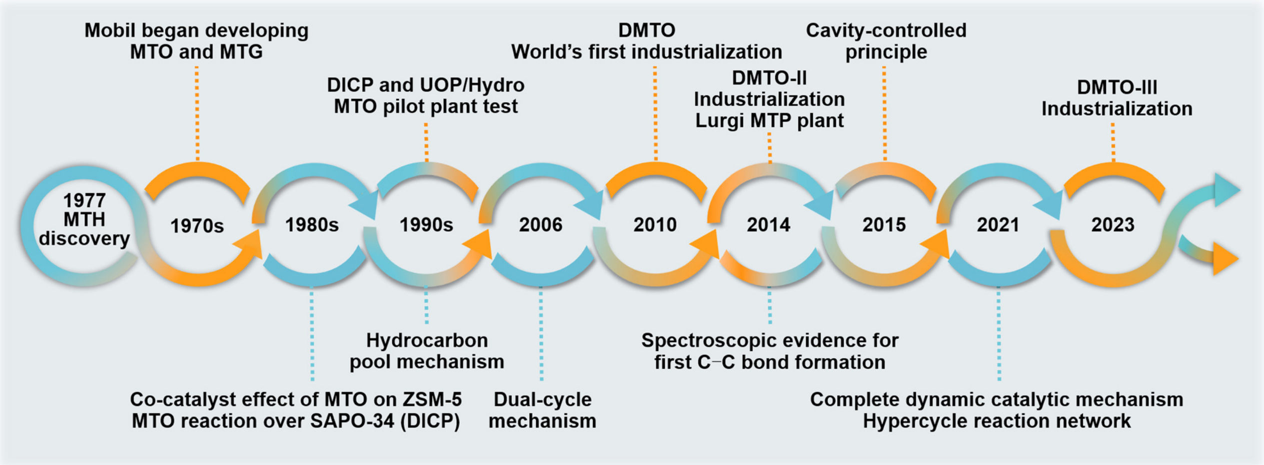

Fig. 5 Milestones in the fundamental research and industrial development of the MTO process.

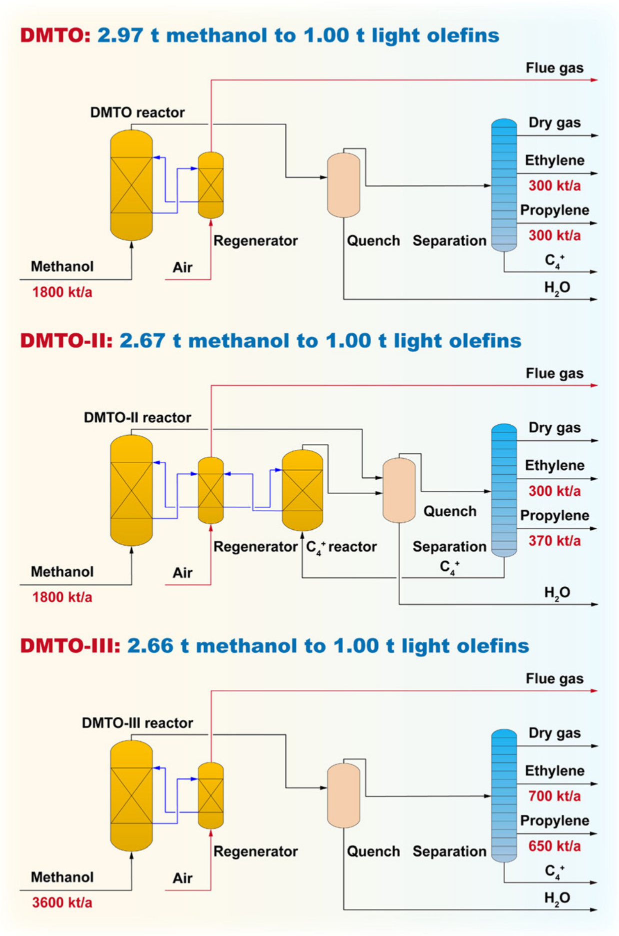

Fig. 6 Simplified process diagrams of DMTO, DMTO-II and DMTO-III technologies. Reproduced with permission from ref. 42 and 55. Copyright 2021 Elsevier and 2025 American Chemical Society.

3.1. Activation of methanol for the first C–C bond formation in the induction period

The MTO reaction is characterized by an induction period, during which substantial production of olefins is not observed. At the low temperature ($<$573 K), the initial conversion of methanol is limited, and the reaction exhibits a pronounced induction period.[20] The conversion rate gradually increases over time until reaching a stable state. This induction period is attributed to the time required for the formation of active species within the zeolite catalysts, which are essential for initiating the autocatalytic reaction networks responsible for olefin production.[160] Increasing the temperature to above 673 K can largely shorten the induction period and enhance methanol conversion up to 100%. From an industrial point of view, eliminating this period can improve the efficiency of light olefin production. In this sense, understanding and controlling the induction period is vital for optimizing the MTO process.

The nature of the intermediates and their evolution during the induction period have been subjects of extensive research, aiming to elucidate the underlying mechanisms of methanol activation over acidic zeolites.[161] Over 20 mechanisms, including oxonium ylide, carbene, carbocation, and Koch-carbonylation pathways, have been proposed to account for the initial C–C bond formation, as summarized in prior reviews and articles.[19,119] Early hypotheses attributed the induction period to the presence of impurities in methanol or carrier gas (indirect mechanism),[162] but cannot explain the origins of intermediate species or hydrocarbon pool species (HCPs). At that period, direct mechanisms faced skepticism due to insufficient experimental support and high energy barriers. A paradigm shift occurred in 2003 when Hunger and colleagues[163] identified SMS *via in situ* ssNMR spectroscopy under continuous-flow conditions, demonstrating the involvement of SMS in hydrocarbon formation. During the period of 2014–2018, pioneering studies by the research teams of Fan,[164] Weckhuysen,[165] Lercher,[166] Deng,[167] and Liu[168] provided spectroscopic evidence for the direct mechanism of initial C–C bond formation through advanced spectroscopic techniques. These critical advancements validated the direct mechanism for a long-standing controversy on the first C–C bond generation. In particular, ssNMR spectroscopy has been instrumental in identifying surface species and their transformations during the early stages of the reaction, providing atomistic insights into the roles of different active sites, such as BAS and LAS of zeolites.

3.1.1. Mechanism of methanol conversion to DME. In the initial stage of MTO process, the conversion of methanol to SMS and DME is an inevitable but often overlooked issue in the initial stage of MTO. In general, the characteristic steps involved in this reaction process include (1) unimolecular methanol dehydration to SMS, (2) coupling of SMS with another methanol molecule to generate DME, and (3) bimolecular methanol direct dehydration to DME *via* an associative pathway, and so on.[169] A fundamental understanding of this reaction process is crucial for elucidating the mechanisms underlying methanol conversion. Typically, the conventional methanol dehydration to SMS on BAS requires elevated temperatures ($>$473 K).[170] Deng *et al.*[171] reported that the Lewis acidic framework-associated tri-coordinated Al can catalyze methanol activation to form SMS species. Methanol was first adsorbed on framework-associated tri-coordinated Al, accompanied by the transfer of protons from the hydroxyl group of methanol to the zeolite framework to form SMS. They proposed that the framework-associated tri-coordinated Al with two hydroxyl groups is preferable for the methoxylation process, accounting for the observed methanol activation at low temperatures. Zheng *et al.*[172] developed a new route for methanol dehydration to SMS over SAPO zeolites based on a novel adsorbate-induced frustrated Lewis pair (FLP; three-coordinated framework Al is LA and Si–O(H) is LB) active site, enabling the SMS formation at room temperature (Fig. 7a). As shown in Fig. 7b, the ^{13}C–^{27}Al dephasing attenuation in ^{13}C–^{27}Al S-RESPDOR data reflected the distance between methanol carbon and Al in a H-SAPO-34 framework following the order of SMS (56.4 ppm with 80.5% dephasing attenuation) $<$ induced FLP adsorption (52.8 ppm with 76.5% dephasing attenuation) $<$ BAS adsorption (50.4 ppm with 50.6%

dephasing attenuation). This tendency was further supported by the geometric adsorption modes of the three above-mentioned species obtained by the refined crystal structures from synchrotron X-ray diffraction (SXRD)/neutron powder diffraction (NPD) with deuterium methanol. They demonstrated that methanol was initially adsorbed at the FLP site with its O atom directly bond to LA and H atom interacting with LB. Subsequently, a water molecule was eliminated from $-SiOH_2$, reconstructing the typical Si–O–Al bridge and yielding SMS species (Fig. 7c). Note that the dehydration process was realized without the C–O bond cleavage in methanol molecules in this new induced FLP route, in contrast to the traditional BAS-catalyzed route, which generally proceeds with methanol C–O cleavage. These results were further highlighted and evaluated by theoretical simulations.

Furthermore, the conventional BAS-catalyzed methanol dehydration typically requires elevated temperatures ($>$423 K).[170] Improving the catalytic reactivity is urgently needed but remains extremely challenging. In response to this key issue, Zheng *et al.*[173] demonstrated a co-feeding strategy of acetone to tune the local microenvironment of methanol within H-ZSM-5, realizing unprecedented DME formation at room temperature and olefin production at 413 K. As shown in Fig. 7d, upon increasing the reaction temperature for the H-ZSM-5 zeolite with ^{13}C-methanol adsorption, the ^{13}C-DME signal at 60.0 ppm only appeared above 393 K. After co-injection of ^{13}C-methanol with additional 2-^{13}C-acetone, this characteristic signal was excitingly observed when the reaction occurred even at 298 K (Fig. 7e). Meanwhile, significant enhancement of the ^{13}C-DME signal was detected for H-ZSM-5 zeolites with ^{13}C-methanol and 2-^{13}C-acetone co-injection compared with those without 2-^{13}C-acetone across the reaction temperature range. These findings suggested that the injection of an extra acetone molecule can considerably facilitate methanol conversion to DME. Further 2D ^{1}H–^{1}H homonuclear correlation NMR experiments indicated that the spatial interaction between acetone and methanol is an essential prerequisite for accelerating methanol conversion (Fig. 7f). In combination with high-level multiscale theoretical simulations, they proposed that the crucial role of acetone in accelerating methanol dehydration to DME is the perturbation and destabilization for the adsorbed methanol cluster with strong hydrogen bonds, and the following water traction during DME formation, decreasing the reaction-free energy barriers from 136.9 kJ mol^{-1} (without acetone) to 103.9 kJ mol^{-1} (with acetone). This work provides new

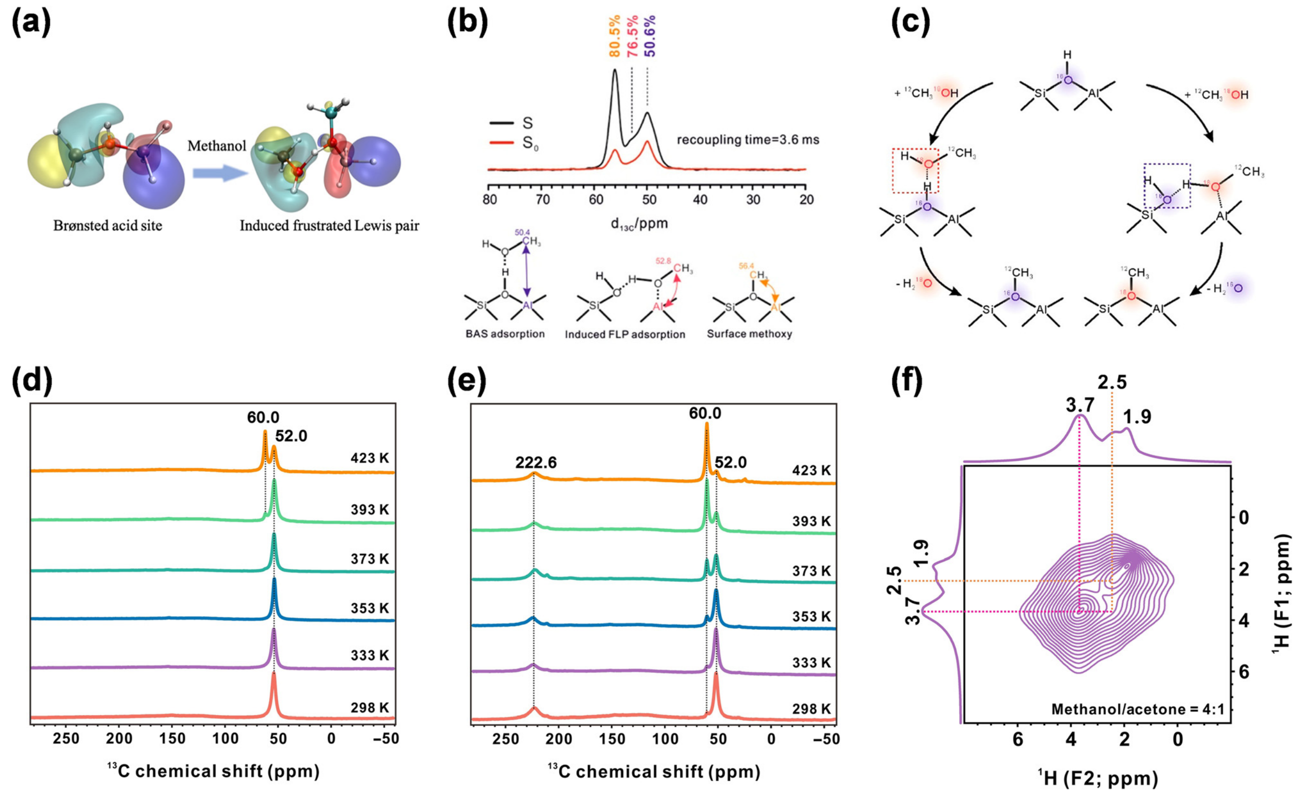

Fig. 7 (a) Illustration of induced FLP sites formed by methanol adsorbate. (b) ^{13}C–^{27}Al-S-RESPDOR spectra of ^{13}C-methanol adsorbed on H-SAPO-34 in the top, and schematic depicts the proposed signal assignment of BAS adsorption, FLP adsorption, and the surface methoxy species in the bottom. (c) Schematic depicting the mechanisms of the formation of SMS *via* the traditional BAS route and proposed induced FLP route. Reproduced with permission from ref. 172. Copyright 2021 American Chemical Society. (d) and (e) ^{13}C MAS NMR spectra of H-ZSM-5 zeolites with the adsorption of ^{13}C-methanol without (d), and with additional 2-^{13}C-acetone (e) recorded upon reaction at different temperatures for 2 hours. (f) Two-dimensional ^{1}H–^{1}H single-quantum MAS NMR spectra of H-ZSM-5 zeolite with the adsorption of ^{13}C-methanol and 2-^{13}C-acetone and reaction at 298 K. Reproduced with permission from ref. 173. Copyright 2025 American Association for the Advancement of Science.

opportunities for the rational design of reaction systems by manipulating the local surroundings to regulate catalytic performances.

3.1.2. SMS-mediated direct mechanism on BAS. As the most experimentally validated intermediate during the induction period, SMS serves as the pivotal species in C–C bond formation. Fan *et al.*[164] proposed a direct mechanism in which SMS interacts with DME to generate methoxymethyl carbocation ($CH_3OCH_2^+$), exhibiting a lower energy barrier compared to alternative pathways (*e.g.*, methane–formaldehyde coupling). *In situ* ssNMR studies provided the spectroscopic evidence that the direct formation of the C–C bond originates from the interaction between surface-adsorbed C1 reactants (*i.e.*, DME/methanol) and SMS/TMO intermediates on the H-ZSM-5 catalyst.[168] At the beginning of the methanol conversion at 573 K in an NMR rotor as a microreactor under continuous-flow conditions, a novel signal at 69.0 ppm indicated methyleneoxy species formation *via* SMS/TMO-mediated DME methylation, coinciding with the first C–C bond generation (Fig. 8a). Subsequent breakage of the C–H bond from this activated reactant yielded ethene, with hydrogen transferring to framework oxygen. Furthermore, the dynamic progressive activation of DME evoked by SMS on H-ZSM-5 was revealed by *in situ* ssNMR at programmed temperatures from 373 to 573 K.[174] During the continuous injection of methanol at temperatures above 473 K, the chemical shift of DME gradually migrated from 63.5 to 69.0 ppm, indicating that highly activated DME exhibits the characteristics of methyleneoxy analogue species. *Operando* simulations suggested that with the increase in temperature, SMS species transition from covalent to ionic nature, and the elongated C–O bond facilitates the attack on approaching C1 molecules (methanol or DME).

The 2D ^{13}C–^{13}C correlation ssNMR spectroscopy provides more details for the dynamic evolution of C1 species in the C–C bond formation over CHA zeolites. The close spatial proximity of SMS with adsorbed methanol was evidenced by a strong cross-peak at (57.7, 52.2) ppm in the 2D ^{13}C–^{13}C PDSD spectra recorded after an MTO reaction at 673 K on H-SAPO-34 zeolites, suggesting that methanol activation may occur *via* polarization of the C–H bond of SMS.[165] Furthermore, in a series of 2D ^{13}C–^{13}C PDSD experiments conducted at 298, 353, and 403 K on H-SAPO-34 zeolites after feeding $^{13}CH_3OH$ for 60 s, Xu and Liu *et al.*[119] unrevealed an intensification in the correlation between SMS and surface-adsorbed C1 reactant as the temperature increased. As shown in Fig. 8b, spatial interaction between SMS and DME was observed at a relatively low temperature of 353 K, indicated by a correlation between SMS (56.7 ppm) and DME (60.5 ppm). As the temperature increased to 403 K, the appearance of a cross-peak at (56.7, 50.8) ppm revealed the correlation of SMS and adsorbed methanol. These observations imply that DME more easily interacts with SMS compared to methanol at lower temperatures. Additionally, 2D ^{13}C–^{13}C CORD MAS NMR experiments directly captured and identified surface ethoxy species (70.5 and 14.2 ppm) as highly reactive ethene precursors on HSSZ-13 under real MTH reaction at 493 K (Fig. 8c).[121] The advanced *ab initio* molecular dynamics (AIMD) simulations further visualized the cleavage dynamics of the C–O and C–H bond in SMS, confirming the critical role of SMS in the initial C–C bond formation. Notably, the free energy barriers of the C–C bond coupling reaction *via* the DME and SMS pathways (141.6 kJ mol^{-1}) are lower than that of the methanol and SMS pathway (170.5 kJ mol^{-1}), aligning with the observed spatial proximity of these species in ^{13}C–^{13}C PDSD spectroscopy.

Besides DME, the coexistence of methane, formaldehyde and CO has been widely reported during the initial stage of the methanol conversion on H-ZSM-5 zeolites.[175,176] Notably, oxygenated and carbonylated compounds have been detected from MTO facility in Baotou, China.[177] Understanding the role of these species is essential for elucidating the mechanistic diversity of C–C bond formation. The methane–formaldehyde mechanism suggests that methane and formaldehyde are generated through the reaction of the SMS and DME. The research groups of Coperet and Sautet,[178] as well as Lercher,[166] have highlighted the pivotal role of surface-bound acetate species (*i.e.*, MeOAc) in the initial C–C bond formation during the MTO reaction. These species are formed *via* Koch carbonylation (as the core step in the DME carbonylation reaction), where methanol interacts with SMS in the presence of CO, leading to the formation of acetate intermediates. These intermediates can further transform into surface acetyl groups, methyl acetate species, or ketene, serving as the precursors for olefin production during the MTO reaction.[36,179,180] The identification of these acetate species has been achieved through advanced 1D and 2D ^{13}C ssNMR techniques, providing direct spectroscopic evidence of their presence and involvement in the reaction mechanism.[78,181] For instance, Weckhuysen *et al.*[165] provided spectroscopic evidence for C–C bond formation on H-SAPO-34, through the identification of surface-trapped methyl acetate (180.5 and 22.3 ppm) by combining 2D ^{13}C–^{13}C PDSD and ^{13}C–^{1}H CP-HETCOR spectroscopy (Fig. 8d). Dai and Li[182] further observed the formation of acetaldehyde (207 and 29 ppm) from surface-bound acetyl species (derived from the carbonylation of SMS by CO) over H-ZSM-5 zeolites, as revealed by *ex situ* ^{13}C MAS NMR spectra. *Via* a combination of kinetic studies, spectroscopic analyses, and theoretical calculations, the critical role of acetyl motifs in forming acetaldehyde was confirmed, which, in turn, induces the formation of HCP species *via* a series of reactions such as aldol condensation, cyclization, and hydrogen transfer. The detection of trace oxygenates (methanol, dimethyl ether, ethanol, acetaldehyde, and acetone) in industrial-scale DMTO reactors provides experimental validation (see Table S1, ESI†) for the proposed oxygenate-mediated C–C coupling mechanisms. However, the formation pathways of these intermediates and their dynamic roles in governing product selectivity still need further in-depth research.

3.1.3. Critical role of LAS in C–C bond formation. Under mild hydrothermal/thermal treatment, it is inevitable to generate LAS including extra-framework aluminum (EFAl) species, framework tri-coordinated Al, and framework-associated Al.[183–185] Recent studies have highlighted the crucial

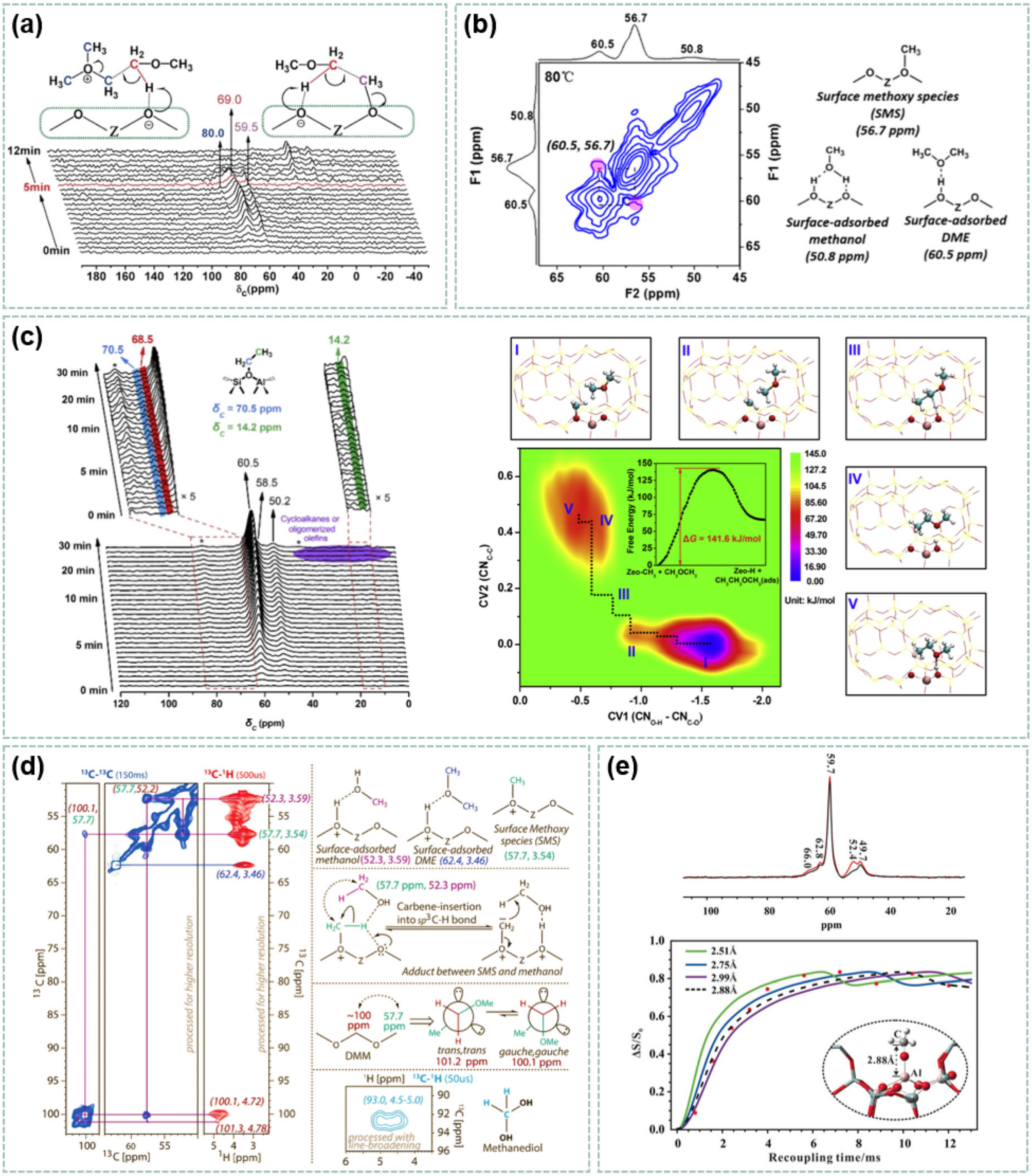

Fig. 8 Spectroscopic evidence for the first C–C bond formation. (a) *In situ* ^{13}C MAS NMR spectra recorded during ^{13}C-methanol conversion over H-ZSM-5 at 573 K. Reproduced with permission from ref. 168. Copyright 2017 John Wiley and Sons. (b) Two-dimensional ^{13}C–^{13}C PDSD MAS NMR correlations of SMS, DME, and methanol on H-SAPO-34 recorded at 353 K after the MTO reaction for 60 s at 573 K. Reproduced with permission from ref. 119. Copyright 2018 American Chemical Society. (c) *In situ* ^{13}C MAS NMR spectra and AIMD simulation results of the C–C bond formation for methanol conversion at initial MTH reaction stage over H-SSZ-13. Reproduced with permission from ref. 121. Copyright 2021 Elsevier. (d) SsNMR spectra of methanol, methoxy, and acetal species in H-SAPO-34 after MTO reaction for 30 minutes at 673 K. Reproduced with permission from ref. 165. Copyright 2016 John Wiley and Sons. (e) ^{13}C–^{27}Al S-RESPDOR spectra of trapped products obtained from reaction of ^{13}C-methanol over dealuminated H-ZSM-5 at 523 K for 1 min (in the top). ^{13}C–^{27}Al RESPDOR built-up data of the 52.4 ppm signal and the simulated curves: green, blue, purple, and dashed black lines correspond to an internuclear ^{13}C–^{27}Al distance of 2.51, 2.75, 2.99, and 2.88 Å, respectively (in the bottom). Inset: Theoretically optimized local structure of SMS-EFAL complex. Reproduced with permission from ref. 167. Copyright 2018 John Wiley and Sons.

role of LAS in the MTH reaction. Lercher *et al.*[186] proposed that EFAL species facilitate hydride transfer between methanol and alkane, generating alkanes and HCHO simultaneously. The formed HCHO subsequently reacts with alkenes at BAS to generate dienes and aromatics, which dominate the production of aromatics and light alkanes. Zheng and co-workers[187] theoretically identified that the synergetic combination of EFAL and BAS promotes initial C–C bond formation *via* an Al–COH_2^+ intermediate. Meanwhile, Deng and co-workers[167] provided direct evidence for the formation of SMS-EFAL (at 52.4 ppm) in ^{13}C MAS NMR spectroscopy on dealuminated H-ZSM-5 zeolites. By employing ^{13}C–^{27}Al S-RESPDOR spectroscopy,[188] the internuclear distance between the ^{13}C atom in SMS-EFAL species and the ^{27}Al atom in the zeolite framework was quantitatively determined to be 2.75 ± 0.24 Å by simulating the dephasing built-up curves (Fig. 8e). Moreover, formate species, which can be generated through hydrogen transfer between SMS-EFAL species and methanol, were observed during methanol conversion on dealuminated H-ZSM-5 zeolites at 523 and 548 K. During the co-reaction of ^{13}C-methanol and ^{13}C-formaldehyde, acetaldehyde (226.2 ppm), surface acetate species (186.3 ppm), methyl acetate (177.9 ppm), and surface ethoxy species (72.4 ppm) were captured in ^{13}C CP/MAS spectra, which was absent without formaldehyde feeding. These signals suggested the involvement of formaldehyde in the formation of the initial C–C bond over EFAL at lower temperatures. DFT calculations further elucidated that SMS-EFAL leads to the formation of formaldehyde, further producing surface ethoxy species and ethanol for ethene generation. Overall, the LAS clusters exert a dual effect on the MTO reaction. On the one hand, EFAl species can synergistically interact with BAS to promote the formation of the initial C–C bonds, thereby influencing the reactivity in both alkene and aromatic methylation steps. On the other hand, LAS facilitates hydrogen transfer pathways that favor the formation of alkanes and expedite catalyst deactivation due to polycyclic aromatic hydrocarbon (PAH) formation with formaldehyde participation.[167,189–196]

In the industrial MTO process, the induction period constitutes a critical phase for reaction initiation, characterized by delayed product formation and low efficiency for alkene production. The formation of the initial C–C bond in this period accumulates essential reactive species required for the high-efficiency stage. The different active species (even in trace amounts) generated in this period can significantly influence the subsequent reaction process. For instance, initial olefins promote HCP species formation, while formaldehyde accelerates catalyst deactivation *via* undesired polyaromatic coke formation.[189,190] Moreover, the quality of industrial methanol feeds is also crucial, as impurities (*e.g.*, ethanol, aldehydes, acids, amines, and metal ions) can alter catalyst performance and product purity. Interestingly, water does not require special removal from methanol feedstocks because it serves as a reaction medium that helps control the reaction temperature and remove the heat of the reaction (detailed in Section 3.4).

3.2. Hydrocarbon pool (HCP) mechanism in high-efficiency stage

Following initial C–C bond formation, the indirect mechanism is widely recognized as the dominant pathway for forming alkenes and aromatic products during the high-efficiency stage. Unlike the induction period, this stage is characterized by dynamic and complex processes, with significant variations in product selectivity depending on the catalysts employed. For instance, SAPO-34 exhibits high selectivity toward light olefins, whereas H-ZSM-5 preferentially produces propene (MTP), gasoline (MTG), or aromatic hydrocarbons (MTA). Numerous studies revealed that co-feeding methanol with alkanes, alkenes, and aromatic hydrocarbons can alter product distribution, demonstrating that catalytic reaction networks can be modulated by additional hydrocarbons.[197,198] Pre-coking strategies have been confirmed in the MTO unit of demonstration scale for highly shape-selective MTO processes. However, utilizing the co-reaction effect in MTO to target specific products relies on the control over catalytic networks. Over the past forty years, the hydrocarbon pool concept has been continuously refined and expanded, evolving from the consecutive methylation and cracking reactions to paring reaction, side-chain alkylation mechanism, and ultimately to the HCP mechanism, which now accounts for the hydrocarbon formation in MTH reactions.[18,199–201] SsNMR spectroscopy is possibly the most widely used method for accurately elucidating the structure of carbocationic HCP species confined to zeolites and their host–guest interactions, thereby providing critical experimental evidence for constructing efficient catalytic cycles.

3.2.1. Structure and noncovalent interactions of HCP species. Haw and co-workers[72] developed an *in situ* pulse-quench reactor (see Section 2 for details) that rapidly quenches the catalyst bed with nitrogen for subsequent measurements. Revealed by the character signals in ^{13}C MAS NMR spectra (130–150 ppm, and 240–250 ppm), the alkylated cyclopentadienium ions and methylbenzenium cations (pentamethylbenzenium cation and heptamethylbenzenium cation) were identified as HCP species upon acetone introduction or the co-feeding of aromatics with methanol over various zeolites (*e.g.*, H-ZSM-5, H-SAPO-34, and H-Beta).[202–206] The direct observation of HCP intermediates under reaction conditions has been achieved by employing the *in situ* MAS NMR spectroscopy under continuous-flow conditions.[207] Xu and Liu *et al.*[208] observed the formation of heptamethylbenzenium cation (heptaMB$^+$) and methylcyclopentenyl ion (MCP$^+$) on a DNL-6 catalyst (an eight-membered-ring SAPO molecular sieve with an RHO structure and large α cages) after ^{13}C-methanol conversion at 548 K. This identification was further supported by GC-MS analysis of their deprotonated form, obtained by dissolving the organic-containing zeolite framework in hydrofluoric acid, followed by extracting the organic species in organic solvents. The presence of these carbenium cations on DNL-6 was attributed to the large cages and the high acidity of this SAPO molecular sieve. Additionally, under real MTO conditions, heptaMB$^+$ and MCP$^+$ were detected in CHA-type catalysts by conducting the reaction under milder conditions to lower the reactivity of carbenium ions.[209] The involvement of these species in aromatic-based dual-cycle mechanisms including paring and side-chain cycles was confirmed by theoretical calculations. Refocused INADEQUATE experiments have provided direct structural assignments for a series of carbenium ions derived from the through-bond correlations on H-ZSM-5

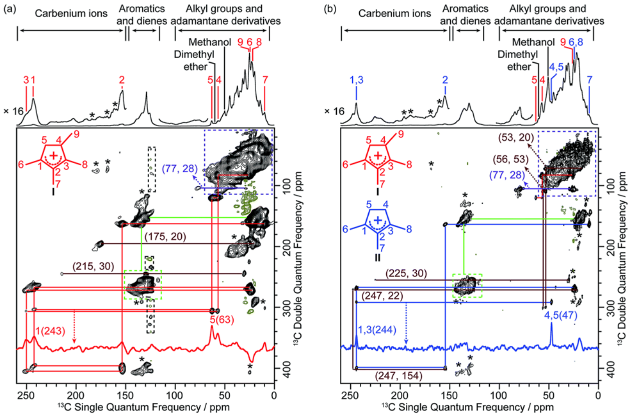

Fig. 9 2D ^{13}C–^{13}C refocused INADEQUATE spectra of activated (a) H-SSZ-13 and (b) H-SAPO-34. Data were recorded at 9.4 T and at a MAS rate of 14 kHz. Signals of positive intensities and Fourier Transform (FT) wiggles of negative intensities are coded in black and olive, respectively. Asterisks (*) denote spinning sidebands. Reproduced with permission from ref. 100. Copyright 2019 Royal Society of Chemistry.

and CHA-type catalysts.[95,99,100] This 2D experiment not only provides a straightforward approach for mapping the carbon skeleton of carbenium ions through *J* couplings (Fig. 9),[100] but also enables a more accurate determination of the ^{13}C chemical shifts of different carbon sites owing to the enhanced resolution in the vertical dimension. Furthermore, the application of DNP-enhanced NMR spectroscopy significantly reduced the acquisition times from several days under the standard experiments at room temperature to just 14 hours, providing a powerful approach for identifying carbocation ions present in low concentrations.[99]

The trapped HCP species (cyclic carbenium ions) in the zeolite channel or cage serve as the reaction center in the steady stage of MTO, acting as supramolecular entities. Deng and coworkers[210,211] applied a ^{13}C–^{27}Al S-RESPDOR method, to probe dipolar interaction between ^{13}C atoms in trapped organic species and ^{27}Al atoms in zeolite frameworks. Specifically, ^{13}C–^{27}Al dephasing was observed for the methyl group of cyclopentenyl cations and pentamethylbenzenium ions (25 ppm), as well as methylbenzenes (17 and 18 ppm), during the methanol reaction over H-ZSM-5 at 573 and 623 K (Fig. 10a). These results provide critical insights into noncovalent interactions (generally refer to hydrogen bonding, π-interaction, van der Waals interaction, and electrostatic interaction) in the MTO reaction. Additionally, the intermolecular noncovalent interactions between carbenium ions and various organic molecules such as methanol, ethene, and propane were revealed by combining 2D ^{13}C–^{13}C correlation ssNMR spectroscopy and theoretical analyses.[212] Adsorbing ^{13}C-labeled methanol/ethene/propane over cyclopentenyl-cation-containing H-ZSM-5 yielded strong correlation peaks in the 2D ^{13}C–^{13}C PDSD spectra, confirming cation-induced dipole, cation–dipole and cation–π interactions (Fig. 10b). Reduced density gradient (RDG) isosurfaces further visualized these intermolecular interactions, suggesting preferential adsorption of organic molecules at the center of pentenyl cations due to their high positive charge density. The influence of noncovalent interactions on the adsorption and transformation of alkanes, alcohols, and alkenes was further confirmed by comparing the catalytic reactions of propane, methanol, and ethene on zeolites with and without the addition of cyclopentenyl carbocations. The co-reaction with cyclopentenyl carbocations significantly increased the conversion rates of propane from 30.8% to 45.2%, methanol from 26.9% to 98.6%, and ethene from 30.9% to 52.2%. These enhancements clearly demonstrate the promoting effect of the cyclic cations. During methanol conversion, the presence of cyclopentenyl carbocations also increased aromatic selectivity while decreasing propene selectivity, indicating that these cations influence product distribution by altering the balance between alkene-based and aromatic-based reaction pathways. Overall, the combination of ssNMR experiments and theoretical studies suggests that the cyclic cations interact noncovalently with methanol and hydrocarbon products, promoting methanol conversion and modulating the transformation of key intermediates such as alkanes and olefins.

Beyond these noncovalent interactions, strong interactions between the confined HCP species and the zeolite framework have also been quantitatively characterized by the ^{29}Si–^{13}C REDOR experiments. Due to the low HCP species concentration and the intrinsically low γ of ^{29}Si nuclei, probing long-range van der Waals interactions between HCP species and the aluminosilicate framework remains a challenge. Through-space ^{13}C–^{27}Al S-RESPDOR and ^{29}Si–^{13}C REDOR experiments demonstrated close spatial relationships between framework ^{27}Al, ^{29}Si and ^{13}C nuclei spins in HCP species, as indicated by dephasing of ^{13}C and ^{29}Si NMR signals, respectively.[99] DNP-enhanced ^{29}Si–^{13}C REDOR experiments further enabled quantitative spatial mapping proximities between confined carbonaceous species and zeolite surface sites in tens of hours.[95] Moreover, the high signal-to-noise ratios allow the detection of small differences in REDOR fraction patterns as a function of recoupling times for individual Si sites. These host–guest interactions predominantly govern the adsorption of HCP components, ultimately leading to preferential accumulation within zeolitic channels and subsequent catalyst deactivation *via* pore blockage.

3.2.2. Linkage between direct and indirect mechanisms and the interconnection of catalytic cycles. The interplay between direct and indirect mechanisms in zeolite-catalyzed methanol conversion involves dynamic transitions between distinct catalytic cycles. While the indirect mechanism, governed by HCP species is widely accepted as the dominant pathway for methanol propagation at the steady stage, the intrinsic linkage between these pathways remains debated. Two key challenges persist: (1) elucidating the transition from initial direct C–C coupling to the HCP-mediated indirect mechanisms, and (2) clarifying the interconnection between alkene-based and aromatic-based cycles. Significant efforts have been dedicated to elucidating the hydrocarbon pool chemistry in the early stages of MTH conversion on zeolites

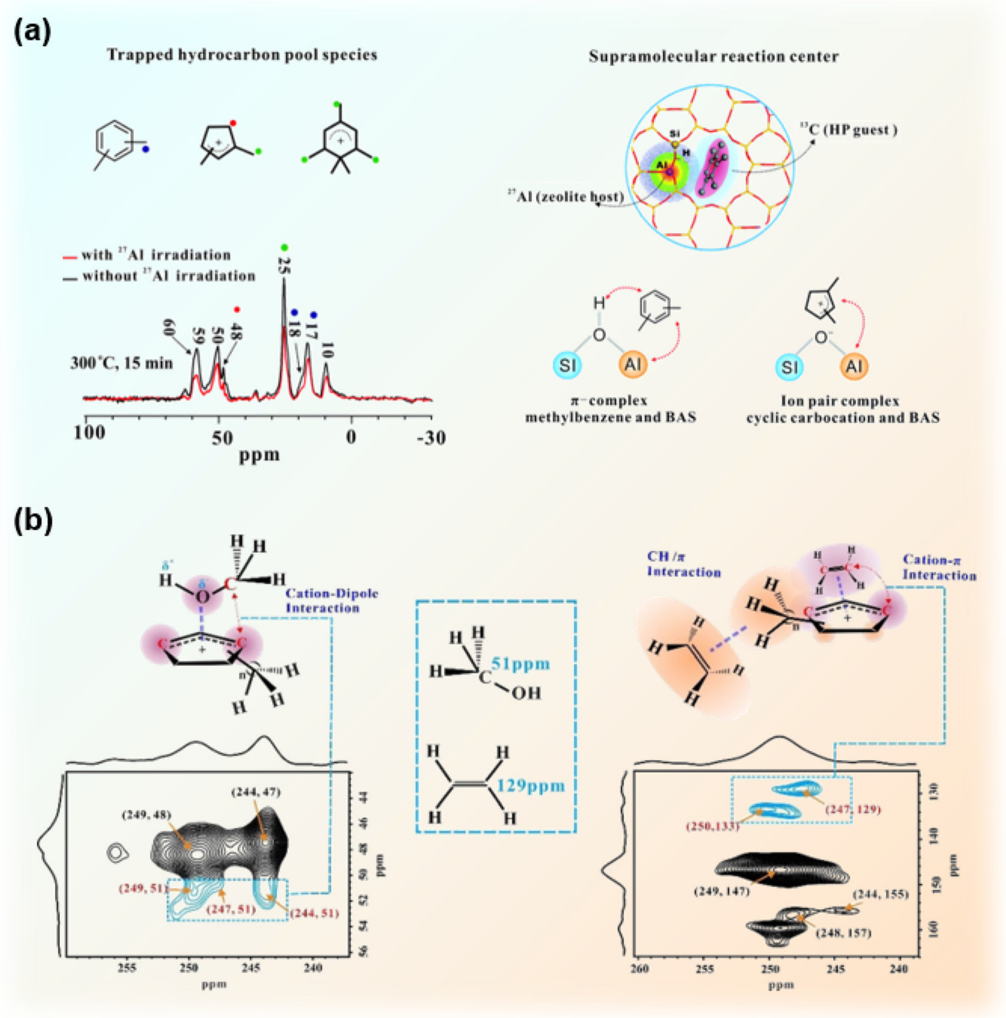

Fig. 10 (a) ^{13}C–^{27}Al S-RESPDOR MAS NMR spectra of trapped organic species over H-ZSM-5 zeolite and the supramolecular models. Reproduced with permission from ref. 41 and 210. Copyright 2021 Royal Society of Chemistry and 2016 John Wiley and Sons. (b) Two-dimensional ^{13}C–^{13}C PDSD spectra of adsorbed ^{13}C-labeled methanol and ethene (248 K) over cyclopentenyl-cation-containing H-ZSM-5. Reproduced with permission from ref. 212. Copyright 2021 John Wiley and Sons.

through combined experimental and theoretical investigations, advancing the understanding of these complex catalytic transformations.

Theoretical calculation suggests that ethene and propene formed *via* initial C–C bond coupling rapidly undergo cyclization to generate five- and six-membered ring hydrocarbons, which act as the first HCP intermediates.[213,214] Hunger and Li[215] experimentally identified early-stage species, including three-ring compounds, dienes, and MCP$^+$ on a H-SAPO-34 catalyst *via* ^{1}H MAS NMR and ^{13}C MAS NMR. Further studies using synchroton infrared microspectroscopy by Howe *et al.*[216] proposed that dimethylcyclopentenyls are primary HCP components. This hypothesis was experimentally validated by the observation that MCP$^+$ was formed earlier than PMBs on HSSZ-13 from *in situ* ^{13}C MAS NMR spectra under continuous-flow MTO conditions (Fig. 11a).[217] The subsequent transformation of MCP$^+$ into PMBs was confirmed through ^{13}C-isotope tracing experiments of MCP$^+$ (formed by the adsorption of pentamethylcyclopentadiene molecules) and ^{13}C-methanol, supported by DFT calculations. Further transformation of MCP$^+$ produced PMBs through a serious of deprotonation, hydride transfer, ring expansion, and methylation reactions at the transition stage. Based on these spectroscopic and theoretical insights, it was proved that pentaMCP$^+$ species serve as the initial HCP species, uniquely bridging the direct mechanism at the initial stage and the indirect mechanism that dominates the steady-state stage.

Considering the involvement of surface-bound acetate species in the initial C–C bond formation, several research groups devote to bridge the gap between the Koch-carbonylation mechanism and the HCP mechanism by adding non-methanol reactants such as methyl-acetate/acetaldehyde/acetone. Weckhuysen and colleagues[120] identified the governing HCP species as dienes, polymethyl-benzenes, and acetic acid by employing PDSD experiments during methyl-acetate conversion over H-SAPO-34. Based on the observed species, they

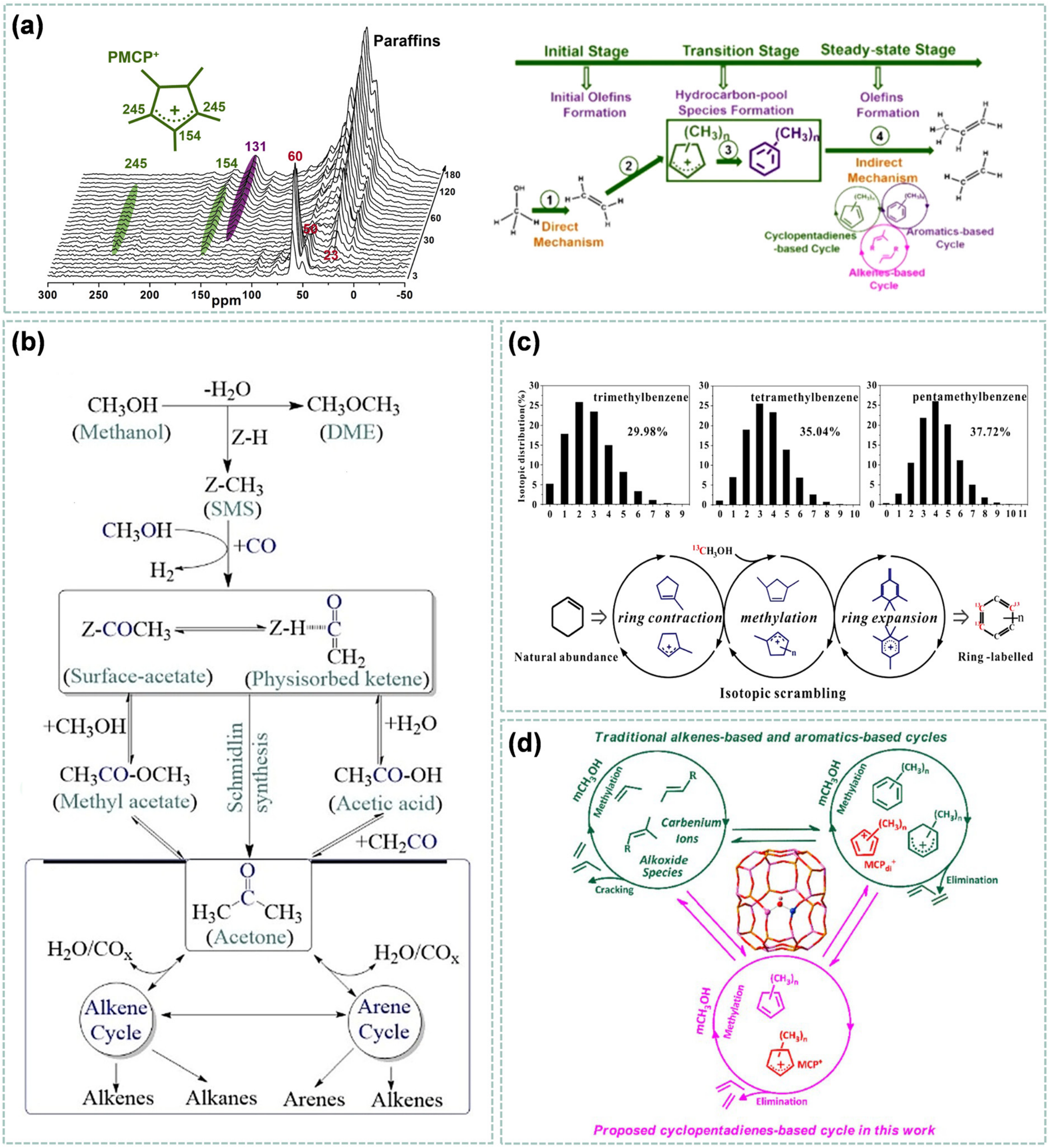

Fig. 11 (a) Identification and the proposed route for the formation and evolution of PMCP$^+$ from $^{13}CH_3OH$ reaction over H-SSZ-13 catalyst. Reproduced with permission from ref. 217. Copyright 2020 American Chemical Society. (b) Connection of the Koch-carbonylation-led direct and dual cycle mechanisms. Reproduced with permission from ref. 33. Copyright 2024 John Wiley and Sons. (c) ^{13}C atom distribution in trimethylbenzene, tetramethylbenzene, and pentamethylbenzene obtained from cofeeding of cyclohexene and ^{13}C-methanol at 523 K for 8 s, and model of incorporation of ^{13}C atoms into the ring of aromatics through a sequential reaction on H-ZSM-5. Reproduced with permission from ref. 219. Copyright 2020 American Chemical Society. (d) Dual cycles (alkene-based and aromatic-based cycles) and the cyclopentadiene-based cycle proposed for methanol conversion on SAPO-34. Reproduced with permission from ref. 221. Copyright 2019 American Chemical Society.

proposed that HCP species formed from methyl acetate provides a mechanistic bridge between the Koch carbonylation mechanism and the HCP mechanism. Similarly, Li *et al.*[182] observed the formation of acetaldehyde derived from the carbonylation of SMS by CO from ^{13}C MAS NMR spectroscopy, suggesting that acetaldehyde from the hydrogenation of surface-bound acetyl species is responsible for the initiation of MTH conversion on H-ZSM-5 zeolites. Gascon and Chowdhury[33] provided further insights, demonstrating that acetone derived from ketene acts as a bridge to link the Koch carbonylation mechanism during the induction period and the dual-cycle mechanism during the steady stage on the H-ZSM-5 catalyst. Combining *operando* UV-Vis spectroscopy, online mass spectrometry, and ssNMR spectroscopy with the strategic use of ^{13}C-enriched reactants, it was proved that co-feeding acetone with methanol significantly alters product distribution by favoring aromatic formation while maintaining light olefins yields, regardless of feed compositions, reaction temperature, and WHSVs. By comparing the 2D dipolar-based ^{13}C–^{13}C correlation spectra of the MTH reaction and AMTH (*i.e.*, co-conversion of $CH_3{}^{13}COCH_3$ and methanol to hydrocarbons), methylated monoaromatics, naphthalene/polyaromatics, and branched paraffinic species were identified as the trapped organics on zeolites in both reactions. Notably, surface acetate and dicarbonylated species were exclusively detected in the AMTH reaction (Fig. 11b). These findings suggest that acetone, derived from the Koch-carbonylation in the early stage of MTH, preferentially incorporates into the arene cycle, promoting aromatic HCP species formation during steady-state conversion rather than undergoing aldol condensation.

The dual-cycle mechanism, consisting of alkene-based and aromatic-based cycles, was proposed by Olsbye *et al.*[218] to rationalize the product distribution in MTO over H-ZSM-5. Employing the 1D and 2D ^{13}C MAS NMR spectroscopy enables direct observation and structure identification of cyclic carbenium ions, providing vital experimental evidence for the dual-cycle mechanism. Extensive analyses, including $^{12}C/^{13}C$ switch experiment, dissolution and extraction procedure, and theoretical calculations have further refined the understanding of the interconnection between dual cycles, beyond conventional hydrogen transfer and cyclization reactions. Deng and co-workers[219] confirmed that cycloalkenes facilitate this connection through a ring-contraction/expansion process. During the co-reaction of cyclohexene and ^{13}C-methanol, methylated and ethylated cyclopentenyl and pentamethylbenzenium ions and methylbenzenes were formed, which was evident from the results of ^{13}C CP MAS NMR and GC-MS analyses of the corresponding trapped organic species (Fig. 11c). Cyclohexene was proposed to undergo ring contraction to form cyclopentene and subsequently trigger the aromatic-based cycle through the ring expansion, which is consistent with the ^{13}C isotopic scrambling in aromatics and the energetic feasibility of cycloalkene aromatization supported by DFT calculations. Further supporting this, Wang *et al.*[220] demonstrated that methylcyclohexene acts as the initial HCP species to generate MCPs *via* ring contraction or MBs through hydride transfer and deprotonation on H-ZSM-5. Additionally, the observation of MCP^+ and its deprotonated form was detected by ^{13}C MAS NMR and GC-MS over an H-SAPO-34 catalyst, verifying their involvement in the MTO reaction.[221] Consequently, a unique MCP-based cycle was proposed, not only as an energetically favored pathway for the formation of light olefins, but also as a crucial bridge linking the alkene-based cycle and aromatic-based cycle (Fig. 11d). Recently, the autocatalysis-driven network of MTO has been demonstrated using a multitechnique approach that integrates kinetics analyses, electronic state analyses, AIMD simulations, and multiple *in situ*/*operando* spectroscopic techniques.[222] Once the initial olefins are formed by direct coupling of SMS with DME, autocatalysis is triggered to switch the reaction from the induction period to the high-efficiency stage. This transition stage is facilitated by the formation of a hypercycle, which consists of an olefin-based cycle interconnected with an MCP-based cycle and an aromatic-based cycle.

These in-depth explorations of the catalytic cycles in the MTO reaction provide a comprehensive understanding of the evolution and pathways from methanol to products on the zeolite catalyst, and may extend to elucidate the mechanism of ethanol-to-hydrocarbon reaction.[223,224] Moreover, light olefin selectivity can be systematically tuned by modulating HCP dynamics through external reactants and tailored zeolite architectures. Co-feeding methanol with additives (*e.g.*, alkenes, aromatics, and formaldehyde) can shift the ethylene-to-propylene ratio by influencing whether the olefinic or aromatic cycle dominates in the dual-cycle mechanism.[197,225] Importantly, ''pre-coking'' strategy involves pre-filling the CHA cage with specific polycyclic aromatic hydrocarbon molecules before the reaction, increasing the ethene selectivity through promoting the catalytic cycle involving naphthalenic cations.[226–228] In addition, the catalytic mechanism of this organic–inorganic system provides a fundamental basis for developing innovative catalytic routes, *e.g.*, coupling of methanol with methylbenzene or formaldehyde.[225,229] These catalytic approaches not only improve the reaction efficiency and selectivity but also pave the way for more sustainable production methods in the petrochemical industry by enabling the conversion of simple feedstocks into higher value chemicals.

3.2.3. Effect of channel/cavity geometry on HCPs. Typically, the size of the cavity and channel for zeolites play a dominant role in controlling the formation of carbenium ions as HCP species, further regulating the formation of alkene and aromatics in the MTO reaction. Recently, Ferri and co-workers[230] have illustrated the relationship between zeolite topology and the nature of carbenium ions by employing transient *operando* diffuse reflectance infrared Fourier transform spectroscopy (DRIFTS) coupled with gas chromatography. On H-ZSM-5, multispecies including alkyl-substituted cyclopentenyl cations, polymethylbenzenium ions, and acyclic allylic carbocations were characterized as active reactive centers, which correlated with the formation of linearly short olefins in the MTO process. Polymethylbenzenium ions were predominantly formed on H-SSZ-13 with CHA topology, correlating with ethene and propene formation. Ferrierite (FER), a medium-pore zeolite with a two-dimensional channel system, restricted the formation of cyclic carbenium ions. Despite this, FER show high selectivity toward C_4–C_5 olefins, accompanied by the formation of C_6 aliphatic chains that may include allylic cation groups. Furthermore, Bladus and Weckhuysen *et al.*[94] elucidated the relationships between zeolite channel geometry and reactive intermediates by using anisotropic zeolite ZSM-5 crystals with different channel orientations. As illustrated in Fig. 12a, combining 2D ^{13}C–^{13}C and ^{13}C–^{1}H ssNMR experiments demonstrated a higher degree of alkylation of HCP species in *b*-oriented zeolite crystals dominated by straight channels. This enhanced alkylation indicates that straight channels favour the aromatic cycle, thereby promoting ethene formation. Conversely, only symmetric methylated aromatics were observed in *a*-oriented crystals dominated by sinusoidal channels, suggesting that the more constrained sinusoidal channels favour the olefin cycle. These findings provide valuable insights for designing catalysts with tailored selectivity and enhanced performance in methanol conversion processes. Recently, paired BAS was found to promote the transformation of HCP species, such as aromatics, cyclopentenyl cations, and pentamethyl-benzenium ions, into the light olefins, elucidating the critical relationship between the BAS configuration and catalytic performance in the MTO reaction over ZSM-5 zeolites.

Recent studies have elucidated the significant role of zeolite cavity size in controlling the formation and reactivity of carbenium ions, thereby influencing the MTO reaction pathway, product diffusion, and product selectivity.[231–233] Liu *et al.*[146,234] reported a cavity-controlled principle in the MTO reaction, showing that the zeolite cavity influences active intermediate formation, reaction pathways, catalyst deactivation, and diffusion. Fig. 12b illustrates

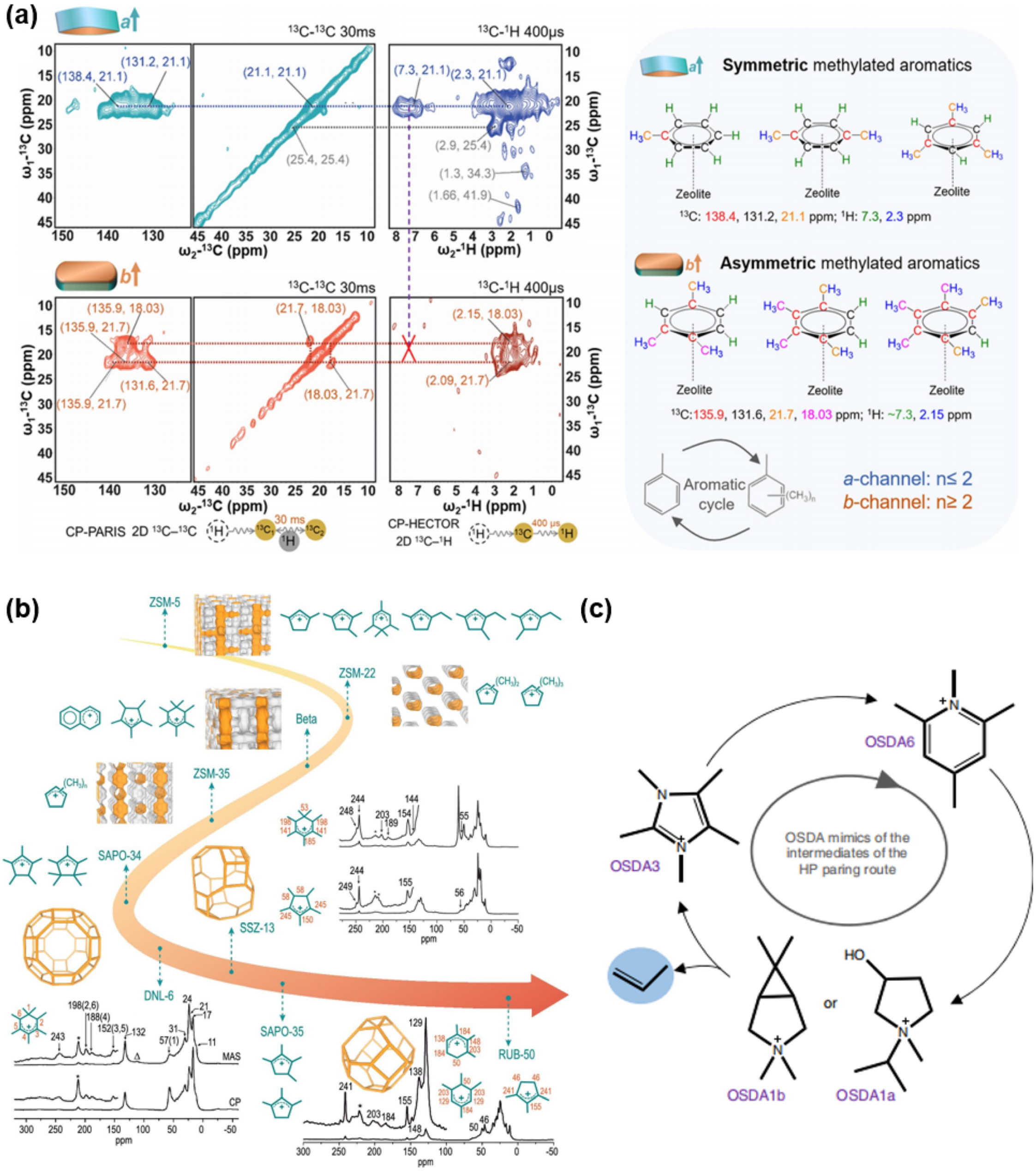

Fig. 12 (a) Identification of rigid methylated aromatics molecules in the *a*-oriented and *b*-oriented zeolite ZSM-5 crystals by 2D ^{13}C–^{13}C and ^{13}C–^{1}H MAS ssNMR spectra after 2 min of the methanol reaction at 623 K. Reproduced with permission from ref. 94. Copyright 2020 Wiley-VCH GmbH. (b) Series of carbenium ions observed in different zeolites by ssNMR spectroscopy during methanol conversion. Reproduced with permission from ref. 234. Copyright 2023 Oxford University Press. (c) Proposed OSDA mimics of the different intermediates present in the HP paring route. Reproduced with permission from ref. 239. Copyright 2018 Springer Nature.

the HCP carbenium ions identified in different zeolites during the MTO reaction. Zeolites with smaller cavities such as SAPO-35 and H-RUB-50 (6.3 × 7.3 Å) predominantly form less-methylated carbenium ions such as trimethylcyclopentenyl and tetramethylbenzenium cations.[234] These intermediates are associated with higher ethylene selectivity. In contrast, zeolites with larger cavities such as SAPO-34 (6.3 × 10 Å), SSZ-13 (7.3 × 12 Å), and DNL-6 (11.4 × 11.4 Å) facilitate the formation of more-methylated carbenium ions including pentamethylcyclopentenyl and hexamethylbenzene ions, leading to increased propylene production. These basic principles provide a possibility to subtly control the MTO product distribution by the design and synthesis of the molecular sieve catalyst. For instance, Liu *et al.*[235] synthesized an ultra-small cage structure SAPO-14 molecular sieve with a narrow 8-MR channel, realizing the propylene selectivity as high as 77.3% in the MTO reaction.

Independently, the research group of weckhuysen[236] observed that differences in the size and shape of the zeolite cages resulted in the retained distinct HCP species. These variations, in turn, led to lattice expansions of differing magnitudes and directions in CHA, DDR, and LEV topologies. The concept of "cage-defining ring size" introduced by Davis and co-workers[237] further clarifies the relationship between the zeolite structure and the olefin selectivity. This parameter is defined as the minimum number of tetrahedral atoms, forming the ring that encircles the center of the framework cages in the molecular sieve topology. Specifically, zeolites with 12-membered cage-defining rings such as CHA, AFX, and SFW topologies exhibit ethylene selectivity similar to that of propylene. Conversely, zeolites with smaller cage-defining ring sizes such as LEV and ERI produce higher ethylene than propylene; while those with larger cage-defining rings such as DDR and ITE generate more propylene than ethylene. These findings reveal the critical influence of zeolite cavity size and cage-defining ring size on the nature of confined carbenium ions, which, in turn, dictate MTO activity and product. Utilizing the host–guest interaction between zeolite frameworks and HCP species enables the synthesis of zeolites with desired topologies and improved performance.[238] By leveraging an in-depth understanding of the MTO mechanism, Corma and colleagues[239] introduced an innovative approach by utilizing the *ab initio* design of organic structure-directing agent (OSDA) molecules guided by the key hydrocarbon pool intermediates, facilitating the synthesis of specific zeolite structures using HCP mimics as OSDAs (Fig. 12c). The obtained catalysts exhibit a much higher selectivity toward propylene (up to 45%) in MTO reactions, owing to the favored paring mechanism on these zeolites.

3.3. Elucidation of the mechanism of catalyst deactivation

The HCP species trapped inside serves as a scaffold for the formation of PAHs, ultimately leading to catalyst deactivation. Deactivation primarily results from coke deposition, which occurs both inside the micropores and on the external crystal surface, thereby blocking micropores, occluding active sites, and reducing olefin production. Given the intricate reaction networks involved, catalyst deactivation is closely linked to conversion rates, product selectivity, and catalyst lifetime, significantly influencing reactor design (*e.g.*, fluidized bed *vs.* fixed-bed reactors) and process optimization in industrial applications. For example, in the SAPO-34-catalyzed MTO reaction, rapid deactivation arises due to coke accumulation within large supercages, exacerbated by the restricted diffusion imposed by the narrow 8-membered ring (8-MR) pore openings.[240] Consequently, fluidized-bed reactors with continuous reaction-regeneration cycles are employed to sustain catalyst activity. In ZSM-5-catalyzed MTP processes, external coke formation is responsible for the deactivation.[192,241] The 10-MR channel of ZSM-5 imposes spatial constraints that limit the formation and diffusion of larger aromatic species. As a result, fixed-bed reactors are typically employed to accommodate the gradual deactivation behavior of the catalyst. Understanding these zeolite deactivation mechanisms is crucial for comprehending the entire MTO reaction process and serves as a theoretical foundation for improving the industrial process efficiency.

Numerous studies have reviewed catalyst deactivation by coke formation and discussed the impact of acidity on carbon deposition.[35,44,242] Over the past decade, multi-technique approaches have been developed to analyze coke composition, spatial distribution, and formation pathways.[240,243,244] Typically, the insoluble coke composition is analyzed by dissolving the zeolite framework in HF, followed by chromatographic (GC/GC-MS, HPLC) or spectroscopic (NMR, MALDI-TOF/MS) analyses.[245–247] However, this dissolution and extraction procedure provides the chemical compound of the confined species (mixture mainly composed of aromatics and polycyclic aromatics) at the cost of destroying the catalyst structure. SsNMR acts as a complementary technique to provide valuable information of the insoluble coke species, the interaction or spatial correlation between various species involved in deactivation, the structural change and the influence of deactivated catalysts on diffusion without damage to the catalyst structure. Additionally, the spatial distribution of coke species in catalyst particles is visualized with analytical tools, including SEM,[248] TEM,[249] atom probe tomography (APT),[250,251] structured illumination microscopy (SIM),[252] and confocal fluorescence microscopy (CFM).[253–255] In this review, we mainly focus on the application of ssNMR as a complementary technique for investigating catalyst deactivation in the MTO process, providing additional insights beyond the existing reviews on this topic.

3.3.1. Coke deposition and the interaction between coke precursors. The complexity of deactivation in the MTO process arises from the diverse types and structures of coke deposits, which are influenced by multiple factors. These include the catalyst framework, acidity, crystal size, and operating conditions such as reaction temperature, pressure, and feed composition. Coke formation and deactivation mechanisms vary with reaction temperature, even for the same catalyst type. Considering the exothermic nature of the MTO reaction, initiating methanol conversion at lower temperatures to utilize the reaction heat to maintain the target temperature seems a promising strategy for energy savings. However, when the reaction is operated at a temperature in the range of 573–623 K, the SAPO-34-catalyzed MTO process exhibits an obvious induction period accompanied by rapid deactivation.[256] Studies on temperature-programmed methanol conversion in a micro-scale fluidized-bed reactor show temperature-dependent behaviors that significantly influence catalyst performance. As shown in Fig. 13a, methanol conversion initiates around 523 K, with a notable conversion increase at the temperature range of 573–598 K.[20] While a decline in methanol conversion occurs between 598 and 623 K, followed by partial recovery above 673 K. Further studies observed the catalyst deactivation of methanol conversion at low temperatures displays a yellow colour, which is distinctly different from the typical blackish-green in catalysts deactivated at higher temperatures.[257] At higher temperatures, the coke deposits are generally more aromatic, which correlates with a shorter induction period and an extended catalyst lifetime. In contrast, at lower temperatures of 623 K, the coke formed tends to be less aromatic and more saturated, possibly comprising species such as methyladamantanes (Fig. 13a, right). This was corroborated by ^{13}C MAS NMR spectroscopy, which identified the characteristic adamantane signals in the deactivated catalyst. The encapsulation of adamantane species within the CHA cages restricts the formation of HCP species on BAS, leading to a more severe deactivation. These adamantane species convert into naphthalene derivatives, eventually forming polycyclic aromatics, which temporarily restore MTO activity but ultimately cause permanent deactivation of SAPO-34. In industrial MTO processes, reactors are preheated to temperatures exceeding 623 K before introducing the methanol feedstock. This practice is essential

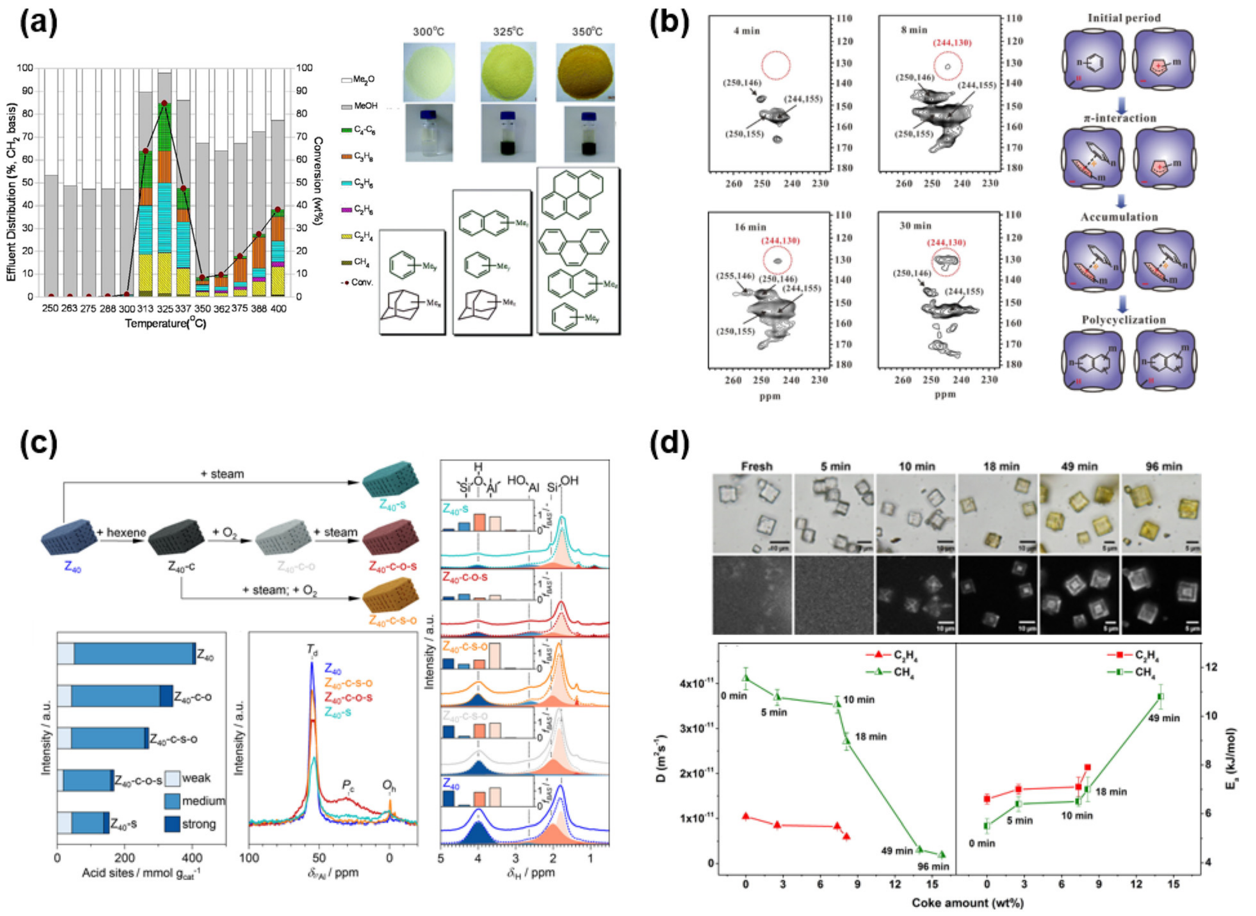

Fig. 13 (a) Effluent distribution of fluidized-bed methanol conversion on SAPO-34 under the condition of programmed increase of temperature (left) and the confined coke after methanol conversion at 573, 598 and 623 K (right). Reproduced with permission from ref. 20 and 257. Copyright 2015 American Chemical Society and 2012 Royal Society of Chemistry. (b) Two-dimensional ^{13}C–^{13}C PDSD spectra of retained species obtained from a ^{13}C methanol reaction over H-SSZ-13-LS at 573 K for 4–30 min (left) and models for the formation of polyaromatics in zeolite channels through the reaction of aromatics with cyclopentenyl cations (right). Reproduced with permission from ref. 260. Copyright 2020 John Wiley and Sons. (c) Total acidity, ^{27}Al, and ^{1}H MAS NMR spectra of H-ZSM-5 (Z_{40}) catalysts after steaming, 1-hexene cracking, or a combination of thereof, followed by oxidative regeneration. The color code in the insets corresponds to that of the deconvoluted spectra. Both reactions were performed at T = 773 K and P = 1.6 bar. Reproduced with permission from ref. 262. Copyright 2024 American Chemical Society. (d) Top: Bright field images and confocal fluorescence microscopy images of SAPO-34 crystals after MTO conversion at 673 K for various reaction times. Down: The variation in intracrystalline self-diffusion coefficients of CH_4 and C_2H_4 at 298 K and diffusion activation energies determined in the temperature range 298–328 K in fresh and spent SAPO-34 as a function of coke amount. A loading of 0.5 molecules per cage is used. Reproduced with permission from ref. 105. Copyright 2018 Elsevier.

to prevent the formation of methyladamantanes—cage-like hydrocarbons that can cause rapid catalyst deactivation by blocking the pores of the zeolite catalysts. By maintaining appropriate preheating protocols, industrial operations balance the thermodynamic efficiency with catalyst longevity, optimizing the overall performance of the MTO process.

While elucidating the precise structure of heavy coke species by ssNMR spectroscopy remains a challenge due to the overlapping NMR signals of structurally similar aromatic compounds, recent advancements have improved its applicability for gaining deeper insights into the correlations of hydrogen atoms with coke species. In 2024, Paunovic *et al.*[258] investigated coke deposition in MTH reactions using 2D ^{1}H–^{1}H DQ–SQ MAS NMR to establish the spatial correlations between different hydrogen atoms from methylbenzenes, naphthalene, PAHs, and the aliphatic substituents on the deactivated catalyst. Furthermore, DNP-enhanced ssNMR has been employed to examine the spatial distribution of coke species in fluid catalytic cracking (FCC) catalysts.[259] This approach revealed that aromatic coke species are primarily surface-exposed, whereas aliphatic species penetrate deeper into FCC catalyst particles.

Although bulky PAHs formed by the continuous accumulation of the cyclic HCP species are often considered as the deactivating species in MTO catalysts, the formation pathways of these species remain controversial. Deng *et al.*[260] revealed that π-interaction-induced spatial proximities between HCP species (cyclopentenyl cations) and aromatics dictate the formation of naphthalene inside H-SSZ-13 zeolite. This was demonstrated using 2D ^{13}C–^{13}C PDSD NMR spectroscopy, confirming the intermolecular proximity of HCP species and aromatics after ^{13}C-methanol reaction over H-SSZ-13 zeolites at 573 K for 8–30 min (Fig. 13b). Furthermore, the normalized intensity of the correlation peak increased linearly over time, suggesting that closer spatial interactions enhance PAH formation. Notably, this correlation peak was barely detectable in high-silica H-SSZ-13, indicating that the acid site density directly affects HCP distribution and thus modulates intermolecular interactions critical to PAH formation. More recently, a cage-passing growth mechanism was proposed on SAPO-34 in which three- to four-ring aromatic hydrocarbons are initially formed within the separate cages and function as the primary coking units/clustering species, subsequently becoming cross-linked with those in neighbouring cages.[247] The molecular structures of coke species were along with the specific cage structures and dimensions. This mechanistic understanding not only sheds light on host–guest chemistry in heterogeneous catalysis but also provides a solid theoretical foundation for optimizing precooking strategies in the MTO reaction.[227]

3.3.2. Acid site evolution and mass transport limitations of deactivated catalysts. The formation of carbon deposits significantly impacts methanol conversion by modifying catalyst acidity, blocking pore entrances, and restricting mass transport, ultimately leading to a severe decline in catalytic performance. Besides identifying the nature and location of the coke species in zeolites, it is essential to understand the structural and property changes of catalysts throughout reaction-regeneration cycles, particularly under elevated temperatures in industrial MTO processes.

In 2013, Li and Hunger *et al.*[261] employed ^{1}H MAS NMR spectroscopy assisted with an NH_3 probe molecule to monitor the densities of accessible BAS and active HCPs as a function of time-on-stream (TOS) on SAPO-34 samples from a fix-bed reactor. During the active phase of the catalyst lifetime, a rapid decrease in the density of accessible BAS was observed due to HCP formation on BAS sites. As polycyclic aromatics progressively blocked the pores, BAS became undetectable by ^{1}H MAS NMR. Interestingly, a later study from the same group showed that upon regeneration of SAPO-34 in synthetic air at 873 K, BAS was fully restored, with intensities comparable to those of the fresh catalyst. In 2024, Paunovic and coworkers[262] used a combination of ssNMR, IR, and UV-Vis spectroscopic techniques to systematically investigate the structural changes of ZSM-5 catalysts during MTH reaction-regeneration cycles. ^{27}Al and ^{29}Si MAS NMR spectra provided evidence of dealumination in ZSM-5 frameworks, primarily due to steam generation during MTH reactions (Fig. 13c). Notably, dealumination reduced BAS concentrations, initially accompanied by a rise in LAS. Structural analysis revealed that aluminum loss was more pronounced in the channels than in the intersections, leading to the formation of penta- and hexacoordinated detached aluminum species. Further investigation using 2D ^{27}Al–^{27}Al DQ–SQ MAS NMR demonstrated that a significant fraction of the detached aluminum species remained in close proximity to the framework aluminum sites. These aluminium redistribution processes lead to a decrease in catalyst activity and alter the reaction rates, reducing the selectivity of C_{3+} alkenes and lowering catalyst turnover capacity due to the enhanced formation of coke precursors.

Deactivation is known to depress the conversion of methanol and limit mass transport by blocking pore entrances in catalytic processes. To probe the internal pore structure and local chemical environments during methanol conversion, HP ^{129}Xe NMR spectroscopy was applied on SAPO-34 (crystal size of 7–10 μm) under mild conditions.[105] A sharp reduction in the ^{129}Xe intensity adsorbed in the spent SAPO-34 catalyst, compared to the fresh catalyst, implied that CHA cavities were occupied by coke species. In addition, PFG NMR measurements using methane and ethene as probe molecules have demonstrated a reduced self-diffusion coefficient associated with increased diffusion activation energy (Fig. 13d). As coke species evolved, spatial heterogeneity in SAPO-34 crystals led to further diffusion constraints, reducing reactant accessibility to active acid sites and thereby accelerating MTO catalyst deactivation, particularly in cavity-type SAPO catalysts with narrow pore openings. By combining fluorescence microscopy with spectroscopic techniques, Weckhuysen and co-workers[253] established a direct correlation between the pore architecture and the molecular transport dynamics. These advancements in integrated imaging techniques offer critical insights into catalyst structural evolution, facilitating optimized catalyst design and process improvements in industrial MTO applications.

Understanding the coke formation or deposition mechanism is essential for mapping the entire reaction process, from the activation of reactant to catalyst deactivation. These insights provide fundamental guidance for catalyst optimization and process design. We will discuss key strategies in these two areas:

(1) Catalyst optimization. Many studies have revealed that reducing the SAPO-34 crystal size can increase the surface area and shorten diffusion paths, thereby improving mass transfer efficiency.[1] In MTO industrial catalysts, specially designed nano-sized SAPO-34 molecular sieves are typically used.[42] Another approach is the introduction of hierarchical pore structures, where mesopores or macropores are incorporated into the microporous SAPO-34 to enhance the internal mass transfer.[263,264] In addition, the existence of inactive siliceous exterior rim of Si-zoned ZSM-5 particles introduces surface passivation, reducing the diffusion limitations and extending the catalyst lifetime by reducing coke accumulation on external surfaces.[265] Importantly, the catalyst should simultaneously possess the mechanical strength to withstand attrition and thermal stresses in fluidized-bed reactors and regenerators in practical applications.

(2) Process optimization for catalyst regeneration. To solve the rapid deactivation of SAPO-34, a fluidized bed reactor is used with a reaction-regeneration cycle in the industry to remove coke and restore catalytic activity.[20] Based on a comprehensive understanding of coke evolution on SAPO-34, Ye and Liu *et al.*[228] developed a regeneration strategy by steam cracking to directionally transform coke into active HCPs (naphthalenic species) within nano-confined spaces in industrially relevant SAPO-34 zeolites. This approach effectively restores catalytic activity, enhances light olefin selectivity, and generates minimal flue gas emissions with negligible CO_2 release (a detailed discussion is presented in Section 3.4.3).

3.4. Effect of water in the MTO reaction

In the MTH reaction, water is an unavoidable dominant byproduct, and its presence significantly impacts catalyst stability, adsorption behavior, and diffusion processes, ultimately influencing the overall reaction performance.[243,266,267] In industrial MTO processes, typically conducted at 673–773 K using SAPO-34 catalysts, co-feeding water dilutes reactant partial pressures and removes excess heat from the reactor. In addition, cofeeding water with methanol enables modulating the catalyst deactivation, as water can modulate HCP formation, reduce coking rate, and enhance olefin selectivity and catalyst lifetime.[27,268,269] This section summarizes the impact of water on different stages of MTO reaction, as revealed by ssNMR studies.

3.4.1. Influence on active sites and stability of catalysts. During the MTH conversion process, water interacts dynamically with the catalyst framework through water adsorption, reversible hydrolysis and irreversible hydrolysis of T–O–T bonds (from weak to strong). The extent of these interactions depends on reaction conditions, including temperature, pressure, and water content. Recent studies have demonstrated that under mild hydrothermal conditions (373–573 K), water can dynamically and reversibly break and reform T–O–T bonds in SAPO-34.[270] By treating a SAPO-34 catalyst with gaseous $H_2{}^{17}O$, 1D and 2D ^{17}O MQMAS spectra confirmed the formation of Si–^{17}O–Al and P–^{17}O–Al species (Fig. 14a). Leveraging this framework flexibility (dynamic and reversible breaking and forming of T–O–T bonds), bulky probe molecules (*e.g.*, trimethylphosphine (TMP) and pyridine) were successfully encapsulated within CHA cavities *via* 8-MR windows, enabling accurate identification of four distinct BASs through 2D ^{1}H–^{31}P HETCOR and REDOR experiments. More importantly, this strategy enhanced light olefin selectivity and the ratio of ethene to propene in the MTO reaction, owing to the extra diffusion restrictions with TMP/pyridine encapsulation. This water-induced reversible process of SAPO-34 not only reveals the interactions between gaseous water and the framework of molecular-sieve under mild hydrothermal conditions, but also provides an effective "ship-in-a-bottle" approach for optimizing catalysts and manipulating shape selectivity in the MTO reaction.

While SAPO-34 exhibits high hydrothermal sensitivity, irreversible T–O–T hydrolysis can occur even at room temperature, leading to potential framework degradation. A recent work by Dai *et al.*[271] investigated water-induced structural changes in SAPO-34 catalysts during MTO conversion at 623 K. Using 1D ^{27}Al and ^{31}P MAS NMR, combined with 2D ^{31}P–^{27}Al HETCOR MAS NMR, they observed progressive accumulation of organic deposits inside SAPO-34 pores and cages. These studies revealed that, as MTO conversion progresses, more organic deposits are accumulated within the cages of the SAPO-34 catalyst, covering partial BAS and even some P–O–Al bonds, thereby effectively preventing the framework irreversible hydrolysis.

3.4.2. Modulation of the reactivity of reactive substrates and intermediates. The interactions between water and zeolites enable dynamic tuning of the local structure of adsorbate–zeolite complexes, emphasizing the significance of microenvironmental effects on catalytic performance. Competitive adsorption of water with methanol and propene reduces the accessibility to BAS, thereby lowering the intrinsic methanol reactivity toward SMS formation and inhabiting the formation of bulky HCP species. This interaction induced a more efficient use of the inner part of SAPO-34 crystals, leading to an increase in the length of the induction period.[266] Kung *et al.*[272] reported that the loading amount of water influences the structure of water–methanol complexes formed with BAS protons in H-ZSM-5, thereby affecting the initial rate of methanol dehydration to DME. Water-assisted MTO reactions have been shown to increase the concentration of naphthyl species in SAPO-34, promoting the catalytic reaction cycle with these species and resulting in an increase in ethene selectivity from 49.7% to 57.7%.[269] Additionally, water also serves as a proton transfer mediator, facilitating proton shuttling between the zeolite framework and organic intermediates, thereby reducing the reaction energy barrier for ethene formation.

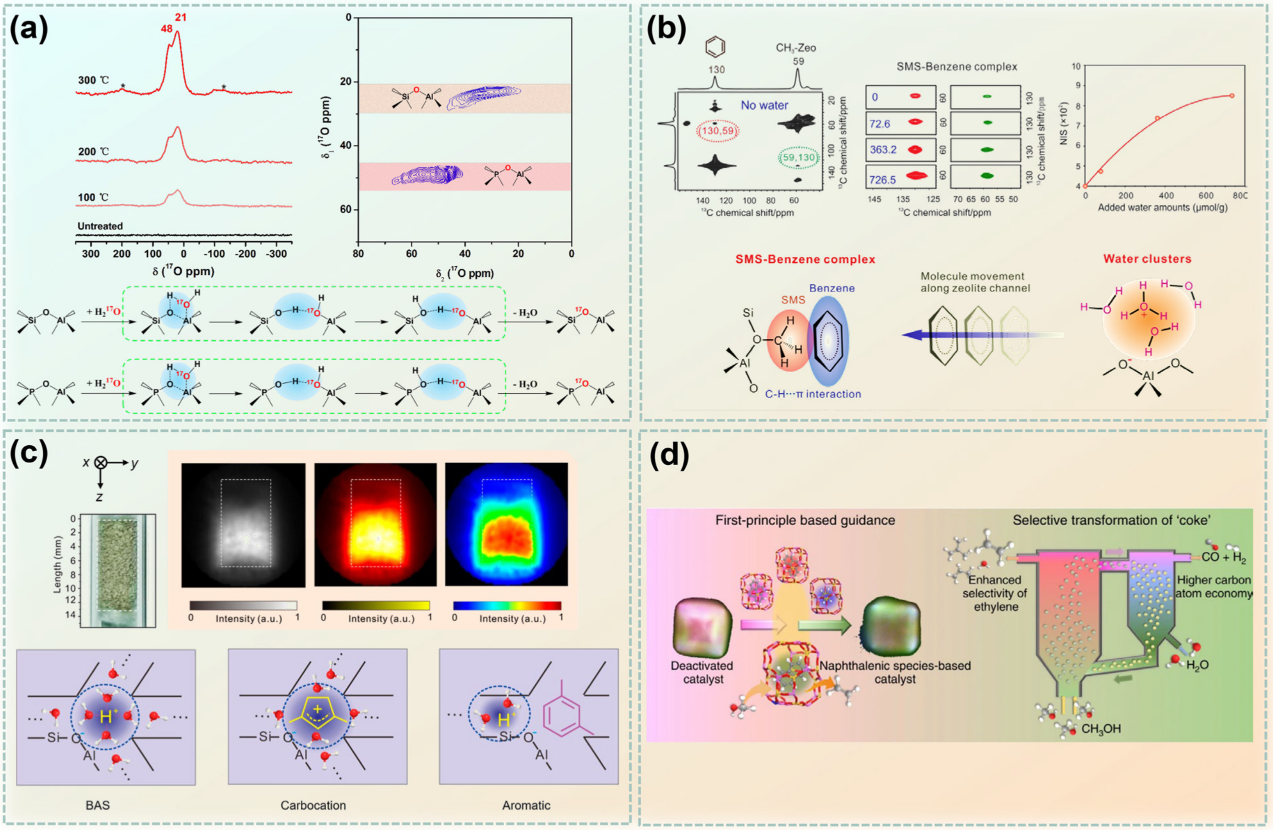

Fig. 14 Influence of water on the MTO reaction. (a) One- and two-dimensional ^{17}O MQMAS NMR spectra of $H_2{}^{17}O$ steamed SAPO-34, and schematic of the proposed route for ^{17}O incorporation from $H_2{}^{17}O$ into the Si–O–Al (top) and P–O–Al (bottom) species. Reproduced with permission from ref. 270. Copyright 2020 John Wiley and Sons. (b) Influence of water on the construction of reactive SMS-Benzene complex over H-ZSM-5. Reproduced with permission from ref. 273. Copyright 2023 John Wiley and Sons. (c) Two-dimensional ^1H MRI images of reacted H-ZSM-5 zeolites exposed to a moist environment (72% humidity) for 60 min. Reproduced with permission from ref. 274. Copyright 2024 American Chemical Society. (d) Schematic of selective transformation of coke into specific intermediates over SAPO-34 catalyst. Reproduced with permission from ref. 228. Copyright 2021 Springer Nature.

In the high-efficiency stage governed by super catalytic cycles, water modulates the reactivity of carbenium ions and regulates the thermodynamics and dynamics of catalytic reaction networks. A water-induced microhydrophobic effect plays a crucial role in improving the methylation reaction between SMS and benzene, which is a key step in the MTH reaction.[273] Multiple dimensional solid-state NMR experiments revealed the formation of SMS-benzene complexes evidenced by the correlation peaks in 2D ^{13}C–^{13}C PDSD MAS NMR spectra (Fig. 14b). The formation of SMS–benzene–water complexes was validated by ^1H–^1H triple-quantum (TQ)-SQ MAS NMR spectroscopy under ultra-fast magic-angle spinning (100 kHz) conditions, demonstrating the spatial proximity of benzene, water, and SMS. ^1H–^{27}Al S-RESPDOR MAS NMR spectra elucidated the spatial proximity between the benzene molecule (^1H) and the BAS (^{27}Al) within zeolite pores, highlighting the role of water in methanol pre-activation and proton transport between organic intermediates and zeolites. Cofeeding water in the MTO reaction impelled that water promotes the catalytic reaction cycle with naphthyl species in SAPO-34, facilitating a highly efficient catalytic cycle to achieve 58% ethene selectivity and extended catalyst lifetime.[269] Additionally, the impact of water on the cyclopentenyl cation reactivity within ZSM-5 pores was explored using micromagnetic resonance imaging (μMRI) and ssNMR techniques.[274] ^{13}C CP MAS spectra of the confined product on the catalyst in a fixed-bed reactor after methanol at 573 K revealed a nonuniform distribution of cyclopentenyl cations and aromatic hydrocarbons, leading to a water adsorption gradient along the fixed-bed reactor (72% relative humidity), as visualized by 2D ^1H MRI images (Fig. 14c). The 2D ^{13}C–^1H HETCOR NMR experiments indicated that BASs and cyclopentenyl cations exhibit higher water adsorption capacities than aromatic hydrocarbons. Specifically, the nucleophilic character of water significantly enhanced the conversion of cyclopentenyl cations to aromatic compounds, reinforcing aromatic-based catalytic cycles and boosting ethene selectivity. These findings reveal the pivotal role of water in manipulating confined carbenium ion reactivity, ultimately tuning the product selectivity in MTH processes.

3.4.3. Influence on catalyst deactivation and regeneration.

Water plays a multifaceted role in the MTO reaction, particularly in mitigating coke formation and thereby extending the catalyst lifetime. The competitive adsorption of water, methanol, oxygenates, HCPs, and coke precursors at BAS reduces the accessibility, thereby slowing the key reaction steps such as formation of initial HCPs, olefin dimerization, cyclization, and hydrogen transfer, ultimately decreasing coke formation. Co-feeding water selectively quenches PAH clustering against the formation of active HCP species on SAPO-34 catalysts under MTO reaction conditions, thereby slowing catalyst deactivation due to coke deposition.[246] While catalyst deactivation due to coke deposition is inevitable, the regeneration of deactivated catalysts can remove coke species while restoring the catalytic activity. Traditionally, air or oxygen is used to oxidize coke species into CO, CO_2, and steam (H_2O), thereby removing and deactivating carbon deposits.[275,276] However, to reduce CO_2 emissions, steam gasification has been employed as a more sustainable alternative, converting coke into valuable syngas rather than fully oxidizing into CO_2. In the MTO process, partially regenerating deactivated SAPO-34 catalysts *via* steam gasification has been proved to enhance ethylene selectivity (compared to air combustion), primarily due to the residual coke in SAPO-34 consisting of active HCPs, such as methylated benzenes and naphthalene.[226,228] Recently, Liu *et al.*[228] have reported that during steam cracking at 953 K, the coke deposits on deactivated SAPO-34 catalysts were selectively converted into active naphthalene species (Fig. 14d). These confined naphthalene species exhibit high stability at high temperatures, promoting an efficient ethylene formation cycle *via* a naphthalene-based catalytic pathway in the MTO reaction. To validate this coke transformation strategy, fluidized-bed reactor-regenerator pilot experiments were conducted at the level of a pilot plant, achieving an unexpectedly high selectivity of 85% for light olefins, with 88% valuable CO and H_2 and only 5% CO_2 as byproducts from regeneration. This strategy effectively regulates the MTO reaction through partial steam gasification of coke species, reducing CO_2 emissions and increasing carbon atom utilization, thereby further enhancing the economic viability of the MTO process.

Despite its complexity, water plays a crucial role throughout all stages of the MTO reaction. In DMTO technology, almost 20% external water is introduced along with methanol vapor, resulting in products containing nearly 75% water (mass fraction). Beyond serving as a heat carrier to dissipate the exothermic energy of the MTO reaction, water helps to reduce the partial pressure, which is beneficial for generating low-carbon olefins (because MTO is inherently a low-pressure process). Moreover, water competes with olefins for adsorption on active sites, thereby facilitating the desorption of olefins and enhancing olefin selectivity.[277] By mitigating the concentration of reactants at these active centers, water also slows down catalyst coking in the MTO reaction.[226,278]

4. Application of ssNMR techniques in DME carbonylation reactions

The MTE process, catalyzed by zeolites, represents another significant advancement in methanol conversion technologies. This process encompasses the initial dehydration of methanol to DME, followed by the carbonylation of DME with CO to yield MA, which is subsequently hydrogenated to produce ethanol.[28,29,31,279] The pivotal step in this sequence is the selective carbonylation of DME to MA, a reaction typically conducted at temperatures ranging from 423 to 573 K under high pressures from 2 to 5 MPa using MOR zeolites characterized by their unique 8-MR and 12-MR pore structures.[31] The DME carbonylation mechanism exhibits notable parallels with the MTO reaction, particularly concerning the evolution of SMS, which are crucial for the initial C–C bond formation and subsequent product development. Both processes progress through stages of induction, high-efficiency reaction, and rapid deactivation. Considering the economic significance of ethanol as the primary MTE product, there is a pressing need for further investigation into DME carbonylation.[31] Fundamental research not only deepens our mechanistic understanding but also drives industrial advancements, paving the way for more efficient and sustainable processes in methanol conversion.

The development of DME carbonylation technology has advanced rapidly from mechanistic discovery to industrial implementation, as illustrated in Fig. 15. In 1984, Fujimoto *et al.*[280] investigated methanol carbonylation on various zeolites including H-Y, H-ZSM-5, H-MOR, as well as Cu-modified zeolites, establishing a foundation for subsequent research. The MOR zeolite has a one-dimensional channel system consisting of 12-MR channels and narrower 8-MR channels, which are connected by 8-MR side pockets. In 2006, Iglesia *et al.*[279] demonstrated that DME carbonylation over H-MOR achieved high reaction rates with 99% MA selectivity, attributing this performance to the unique pore structure and acid site distribution of the MOR zeolites. Subsequent studies in 2007 confirmed the correlation between catalytic performance and the number of BAS in the 8-MR side pocket.[281] The confinement effect and acid site distribution within these structures play a critical role in enhancing DME carbonylation activity and selectivity. In 2010, Shen *et al.*[282] enhanced the stability of H-MOR through pyridine modification, solving the problem of rapid catalyst deactivation. In 2013 and 2015, Deng *et al.*[78] and Bao *et al.*,[79] using various *in situ* ssNMR techniques, directly detected acetyl species, further validating the proposed reaction mechanism.

Liu *et al.*[298] has pioneered the use of the DMTE (dimethyl ether to ethanol) process to produce ethanol from DME *via* MA. Starting with methanol as the feedstock, the process includes: (1) a methanol dehydration unit to generate DME, (2) a DME and CO carbonylation unit to produce MA, and (3) a MA hydrogenation unit to yield ethanol as the final product, with the generated methanol recycled back into the reactants. Thus, the net reaction converts methanol and syngas into ethanol (Fig. 16). Methanol feedstock can be sourced through multiple pathways, including syngas-to-methanol conversion, which has already been industrially implemented, CO_2 hydrogenation with green hydrogen and biomass-based routes for green methanol production, both of which hold potential for future realization. Additionally, innovative approaches for utilizing CO resources (such as steel plant tail gas and coke oven gas)

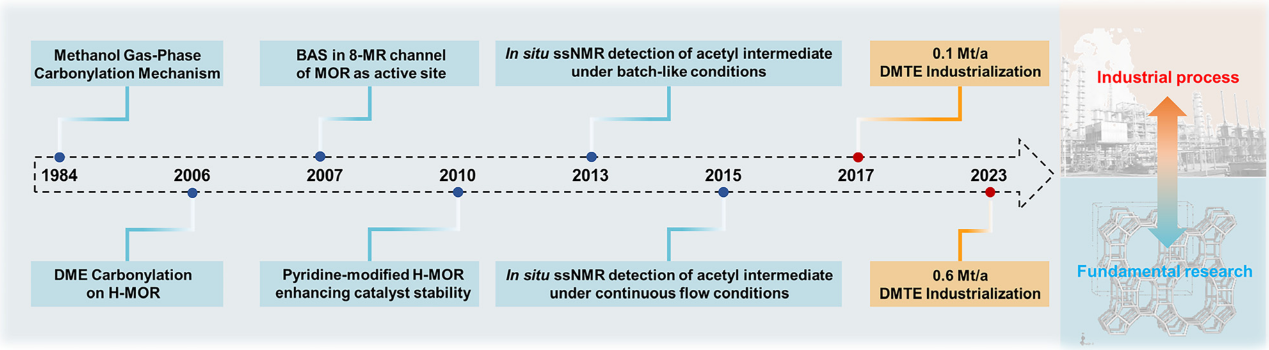

Fig. 15 Milestones in the fundamental research and industrial development of the DME carbonylation process.

promote low-carbon integrated development across industries such as steel, energy, and environmental sectors. In collaboration with Shaanxi Yanchang Petroleum (Group), the world's first 0.1 Mt a^{-1} ethanol demonstration project was launched in 2017. Subsequently, the technology was extended to the steel industry, and a 0.6 Mt a^{-1} ethanol production plant was ultimately completed in 2023. Thus far, DMTE technology has been licensed for 14 commercial units with an annual ethanol production capacity of 4.55 Mt a^{-1}. Notably, this process utilizes an anhydrous system for carbonylation and hydrogenation, enabling direct anhydrous ethanol production while circumventing the challenges associated with ethanol-water azeotropes. The carbonylation and hydrogenation processes generate minimal acetic acid, resulting in low system corrosivity. This significantly reduces the acid corrosion resistance requirements for reactor materials, greatly enhances equipment operational safety, and substantially reduces costs. Additionally, high-performance zeolite-based catalysts substitute noble metal catalysts, enhancing economic feasibility. Flexible MA and ethanol configurations further improve market competitiveness. Different from fluidized-bed reactors used in MTO processes, fixed-bed reactors are employed in the DME carbonylation reaction due to their ease of scale-up and operational simplicity.

Despite the industrial success of DME carbonylation technology, several scientific issues remain unresolved, particularly concerning the mechanistic intricacies and catalyst optimization. Core scientific issues such as detailed reaction mechanisms and the direct correlation between fundamental research and industrial applications remain underexplored.[29,283] This review emphasizes the following aspects: (1) the roles of 8-MR and 12-MR pore channels in MOR zeolites, (2) the distinction of non-equivalent T sites in MOR zeolites, (3) the impact of water on the carbonylation reaction of DME, and (4) strategies for modifying MOR zeolites to enhance the catalytic performance. By systematically addressing these aspects, this review aims to deepen the mechanistic understanding of DME carbonylation and foster advancements in catalyst design.

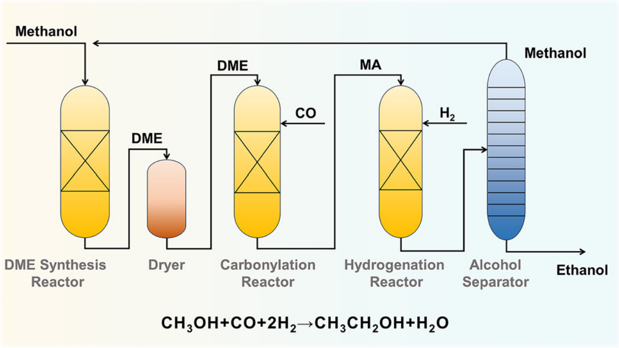

Fig. 16 Simplified process diagrams for DMTE technologies.

4.1. Roles of 8-MR and 12-MR channels in DME carbonylation of MOR zeolites

The exceptional catalytic performance of MOR zeolites with 99% selectivity to MA is attributed to the unique pore architectures. As illustrated in Fig. 17a, MOR zeolites feature large 12-MR channels (7.0 × 6.5 Å) and smaller 8-MR channels (5.7 × 2.6 Å), connected by side pockets (4.8 × 3.4 Å).[34,279,281,284,285] This well-defined structure facilitates the precise progression of the carbonylation process, leading to high MA selectivity. Understanding the specific roles these channels play is crucial for elucidating the reaction mechanism and optimizing catalyst design. In this section, we will focus on the key reaction intermediates (*e.g.*, methoxy, acetyl species, and ketene species) and the roles of 8-MR and 12-MR channels of MOR zeolite in DME carbonylation reactions.

4.1.1. Key intermediates. The carbonylation reaction begins with the activation of DME on BAS to form SMS and methanol. Subsequently, CO inserts into the C–O bond of the SMS, yielding a surface acetyl group. This acetyl group then reacts with another DME molecule to produce one molecule of MA and releases an additional methoxy group (Fig. 17b).[285]

SMS governs the C–C coupling between SMS and CO during DME carbonylation. Zheng *et al.*[169] revealed the stepwise mechanism of SMS formation from methanol and DME in the MOR through AIMD free energy barrier calculations, demonstrating the critical role of DME in SMS generation. Based on AIMD calculations, methanol in the 8-MR channel follows a bimolecular mechanism: the methanol molecule near

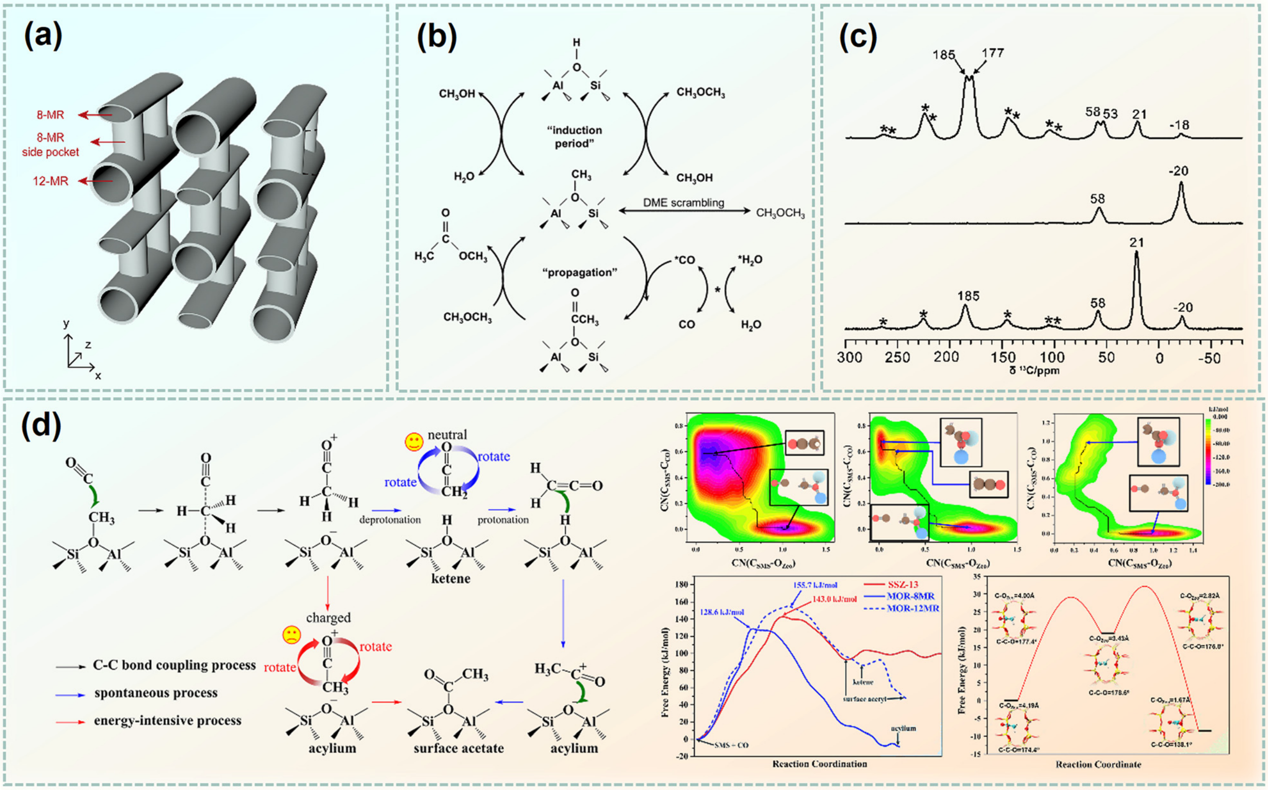

Fig. 17 Key intermediates in the DME carbonylation process on zeolites. (a) Structure of MOR. Reproduced with permission from ref. 293. Copyright 2023 Elsevier. (b) Mechanism of DME carbonylation with CO on H-MOR. Reproduced with permission from ref. 285. Copyright 2007 Elsevier. (c) Detection of the acetyl species through *in situ* ssNMR techniques. Reproduced with permission from ref. 78. Copyright 2013 American Chemical Society. (d) Left: Routes leading to surface acetyl in MOR and SSZ-13 with and without participation of ketene: pathway in MOR-12MR and SSZ-13 (blue Arrows) and in MOR-8MR (red Arrows). Right: Two-dimensional free energy profiles and primary product of C–C bond coupling between SMS and CO in MOR-12MR (top, left), MOR-8MR (top, middle), SSZ-13 (top, right) based on MTD-AIMD. The black lines represent the minimum free energy paths (MFEP) (down, left). Free energy surfaces of acylium ion to surface acetyl in MOR-8MR (down, right). Reproduced with permission from ref. 286. Copyright 2021 American Chemical Society.

BAS first undergoes protonation, while the second methanol acts as a methyl transfer agent to generate $DMEH^+$ and water. After water desorption, $DMEH^+$ forms SMS at the BAS while regenerating methanol. DME follows a similar stepwise SMS formation mechanism, but exhibits significantly lower free energy barriers in 8-MR (74.6 kJ mol^{-1}) than methanol in 8-MR (124.9 kJ mol^{-1}) and DME in 12-MR (159.3 kJ mol^{-1}), making 8-MR channel the preferential position for DME-derived SMS formation.

The detection of acetyl species has attracted widespread attention and has been validated by various methods such as kinetic analysis and DRIFT spectroscopy.[281,286,287] Here, we specifically focus on the observation of acetyl species *via* ssNMR spectroscopy. Deng *et al.*[78] identified acetyl species as key intermediates in DME carbonylation through ^{13}C MAS NMR spectroscopy on H-MOR zeolites. Their work employed sealed glass ampoules operating under batch-like conditions. The co-adsorption of ^{13}CO and $^{13}CH_3I$ at 473 K produced carbonyl (185 ppm) and methyl (21 ppm) species, confirming the formation of acetyl species (Fig. 17c). This finding was further supported by CSA analysis, as the calculated isotropic chemical shift of the acetyl group in the 8-MR (184.2 ppm) closely matches the experimentally measured surface acetyl chemical shift (185.3 ppm). Subsequently, Bao *et al.*[79] used continuous-flow ssNMR technology to monitor the formation and evolution of acetyl species, where the acetyl signal at 169 ppm was unambiguously identified through the integration of ^{13}C CP MAS NMR spectrum and DFT calculations.

The reaction pathway proceeds through CO insertion into SMS to form acetyl carbocation intermediates, which subsequently undergo competitive conversion to ketene species at BAS. While ketene may further reorganize to regenerate acetyl groups, the remarkably low energy barrier (12-MR: 17 kJ mol^{-1}, 8-MR: 12 kJ mol^{-1}) of this step results in an extremely low steady-state concentration of ketene, rendering it experimentally undetectable under conventional analytical conditions.[288,289] Jensen *et al.*[290] identified ketene as a key intermediate in DME carbonylation of MOR zeolites through a combination of DFT calculations and isotopic experiments. The introduction of D_2O into the CO/DME feed during MA synthesis yielded doubly deuterated acetic acid (CH_2DCOOD, *m*/*z* = 62) in mass spectrometry analyses. This observation provides mechanistic evidence that ketene intermediates are exclusively involved in this pathway, as all alternative reaction routes would generate monodeuterated CH_3COOD (m/z = 61) through non-ketene-mediated deuterium incorporation. Zheng *et al.*[286] advanced the mechanistic understanding by integrating AIMD simulations, SXRD, and FT-IR spectroscopy to elucidate the critical role of ketene and its derivatives (specifically, acylium ions and surface acetyl groups) in direct C–C bond coupling during DME carbonylation (Fig. 17d). Within the 8-MR channels, the highly selective formation of ketene leads to exceptionally stable acylium ions, demonstrating superior reactivity for catalytic cycles. Conversely, spectroscopic evidence from FT-IR investigations revealed that ketene presenced in 12-MR channels promotes unfavorable pathways, including dimerization and carbonaceous precursor formation, which accelerate catalyst deactivation. This work underscores the role of framework confinement effects on ketene speciation, which dictate either selective C–C coupling or detrimental side reactions, thereby highlighting the structure-dependent reactivity in zeolite catalysis. Building upon prior mechanistic studies, Hou *et al.*[291] have recently expanded the catalytic repertoire of zeolite-mediated ketene transformations by systematically investigating the conversion of ketene to gasoline-range hydrocarbons within the confined channels of H-SAPO-11.

4.1.2. Synergistic role of 8-MR and 12-MR. The BAS within the 8-MR channels of MOR zeolites is recognized as the primary active sites for DME carbonylation.[281,292] A linear correlation exists between MA formation rates and the density of BAS in 8-MR channels by kinetic and spectroscopic probe experiments (Fig. 18a).[281] Notably, according to quantum chemical calculations, the T3–O33 site within the 8-MR side pocket exhibits higher activity due to its spatial configuration, which promotes carbonylation while minimizing side reactions (*i.e.*, MTH reactions) leading to deactivation.[34] The unique structure of the 8-MR channels imposes spatial constraints on reactants and intermediates, generating a confined environment that enhances selectivity of MA.[292] Moreover, the steric constraints within 8-MR channels influence the spatial distribution of SMS, further directing the reaction pathway toward MA production with minimal by-products (*i.e.*, hydrocarbons).[34] Advanced techniques, particularly ssNMR spectroscopy, have confirmed the role of the 8-MR channel by directly detecting reaction intermediates and their interactions with acid sites.

Deng *et al.*[78] prepared samples with BAS selectively located in the 8-MR and 12-MR channels in MOR, respectively. Samples with BAS in 8-MR channels were prepared *via* pyridine preadsorption, as pyridine is generally considered to bind only to BAS in 12-MR. Samples retaining BAS in 12-MR channels were obtained through Na^+ ion exchange, owing to the preferential occupation of Na^+ in the 8-MR regions. *In situ* ^{13}C MAS NMR spectra revealed that the acetyl signal appeared only in the sample with BAS in the 8-MR region. Bao *et al.*[79] systematically investigated the roles of the 8-MR channels in H-MOR during DME carbonylation by *in situ* continuous-flow ^{13}C MAS NMR spectra. The early appearance of the carbonyl signal in the 8-MR indicates that carbonylation begins within the 8-MR channels, confirming their roles as active sites for the carbonylation reaction. Recent advancements in synthesis and characterization techniques have facilitated deeper investigations into the quantitative analyses of the reaction kinetics of T-site. Shen *et al.*[293] determined the distribution of four T-sites in MOR zeolites using 1D ^{27}Al MAS NMR spectra, 2D ^{27}Al 3Q MAS NMR spectra, and ^{27}Al–^{29}Si correlation ssNMR spectra. The MA formation rate at T3 sites was derived from catalytic evaluations of DME carbonylation using both a benchmark MOR and a plate-like MOR zeolite (specifically synthesized *via* a two-step crystallization method) containing exclusively T3 site Al atoms. Comparative catalytic evaluation of two MOR zeolites with nearly identical framework Si/Al ratios and total BAS quantities, but substantially different T4 site contents, enabled the determination of MA formation rates specifically attributable to T4 sites in DME carbonylation. While both the T3 and T4 sites exhibit carbonylation catalytic activity, the specific activity of T4 is only one-fourth of that of the T3 site.

Additionally, the identification of the rate-determining step in the reaction mechanism requires explicit attention. Iglesia *et al.*[279] determined that CO insertion into SMS to form acetyl intermediates is the rate-determining step, as the rate of MA formation depends on CO partial pressure rather than DME partial pressure. This step is specifically enabled by the unique confined space of the T3–O33 site within the 8-MR channels, as demonstrated by DFT calculations (Fig. 18b).[34,284,294–297] These findings reinforce the central role of 8-MR channel in the catalytic mechanism, which ensures the high activity and selectivity of H-MOR.

The 12-MR channels in MOR zeolites serve as the primary diffusion channel for reactants and products, facilitating efficient product desorption. PFG NMR experiments revealed that blocking the 12-MR channels leads to reducing the effective diffusion coefficients for molecules like methane and DME. Additionally, ^{129}Xe NMR spectroscopy showed that xenon atoms preferentially adsorb in the 8-MR side pockets at low pressures but migrate through the 12-MR channels at elevated temperatures. However, Xe diffusion through the 12-MR channels was hindered when blocking the 12-MR with pyridine (Fig. 18c). Further ^{129}Xe NMR investigation across temperatures ranging from 213 K to 383 K provided additional evidence that the guest molecules primarily diffuse through the 12-MR channel to enter the 8-MR side pockets for the reaction.[107,108] Subsequent research evaluated the impact of surface diffusion resistance in 12-MR channels on catalytic performance. MOR samples exhibiting significant transport resistance display approximately 50% lower apparent activity and reduced stability. However, chemical etching of the outer MOR layer can mitigate surface barriers, enhance mass transport properties, and improve both activity and stability.[298]

However, the BASs in 12-MR channels of MOR zeolites significantly contribute to catalyst deactivation, adversely affecting stability and lifetime. These acid sites can also favor the formation of hydrocarbons, leading to severe deactivation by the deposition of carbonaceous residues.[34,299] Subsequently, these aromatics may transform into carbon deposits, blocking the channels of catalysts and diminishing catalytic activity.

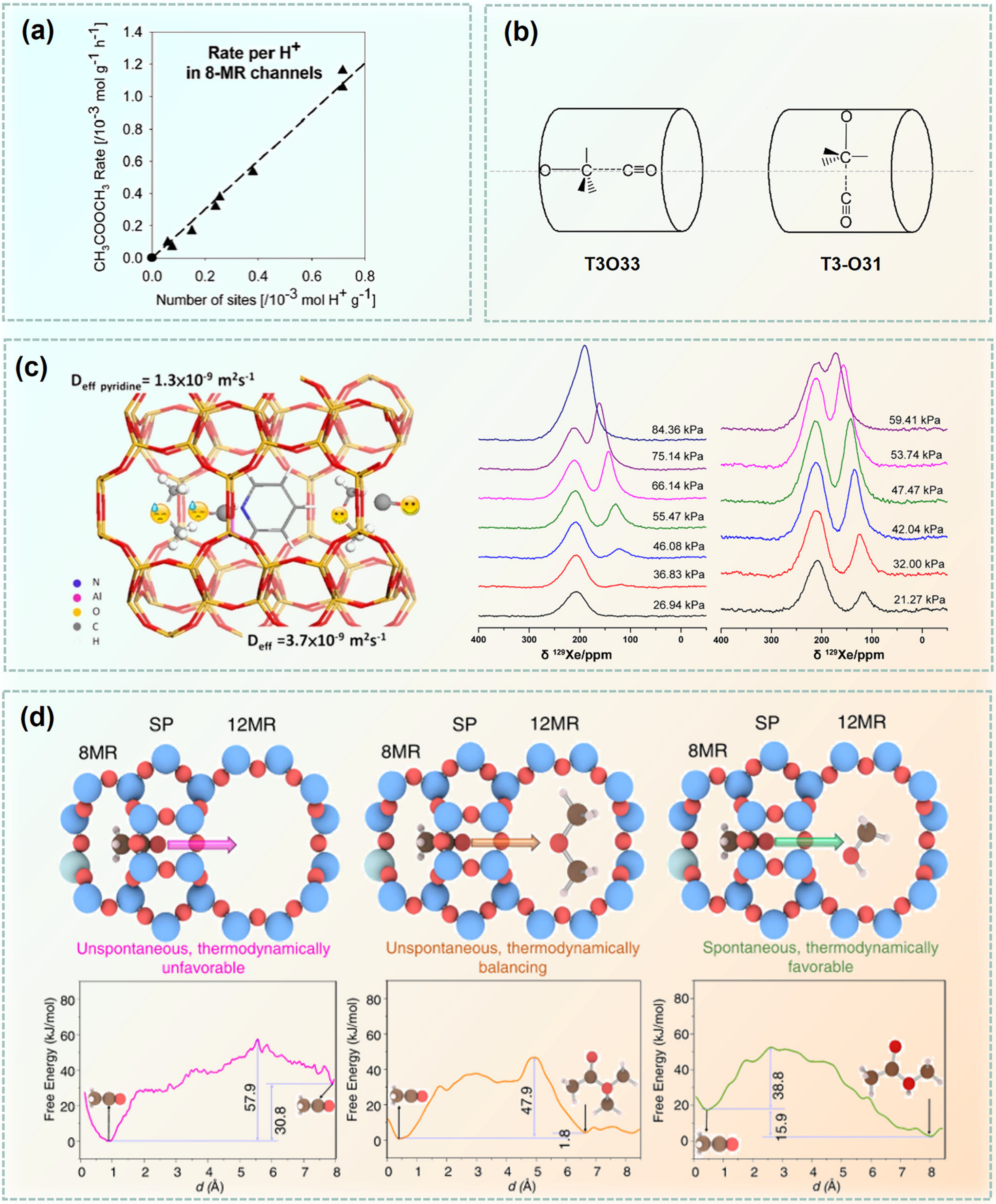

Fig. 18 Roles of 8-MR and 12-MR in H-MOR zeolite. (a) BAS density in the 8-MR is proportional to the MA formation rates. Reproduced with permission from ref. 281. Copyright 2007 American Chemical Society. (b) Schematic of the relative orientation of the $O_{framework}$–CH_3 bond and the channel axis at the T3–O33 position of MOR and any other position in an 8MR channel. Reproduced with permission from ref. 34. Copyright 2008 American Chemical Society. (c) ^{129}Xe NMR spectra of H-MOR and pyridine-modified H-MOR with different loadings of xenon at 213 K. Reproduced with permission from ref. 107. Copyright 2016 American Chemical Society. (d) Migration of the acylium ion from the side pocket to the 12-MR channel. Reproduced with permission from ref. 303. Copyright 2022 Springer Nature.

Theoretical calculations demonstrated that at the T1, T2, and T4 positions in the 12-MR channels of H-MOR, the energy required for the reaction of methoxy group with DME to form TMO^+ is significantly lower than that for reaction with CO to form acetyl groups. The formation of TMO^+, which is typically an active intermediate in the MTO reaction for initial C–C bond formation, is kinetically favorable in the 12-MR channels of H-MOR, and further leads to the generation of carbon deposits.[34,35] Therefore, the occurrence of the MTO reaction and the resulting blockage of the 12-MR channels might be one of the reasons for deactivation in the DME carbonylation reaction. Elucidating the structure and evolution of carbon deposits is crucial for understanding the deactivation process.

Ma *et al.*[300] examined the deactivation behavior of H-MOR and Cu/H-MOR catalysts in DME carbonylation by thermogravimetric analysis (TGA), ^{13}C NMR spectroscopy, FT-IR, UV-vis and N_2 physisorption. Through ^{13}C MAS NMR spectroscopy, they observed an increase in aromatic carbon signal (130 ppm) and a decrease in alkoxy signal (51 ppm) at different TOS. This suggested that alkoxy species were converted into stable aromatic carbon deposits, leading to blockage of the 12-MR channels, thereby hindering the transport of reactants and products. Notably, the BAS in the 8-MR side pockets remained unaffected, indicating that carbon deposition predominantly occurred in the 12-MR channels. UV-vis spectra of spent catalysts exhibit four characteristic bands at 300, 383, 452, and 550 nm, assignable to coke structures ranging from double-conjugated bonds (300 nm) and single-ring aromatics (383 nm) to two-/three-ring systems (452 nm) and highly conjugated polyaromatics (550 nm). Further analyses employing ^{13}C MAS NMR spectroscopy, TGA, and FT-IR elucidated the dynamic evolution of carbon deposits during deactivation.[301] Two types of carbon deposits were identified: soft coke formed early from DME decomposition and gradually covering acid sites, and hard coke generated by polymerization and MA decomposition accompanied by releasing CH_4 and H_2. These deposits primarily accumulated in the 12-MR channels, leading to pore blockage and accelerating deactivation. Additionally, recent studies have identified the formation of cyclic oxygenated species *via* a significant pathway for the deactivation of pyridine-modified H-MOR zeolites.[302] Excess acetyl species formed in the 8-MR side pockets convert into ketenes within the 8-MR and then migrate into the 12-MR to undergo polymerization and decarbonylation, forming cyclic oxygenates that ultimately lead to catalyst deactivation. Liu *et al.*[287] systematically investigated the effects of reaction temperature and pressure on coke formation using *in situ* FT-IR spectroscopy. These findings demonstrated that elevated temperatures and reduced pressures promote the conversion of DME to olefins at BAS on the zeolite, which subsequently accelerates coke deposition. This study establishes quantitative correlations between operating parameters (temperature/pressure) and reaction pathways in DME carbonylation, providing critical guidance for process optimization.

In DME carbonylation, the synergistic interplay between the 8-MR and 12-MR rings of H-MOR zeolites is pivotal for optimizing catalytic performance. The 8-MR channels serve as active sites, while the 12-MR channels function as diffusion pathways. Investigations utilizing ^{13}C MAS NMR spectroscopy with ^{13}C-labeled acetyl chloride ($CH_3{}^{13}COCl$) have shed light on this synergy in which 8-MR side pockets and channels serve as active sites, while the 12-MR channels function as diffusion pathways.[303] Thermal treatment at 333 K resulted in a reduction of acetyl signals in the 12-MR and an increase in acylium ion signals in the 8-MR side pockets. This observation suggested that acylium ions stabilize in the 8-MR side pockets before migrating to the 12-MR channels, where they undergo C–O bond coupling with DME or methanol to produce MA. Additional studies employing AIMD simulations and 2D COS (correlation spectroscopy) FT-IR further validated that the 8-MR channels are for the stabilization of acylium ions *via* C–C bond coupling between SMS and CO.[303] Conversely, the 12-MR channels facilitated C–O bond coupling between the carbonyl group of the newly decoupled acetyl moiety and MeOH oxygen, completing MA formation (Fig. 18d). Furthermore, MD simulations and DFT calculations confirmed that CO preferentially adsorbs in the 8-MR side pockets in H-MOR, promoting the activity of the carbonylation reaction inside MOR zeolites.[304] The 12-MR channels, however, enabled efficient transport and reduced product accumulation, thereby enhancing catalytic efficiency and stability. Comparative studies with other zeolites, such as FER, GON, and ATS zeolites, have demonstrated that the 8-MR of H-MOR enhances CO adsorption, while the 12-MR channels promote rapid diffusion. Zheng *et al.*[28] have recently provided a comprehensive mechanistic insight into DME carbonylation based on multiscale simulations and *in(ex) situ* spectroscopies. They identified three key points: (1) DME is more favorable than methanol for forming SMS, as detailed in Section 4.1.1, (2) the side pocket and 8-MR channel lower the barrier for C–C coupling and stabilize the acylium ion, while 12-MR BAS facilitate ketene formation, (3) the stabilized acylium ion in 8-MR acts as a more active intermediate than surface acetate and migrates *via* the 12-MR channel assisted by DME or MeOH. By utilizing diffusion and reaction free-energy surfaces obtained from AIMD simulations, they developed a unified reaction/diffusion model, showing distinct roles for MOR channels: SMS formation and C–C coupling occurs in 8-MR, while MA formation proceeds mainly in 12-MR. These insights into the roles of 8-MR and 12-MR provide crucial guidance for catalyst synthesis design and industrial development. We will discuss three aspects:

(1) The T3 sites within the 8-MR channels have been identified as primary active centers for DME carbonylation. Catalysts with a higher proportion of T3 sites exhibit improved activity. For instance, increasing the proportion of T3 sites in plate-like MOR zeolites has led to a 60% enhancement in catalytic performance compared to the benchmark MOR. Additionally, the identification of CO insertion into SMS as the rate-determining step highlights the importance of maintaining high CO pressures to enhance efficiency or using metal ion modification with Cu, Zn, and other metals to promote CO activation.[305–313] Industrial processes often employ high-pressure conditions to favor CO insertion, improve reactant adsorption, and shift the reaction equilibrium toward product formation. This optimization enhances reaction kinetics and minimizes side reactions. Fixed-bed reactors, due to their compact structure, simple design, and superior control over reaction conditions, are preferred in industrial

settings, as they ensure catalyst stability while minimizing catalyst loss.

(2) While the 12-MR channel not only serves as a diffusion channel but also facilitates side reactions, optimizing the catalyst size can improve the mass transfer efficiency.[314] Many researchers have explored modifications to MOR zeolites, focusing primarily on two approaches: introducing mesopores or creating hierarchical porosity[315] and controlling the synthesis of nanoscale MOR zeolites and nanosheet assemblies.[316–319] Additionally, identifying key coke precursors and their transformation pathways enables the development of strategies to suppress coke formation, thereby extending the catalyst lifetime and maintaining high catalytic activity under industrial conditions. The MTO reaction, as a contributing factor to catalyst deactivation in DME carbonylation, highlights the necessity of minimizing its occurrence in industrial applications. Since the MTO reaction typically occurs at higher temperatures and lower pressures, while DME carbonylation occurs at lower temperatures and higher pressure, the industrial DME carbonylation process is conducted under relatively low-temperature conditions to reduce side reactions.

(3) The current work suggests that the DME carbonylation reaction relies on the synergistic roles of the 8-MR and 12-MR structures. However, further in-depth studies are needed to confirm this relationship and provide valuable insights for the development of other zeolite structures, such as FER and SSZ-13.[320–325] Systematic exploration of the molecular-level cooperation between the 8-MR and 12-MR structures can guide the rational design of MOR catalysts, ultimately improving their stability and efficiency.

4.2. Distinction of T sites in MOR zeolites by using ssNMR techniques

The silicate framework of MOR zeolites is constructed from interconnected 4-MR and 5-MR, forming a 12-MR main channel along the *c*-axis that interconnects with 8-MR side pockets along the *b*-axis. Within the unit cell, four non-equivalent T sites exist: T1 is located in the 12-MR main channel, T2 and T4 are distributed at the interface between 12-MR and 8-MR regions, and T3 resides within the 8-MR side pockets.[326] In DME carbonylation, the MOR exhibits significantly superior activity and selectivity to other zeolites (*e.g.*, FER).[279] Theoretical calculations by Corma *et al.*[34] have demonstrated that the T3–O33 site exhibits higher selectivity than that of the T3–O31 site. This enhanced selectivity is attributed to the unique spatial orientation of methoxy groups at the T3–O33 position, which align parallel to the cylinder axis of the 8-MR channel, thereby facilitating more efficient CO insertion. These findings revealed the importance of precise aluminum siting within the MOR zeolite framework, as the presence of BAS in different channels and specific T-sites can significantly influence the catalytic performance of DME carbonylation. Therefore, developing advanced characterization methods to accurately identify the intrinsic acidity and acidic sites in different channels and T-sites is essential for optimizing the catalytic activity in MOR zeolites.

^{1}H ssNMR spectroscopies have been applied to elucidate the differences in the acidic sites of the 8-MR and 12-MR channels in MOR zeolites, especially in combination with deuterated probe molecules, *e.g.*, pyridine (C_5ND_5) and acetonitrile (CD_3CN). For BASs in H-MOR zeolites, conventional ^{1}H ssNMR methods yield an undistinguishable signal at 4.0 ppm for both the 8-MR and 12-MR channels. The method of combining ssNMR spectroscopy with probe molecules used by Yi and Zheng *et al.*[184,327,328] has been proven to be effective in resolving acidic characteristics such as type, intensity, distribution, and concentration. Pyridine, with a kinetic diameter of 5.4 Å, selectively accesses 12-MR channels while being excluded from 8-MR pores, making it a valuable probe for quantifying BAS in these distinct environments. After adsorbing C_5D_5N onto pre-dehydrated H-MOR using liquid N_2 freezing, the sample was heated to 473 K at the rate of 5 K min^{-1} and then evaluated for 10 min to remove excess physical adsorbed C_5D_5N. Subsequent ^{1}H MAS NMR spectra revealed that BAS signals in the 8-MR appeared in the high-field region (lower chemical shift, 4.2 ppm), whereas the signals arising from the interaction of C_5D_5N with BAS in the 12-MR were observed in the low-field region (higher chemical shift, 15 ppm).[78,79] Likewise, CD_3CN has been extensively employed to the acidity characterizations of MOR zeolite channels with unprecedented resolution of acidic properties in different pores.[329] The 10.5 ppm signal corresponded to the binding of BAS with CD_3CN in the 12-MR channels, while the 12.2 ppm signal was attributed to the binding of BAS with acetonitrile in the 8-MR side pockets (Fig. 19a). The stronger spatial confinement in the 8-MR enhances the strength of hydrogen bond between CD_3CN and BAS, resulting in a higher chemical shift. Furthermore, they performed 2D ^{1}H–^{1}H homonuclear DQ and SQ correlation NMR experiments to map the spatial networks for Brønsted acid pairs (BAPs) in different pore channels of the H-MOR zeolite, following adsorption of CD_3CN probe molecules. These findings highlight the utility of CD_3CN as a reliable and practical probe for differentiating BAS distribution and strength across distinct zeolite regions, which offers advantages over traditional methods due to its unique and unprecedented spectroscopic resolution and sensitivity, particularly in conjunction with advanced 2D homo-/heteronuclear correlation spectroscopy.

In MOR zeolites, aluminum atoms can occupy different T sites within the framework, leading to variations in acidity and catalytic behavior. Therefore, understanding and further controlling the location of framework Al are of critical importance. ^{27}Al MQMAS NMR spectroscopy enables to probe the spatial distribution of Al atoms in MOR zeolites.[330] This two-dimensional technique differentiates Al localization at distinct T sites in zeolites, with the F2 dimension capturing anisotropic chemical shifts and the F1 dimension representing isotropic shifts, thereby eliminating quadrupolar effects. However, its application to MOR zeolite is challenging due to the overlapping chemical shifts of Al at its four T sites, often yielding a single broad signal in ^{27}Al MAS NMR spectroscopy. In this work, MOR zeolites were treated *via* post-$SiCl_4$ treatment under

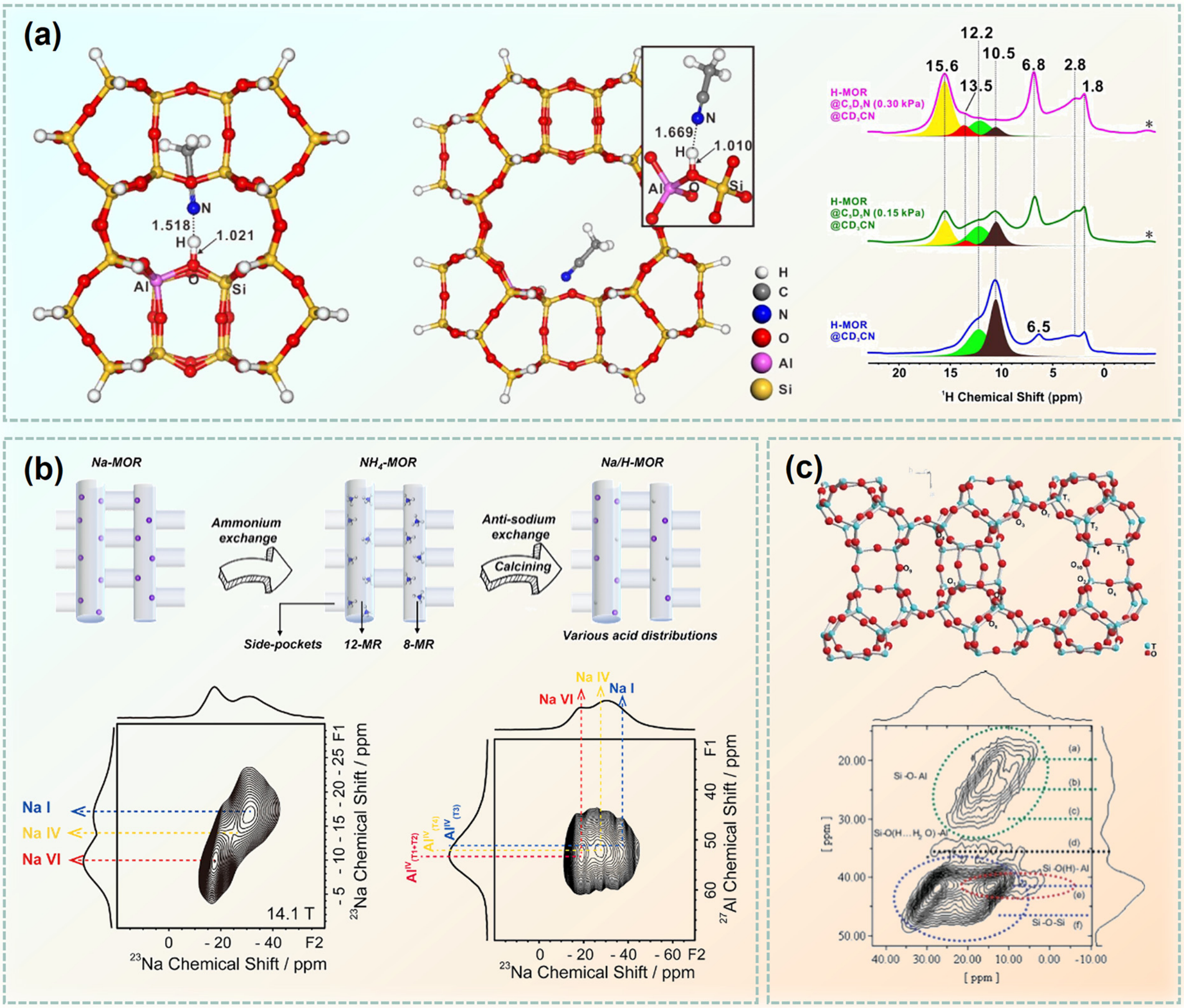

Fig. 19 SsNMR methods for distinguishing different sites in H-MOR. (a) ^{1}H MAS NMR by using probe molecules deuterated pyridine or deuterated acetonitrile. Reproduced with permission from ref. 329. Copyright 2020 American Chemical Society. (b) Two-dimensional ^{23}Na MQ MAS NMR and 2D ^{23}Na–^{27}Al D-HMQC MAS NMR spectrum of Na-MOR acquired at 14.1 T. Reproduced with permission from ref. 7. Copyright 2022 American Chemical Society. (c) Two-dimensional ^{17}O MQMAS NMR spectrum of ^{17}O-enriched H-MOR acquired at 19.6 T. Reproduced with permission from ref. 332. Copyright 2012 American Chemical Society.

low-pressure conditions, enabling directional relocation of framework Al to T3 sites. By systematically varying the treatment temperature, a series of MOR samples with distinct Al distributions across T sites were synthesized. Comparative analysis of these samples resolved the ^{27}Al NMR signals corresponding to T3 (56.2 ppm), T4 (57.3 ppm), T1 (58.4 ppm), and T2 (60.3 ppm) sites.

In addition, sodium ions (Na^+) serve as probes for identifying the locations of framework Al atoms due to their electrostatic interactions. Researchers systematically prepared a series of xNa/(100 − x) NH_4-MOR samples (x = 28, 39, 51, 75) through ion exchange of NH_4-MOR with sodium nitrate solutions of varying concentrations.[7] These precursors were subsequently deammoniated to yield xNa/(100 − x) H-MOR. High magnetic field ^{23}Na MAS NMR and ^{23}Na–^{27}Al D-HMQC spectroscopy successfully resolved distinct Na^+ signals corresponding to site-specific coordination environments within the xNa/(100 − x) H-MOR framework. ^{23}Na MAS NMR spectra identified three distinct Na^+ signals, corresponding to the Na VI site located in the 12-MR channels, the Na IV site in the 8-MR side pockets, and the Na I site in the 8-MR channels. ^{23}Na–^{27}Al D-HMQC NMR spectra further established spatial correlations between Na^+ and adjacent aluminum atoms: Na VI with T1 and T2, Na IV with T4, and Na I with T3, as illustrated in Fig. 19b.

MOR zeolites contain 10 framework oxygen sites (O1–O10). Martucci *et al.*[331] investigated deuterated mordenite *via* neutron diffraction under the assumption of equal protonation probabilities across oxygen sites, identifying four distinct BASs: one at O6 (8-MR side pocket entrance), one at O9 (8-MR channel center), and two at O5/O10 (protruding into the 12-MR main channel). Subsequently, Huo *et al.*[332] established a multimodal NMR strategy combining ^{1}H/^{17}O double-resonance experiments with variable CP contact times and ^{17}O MQMAS spectroscopy (Fig. 19c). This approach systematically resolved three types of BASs in H-MOR by correlating ^1H chemical environments with ^{17}O NMR parameters, ultimately linking site-specific acidity to structural descriptors through quantitative analysis of T–O–T bond angles derived from the ^{17}O MQMAS spectra.

The different structures required for MTO and DME carbonylation reactions are attributed to their differing reaction mechanisms and operating conditions. MTO processes occur at elevated temperatures (673–773 K), where the zeolite's pore size and shape selectivity significantly influence the formation of a diverse array of olefins and aromatics. In contrast, DME carbonylation operates at lower temperatures (423–573 K) and achieves high selectivity ($>99\%$) for MA through the activation of SMS. This selectivity is closely linked to the specific arrangement of BAS within the 8-MR channels in MOR zeolites, which facilitate Koch-carbonylation pathways. To enhance MA selectivity, strategies like directional move of Al from 12-MR to 8-MR channels through selective extraction of undesired framework Al in 12-MR have been employed to optimize BAS density within the 8-MR channels. Selective enrichment of BAS in 8-MR channels has been shown to significantly increase catalytic activity, while minimizing undesired reactions in the 12-MR channels. Post-synthesis treatments that reduce framework defects also contribute to improved performance by mitigating coke formation and enhancing catalyst stability.

Advancements in high-resolution characterization techniques such as NMR probe molecule techniques, ^{27}Al MQMAS NMR spectroscopy, ^{23}Na MAS NMR spectroscopy and ^{17}O MQMAS spectroscopy are crucial for establishing quantitative correlations between the BAS activity and the zeolite structure at the atomic scale. Combining these characterization methods with targeted synthesis and modification strategies enables mapping of aluminum distribution and BAS locations, providing deeper insights into structure–activity relationships.

4.3. Effect of water in DME carbonylation reactions

Using methanol as the feedstock for carbonylation over H-MOR zeolites resulted in significant DME formation, with product selectivity of 65.4% for acetic acid and 30.8% for MA (the DME yield was separated from the yield of the other compounds).[279,280] This contrasts sharply with the 99% MA selectivity observed when DME is used as the feedstock. The lower MA selectivity with methanol arises because water released during methoxy group formation competitively adsorbs at CO-binding sites and/or causes parallel methanol dehydration reactions.[279] Furthermore, even when DME is employed as the feedstock, methanol generated during methoxy group formation can undergo subsequent reactions at BAS, still producing trace amounts of water.[333] Therefore, investigating the impact of water on DME carbonylation remains essential. Moreover, since the zeolite catalyst used is MOR, which has a low Si/Al ratio, its hydrothermal stability during industrial catalyst preparation is a critical consideration.

4.3.1. Effect of water on MOR. The presence of water significantly influences the structural and acidic properties of MOR zeolites, thereby affecting the catalytic performance in DME carbonylation. Water induces reversible changes in the coordination state of aluminum within the MOR framework. Van Bokhoven *et al.*[183] systematically investigated the structural evolution of aluminum species in H-MOR zeolites and the correlation with acid regulation, providing a detailed interpretation of the structure and coordination of Lewis acidic Al sites.[183] They established the reversible transformation mechanism between Al(VI) and Al(IV) in the zeolite framework. Under high-temperature calcination or humid conditions, some tetrahedral Al(IV) species hydrolysed and interacted with water or hydroxyl groups, converting into penta- and octahedrally coordinated aluminum species (Al(VI)). This conversion can be demonstrated by ^{27}Al MAS NMR and ^{27}Al MQMAS NMR spectra. Specifically, increasing the calcination temperature of MOR zeolites enhanced the signal intensity of octahedrally coordinated aluminum (0 ppm) in ^{27}Al MAS NMR spectra. Concurrently, variations observed in the ^{27}Al MQMAS NMR spectra of the sample series further confirmed the aluminum coordination changes. Unlike the traditionally assumed irreversible formation of EFAL species, these Lewis-acidic Al(VI) species remain chemically bonded within the zeolite framework. To confirm this reversible behavior, ammonium exchange and rehydration experiments were conducted, indicating that Al(VI) species reverted to tetrahedral Al(IV) upon hydration, thereby regenerating BASs (Fig. 20a). This reversibility was confirmed by ^{27}Al MAS NMR spectra: as hydration progressed, the Al(VI) signal at 0 ppm diminished and eventually vanished, while the Al(IV) signal at 56 ppm restored. These findings demonstrate the dynamic equilibrium between LAS and BAS, challenging the conventional view of irreversible EFAL formation.[334] Subsequent studies have revealed that cations, such as Na^+, play a crucial role in stabilizing framework aluminum species by reducing their affinity for water molecules.[335] Additionally, cation exchange can regulate the acidity of H-MOR zeolites, making it one of the key modification strategies.

High-temperature selective dealumination effectively regulates acidity in MOR zeolites, optimizing acid site distribution, suppressing side reactions, and enhancing catalytic performance.[336] Under high-temperature steam treatment, framework Al species in the 12-MR channels is selectively removed, whereas those in the 8-MR channels remain largely intact. It was evidenced by three key spectroscopic observations: (1) the Si/Al ratio determined from ^{29}Si MAS NMR spectra increases from 8.5 to 15.5, (2) ^{27}Al MAS NMR spectra show reduced relative intensities of framework-coordinated Al (54 ppm) and octahedrally coordinated extra-framework Al (0 ppm), and (3) ^1H MAS NMR spectra reveal decreased BAS concentration quantified through the 3.8 ppm signal. This treatment decreases both the number and strength of BASs in the 12-MR channels while preserving stable acid sites in the 8-MR channels. Selective removal of acid sites from the 12-MR channels while preserving those in the 8-MR channels optimizes acid site distribution in MOR zeolites, enhancing their suitability for target reactions such as DME carbonylation. The suppression of side reactions improves reaction selectivity and

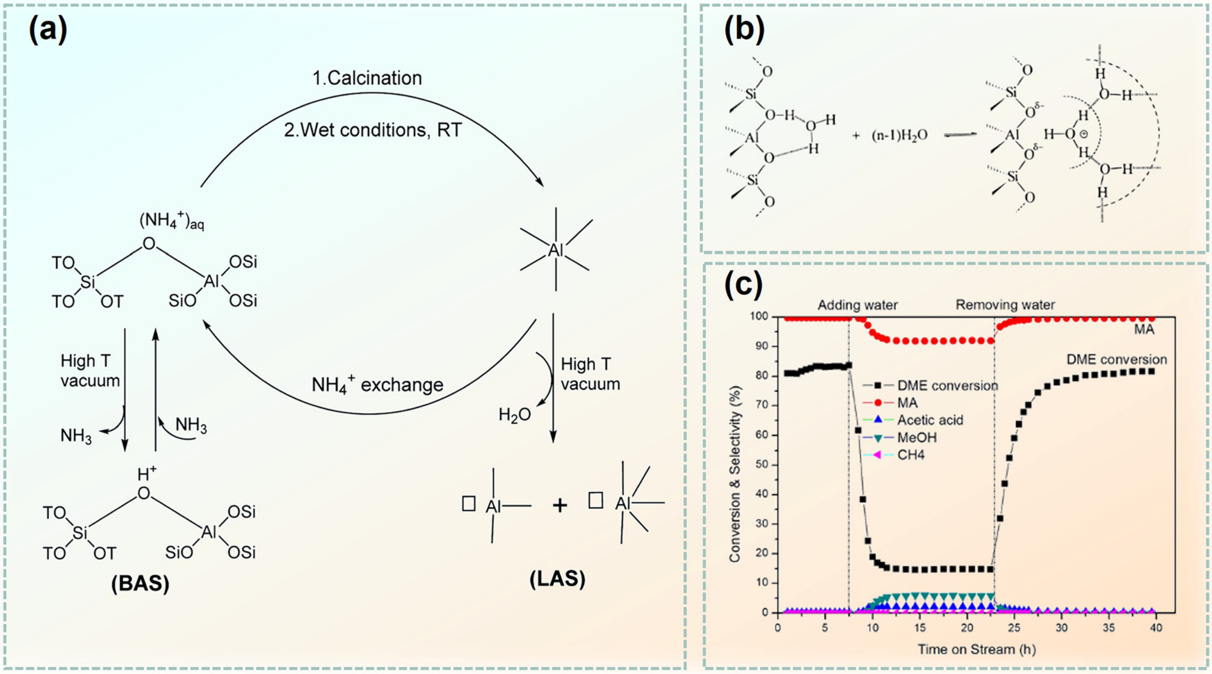

Fig. 20 Effect of water in DME carbonylation reactions. (a) Reversible tetrahedral–octahedral coordination exhibited by framework-associated aluminum and its impact on Brønsted and Lewis acidity. Reproduced with permission from ref. 334. Copyright 2021 Royal Society of Chemistry. (b) Water forms clusters. Reproduced with permission from ref. 337. Copyright 1996 American Chemical Society. (c) Influence of water on the DME carbonylation catalytic performance of 1TMA-H-MOR. TEA-H-MOR was prepared by exchanging with tetraethylammonium (TEA^+) chloride. The exchanged samples were named as *x*TMA-H-MOR (*x* = 1, 2 and 3, the exchange times). Reproduced with permission from ref. 338. Copyright 2020 Royal Society of Chemistry.

enhances target product yield. Furthermore, selective dealumination markedly enhances catalyst stability.

4.3.2. Influence of water on the DME carbonylation reaction pathway. The influence of water on DME carbonylation is a crucial factor in industrial process design. Experimental studies indicated that introducing water into the DME and CO mixture significantly reduces the MA formation rate.[285] The observed water inhibition mechanism cannot be attributed to either H_2O–DME competitive adsorption at BAS or the displacement of DME-derived intermediates, given the persistent zero-order kinetics with respect to DME pressure under hydrous conditions. Rather, H_2O selectively competes with CO for adsorption at LAS.[279] Under steady-state conditions, both methanol and DME form similar SMS on BAS; however, methanol exhibits significantly lower carbonylation activity. Theoretical calculations indicate that the activation energy for the reaction of water with SMS (< 80 kJ mol^{-1}) is lower than that for CO insertion (≥ 100 kJ mol^{-1} at the T3–O33 site).[34] Additionally, water molecules tend to form clusters (Fig. 20b) that obstruct the 8-MR side pockets of MOR zeolites, thereby inhibiting DME carbonylation at low temperatures.[333,337] Liu *et al.*[338] demonstrated that water vapor addition rapidly decreases both the DME conversion rate and MA selectivity while slightly increasing methanol and acetic acid selectivity. Interestingly, these parameters revert to their original levels upon cessation of water vapor, as shown in Fig. 20c. These observations suggest that water suppresses the formation of acetyl intermediates, thereby lowering both reaction rates and selectivity. Consequently, industrial DME carbonylation processes typically incorporate drying units to remove water from the feedstock and mitigate its adverse effects. Although the inhibitory effect of water on the reaction rate is widely accepted, the mechanism of water in DME carbonylation needs more atomic-level studies.

In summary, water exerts two major effects on the DME carbonylation reaction. First, water alters the aluminum species in the zeolite framework, leading to dealumination. Moreover, water suppresses the formation of acetyl intermediates, thereby reducing both the reaction rate and selectivity. Therefore, a key research focus is to prevent dealumination during the preparation of H-MOR zeolites or selectively remove aluminum species in 12-MR. Additionally, minimizing the water content of reactants and ensuring the rapid removal of water produced in the process may provide a promising strategy. This could potentially be achieved through the use of membrane reactors or hydrophobic materials.[339]

4.4. Modification of MOR zeolites in DME carbonylation

Previous mechanistic investigations have demonstrated that DME carbonylation over H-MOR zeolites achieves high conversion and selectivity. It suffers from rapid deactivation due to poor stability—a key limitation hindering its industrial application.[29] This instability primarily originates from carbon deposition within the 12-MR channels, where coke formation from DME induces swift activity loss and complete catalyst deactivation within brief operational periods.[31] To address these challenges, various strategies have been developed, including synthesis optimization,[340–351] acidity modulation,[330,336,352–358] alkaline molecular modification,[282,338] metal modification,[305–313] pore engineering,[316–319] and new zeolite exploration.[320–325] Notably, metal modification, pore engineering, and the exploration of new zeolites have been discussed in Section 4.1 and will not be reiterated here. The remaining modification strategies primarily function through directed regulation of aluminum distribution and selective elimination or poisoning of BAS within the 12-MR pores of H-MOR. SsNMR spectroscopy has proven to be a powerful tool in characterizing these modifications. Techniques like ^{1}H MAS NMR can quantify BAS density, while ^{27}Al and ^{29}Si MAS NMR can assess dealumination and Si/Al ratios, respectively. The use of probe molecules, such as pyridine and CD_3CN, in conjunction with ssNMR, allows for the differentiation of BAS in the 8-MR and 12-MR channels, providing insights into their spatial distribution and interactions. This detailed characterization is essential for understanding the structure–activity relationship in zeolite catalysts and for guiding the development of more efficient and stable catalysts for industrial applications.

4.4.1. Directed regulation of aluminum distribution. During MOR synthesis, controlling the hydrothermal synthesis time,[351] aluminum concentration in the precursor solution,[349,350] synthesis conditions,[343–348] and the type of structure directing agents (SDAs)[340–342] enables the precise regulation of aluminum distribution in MOR. Among these methods, the introduction of SDAs during hydrothermal synthesis represents an effective strategy for controlling aluminum distribution.[340] The tunable size and structure of SDAs enable precise localization within zeolite channels, thereby regulating host–guest interactions and ultimately governing Al siting. For instance, tetraethylammonium hydroxide (TEAOH) employed in an amine vapor-assisted dry-gel conversion method directed 75% of framework Al into 8-MR pores.[342] This is evidenced by ^{1}H MAS NMR spectra of pyridine adsorption on MOR samples before and after TEAOH addition: the BAS concentration in 8-MR side pockets increased from 0.39 to 0.76 mmol g^{-1}, while the BAS concentration in 12-MR channels decreased from 0.39 to 0.26 mmol g^{-1}. These targeted Al distributions directly correlate with catalytic performance—enrichment of Al in 8-MR pores significantly enhances the conversion of DME and the selectivity of MA during DME carbonylation.

Additionally, post treatments can be applied to adjust aluminum distribution in MOR. High-temperature dealumination is a method that has already been discussed in Section 4.3.1.[336,358] Acid treatment is a common post treatment method for removing framework aluminum; however, it also extracts Al from T3 sites, thereby enhancing selectivity at the expense of reduced conversion rates.[353–357] Liu *et al.*[330] proposed a strategy to preferentially relocate framework Al atoms into desired T3 sites in MOR *via* low-pressure $SiCl_4$ treatment (LPST). Due to molecular size constraints, $SiCl_4$ selectively accesses the 12-MR channels, replacing framework Al with Si and extracting $AlCl_3$. The $AlCl_3$ migrates into 8-MR channels and reacts with silanol defects at T sites, enabling Al reinsertion into the framework (Fig. 21a). These conclusions were confirmed by ^{27}Al MAS and MQMAS NMR spectra. Comparative analysis of ^{27}Al MAS NMR spectra from samples treated at varying LPST temperatures reveals similar peak shapes but a distinct upfield shift of tetrahedral Al signals in treated samples, indicating altered Al distribution across T sites. High-field (18.8 T) MQMAS spectra resolve multiple chemical shifts corresponding to distinct Al environments. The 45–65 ppm region in the ^{27}Al MAS NMR spectra of all MOR samples deconvolutes into four components at 56.2, 57.3, 58.4, and 60.3 ppm, assigned to Al occupancy at MOR's four non-equivalent T sites (Fig. 21b). Quantitative fitting of ^{27}Al MAS NMR spectra across samples reveals the Al distribution in each T site, demonstrating the tunability of aluminum siting within the zeolite framework.

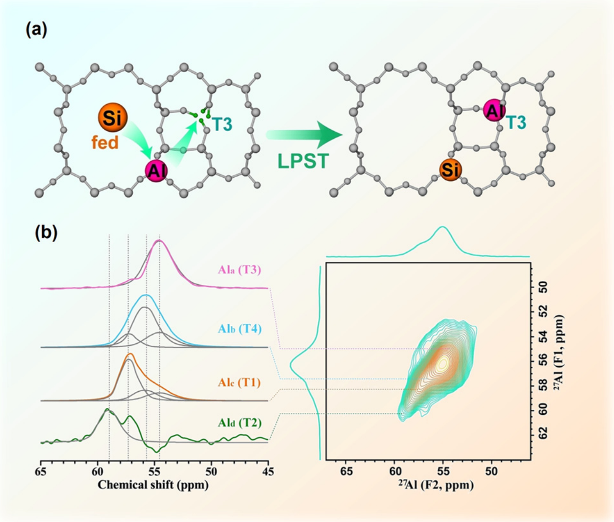

Fig. 21 Using ssNMR techniques to elucidate the mechanism of LPST. (a) Schematic of the LPST mechanism. (b) ^{27}Al MQ MAS NMR spectrum of the MOR-873 K sample at 18.8 T, and the slices extracted from F1 dimension. Reproduced with permission from ref. 330. Copyright 2022 John Wiley and Sons.

4.4.2. Elimination/poisoning of BAS within the 12-MR. Based on the functions of acid sites in different pores of H-MOR during DME carbonylation, several strategies have been proposed to eliminate or poison the acid sites in the 12-MR pores. Pyridine, with a molecular size of approximately 5 Å, has attracted considerable attention due to its optimal size and basicity, demonstrating exceptional efficacy in enhancing catalyst performance. Shen *et al.*[282] mitigated the rapid deactivation of H-MOR zeolite catalysts in DME carbonylation through pre-adsorbing pyridine. This treatment selectively passivated BAS in the 12-MR channels to suppress coke formation and preserved the active sites in the 8-MR channels. Under optimized conditions (473 K), pyridine-modified H-MOR exhibited >99% MA selectivity and remained stable for 48 hours (Fig. 22a). Li *et al.*[359] investigated the effects of pyridine adsorption duration and desorption temperature on BAS peak intensities in MOR using *in situ* DRIFTS and ^{1}H MAS NMR spectroscopy. Catalytic performance evaluations further confirmed that these treatment conditions influenced the activity of pyridine-modified H-MOR. DFT calculations revealed that this modulation arises from proton interactions between pyridine and O2 sites (located at the shared wall of the 12-MR main channel and 8-MR side pocket), which selectively alter BAS accessibility and reactivity. In subsequent studies, researchers observed through FT-IR spectra that the bands associated with Brønsted hydroxyls are completely eroded upon pyridine adsorption at room temperature, demonstrating that pyridine molecules not only selectively adsorb within the 12-MR channels but may also penetrate into the 8-MR side pockets. They hypothesized that this phenomenon likely arises from defect sites in the MOR framework, which enlarge the effective pore window size of the side pockets.[360] Recent work by Liu *et al.*[361] demonstrates that pyridine adsorption effectively converts octahedral Al species into tetrahedral coordination, enhancing catalytic performance by increasing the reactive framework Al content. Comparative ^{27}Al MAS NMR of MOR samples before/after pyridine pre-adsorption shows the disappearance of the 0 ppm octahedral Al signal without altering Si/Al ratios, confirming pyridine-induced framework Al reversion (Fig. 22b). ^{29}Si MAS NMR analysis of H-MOR reveals a 12% signal loss at −106 ppm (Si(1Al)(OSi)$_3$) in NH$_4$-MOR, which is fully restored post-pyridine treatment, verifying framework Al recovery. Pyridine pre-adsorption substantially enhanced catalytic performance, increasing the DME conversion rate by a factor of four and prolonging the catalyst lifetime to 120 hours.

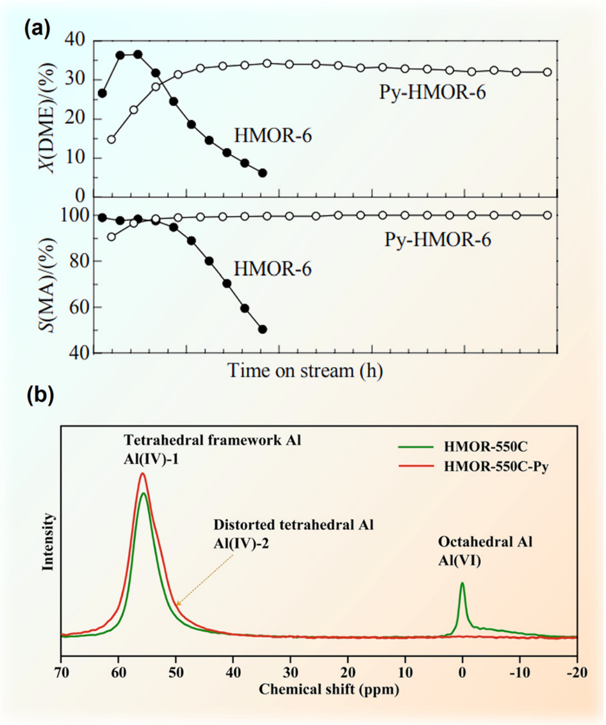

Fig. 22 Effects of pyridine modification on MOR. (a) Conversion of DME and selectivity for MA during DME carbonylation over HMOR-6 and Py-HMOR-6 catalysts. Reaction conditions: 473 K, 5% DME-50% CO-2.5% N$_2$-42.5% He, 1250 ml (g h)$^{-1}$, 1.0 MPa. Reproduced with permission from ref. 282. Copyright 2010 Elsevier. (b) Conversion of extra-framework aluminum into framework aluminum. Reproduced with permission from ref. 361. Copyright 2022 John Wiley and Sons.

Pyridine-MOR can effectively suppress hard coke formation and mitigate catalyst deactivation. However, as the reaction proceeds, the adsorbed pyridine gradually desorbs, failing to persistently shield BAS in the 12-MR channels, leading to continued deactivation.[336] Consequently, researchers have explored alternative reagents to eliminate/poison BAS within the 12-MR. Liu *et al.*[338] utilized tetramethylammonium chloride (TMACl) to selectively exchange counterions in different MOR channels, effectively reducing hydrocarbon formation and hard coke deposition. This strategy enabled stable catalyst operation for 210 hours while maintaining high MA selectivity. Due to steric hindrance, TMA$^+$ ions exclusively access the 12-MR channels, where counterion exchange reduces BAS density in these pores. FT-IR analysis with pyridine probing confirmed inability of TMA$^+$ to access 8-MR counterions: H-MOR exhibited dual Brønsted acid bands (3608 cm^{-1} in 12-MR, 3589 cm^{-1} in 8-MR), where pyridine eliminated the 3608 cm^{-1} peak but retained 3589 cm^{-1}. A facile approach was proposed to purposefully tailor acid site distribution *via* selective silylation using trimethylchlorosilane (TMCS), which selectively covers most undesired Brønsted acid sites in 12-MR channels, leaving approximately 80% of the remaining acid sites in the 8-MR environments of MOR zeolites.[352] ^{29}Si CP NMR spectra of TMCS-treated MOR samples revealed significant reductions in the intensities of Q^3 (Si(OH)(OSi)$_3$) and Q^2 (Si(OH)$_2$(OSi)$_2$) resonance signals, indicating silanol group bonding with TMCS during silylation. Owing to molecular size constraints (TMCS: 6.9 Å), TMCS exclusively accesses 12-MR channels, where its chloro groups hydrolyze to replace Brønsted H$^+$ atoms.

The application of advanced ssNMR spectroscopy has significantly enhanced our understanding of the locations of distinct acid sites and aluminum distribution within MOR zeolites, which is crucial for optimizing their catalytic performance in DME carbonylation. However, challenges persist in the precise regulation of aluminum distribution to enhance the density of BAS in the 8-MR channels while minimizing acidity in the 12-MR channels. Traditional post-synthesis modification methods such as selective dealumination using acidic or basic treatments have been employed to reduce 12-MR acidity. However, these approaches often struggle to fully remove aluminum sites from the 12-MR channels without affecting the 8-MR sites. Moreover, the elimination or poisoning of BAS in the 12-MR channels can negatively affect their role as diffusion pathways, potentially hindering overall catalytic performance. A viable strategy to overcome the limitations is identifying suitable SDAs that inhibit the formation of Al sites in 12-MR channels while maximizing the Al population in 8-MR channels. In addition, the synergistic effect of combining multiple modification strategies may provide a better solution to achieve this goal. Additionally, combining theoretical calculations with ssNMR spectroscopy is proving to be a powerful tool for predicting and verifying aluminum distributions within zeolites,[362–364] providing a more comprehensive understanding of the factors governing aluminum location, facilitating the design of more effective MOR catalysts.

5. Conclusion and perspectives

Over the past decade, zeolite-catalyzed methanol conversion processes have garnered significant attention as alternatives to traditional fossil feedstocks for olefin and ethanol production. Technological advancements have led to the successful operation of several industrial plants, demonstrating the commercial viability of MTO and MTE technology. Concurrently, the industrialization of these processes has spurred continuous progress in fundamental research. In this review, we presented a critical analysis of the relationship between foundational studies and industrial applications in zeolite-catalyzed methanol conversion, with a focus on MTO and DME carbonylation.

Advanced ssNMR spectroscopies have provided profound information into reaction mechanisms and catalyst structure–activity relationships, thereby bridging the gap between fundamental and applied research. In the MTO reaction, *in situ* ssNMR plays a critical role in the analysis of reactant adsorption, intermediate identification, and monitoring of dynamic reaction processes under reaction conditions. Notably, during the induction period, *in situ* spectroscopic evidence of the initial C–C bond formation represents a breakthrough of the past decade. Additionally, it was discovered that formaldehyde, produced during the induction phase through LAS-mediated reactions, facilitates the formation of the initial C–C bond. However, formaldehyde also accelerates the deactivation of the catalyst; therefore, industrial feedstocks should avoid containing formaldehyde impurities. In the high-efficiency stage, active HCP species observed by ssNMR contribute to the construction of a complex reaction network that governs product selectivity. These mechanistic achievements have been reflected in industrial practice. For example, a pre-coking strategy involving the pre-filling of CHA cages with specific PAHs has been employed to shorten induction periods and improve alkene selectivity. Additionally, ssNMR spectroscopy has provided detailed insights into the structural evolution of catalysts and the critical intermolecular interactions that are essential for optimizing catalyst regeneration processes. In parallel, the utilization of ssNMR spectroscopy, particularly 2D ssNMR spectroscopy, has enabled precise characterization of BAS distributions, framework aluminum locations, and the dynamic behavior of active sites of MOR zeolites in DME carbonylation. The synergistic roles of 8-MR and 12-MR channels in MOR zeolites underpin the successful industrial application. Based on these comprehensive understandings, pyridine pre-adsorption effectively preserves active BASs in the 8-MR channels while shielding deactivating sites in the 12-MR channels, demonstrating high selectivity for MA and enhanced stability in DME carbonylation. These approaches underscore the importance of mechanistic studies in driving innovations in catalyst design and process optimization, ultimately leading to more efficient industrial applications in methanol conversion.

The MTO and DME carbonylation processes are interconnected reactions within C1 chemistry, both involving the transformation of simple carbon compounds into valuable hydrocarbons. A key mechanistic link between these processes is the formation of C–C bonds, which is crucial for hydrocarbon production. In DME carbonylation, CO inserts into the C–O bond of SMS, leading to acetyl intermediates. This step significantly influences reaction pathways and product selectivity. Understanding this mechanism has also provided insights into the initial C–C bond formation in the MTO process, enriching comprehension of methanol conversion mechanisms. An in-depth study on the MTO reaction might act as a basis for more comprehensive investigation of DME carbonylation process. The unique structures of zeolite catalysts play a pivotal role in these processes by affecting the adsorption, activation, and reaction pathways of methanol and its derivatives. Interactions between the zeolite framework and intermediates, products, or H_2O significantly alter the local microenvironment of the catalyst, thereby regulating reaction pathways and catalytic cycles. The comprehensive understandings on mechanism of methanol conversion can offer guidance for other methanol-involved catalytic processes, such as conversion of syngas or CO_2 to methanol followed by the MTO reaction to produce sustainable chemicals using a bifunctional catalytic system.[365–370]

Despite these advancements, correlating *in situ* characterization of active sites with the atomic-level mechanisms remains a significant challenge due to the dynamic evolving nature of active sites and intermediate species during catalytic reactions. Addressing this challenge necessitates the advancement of *in situ* techniques capable of modulating operating conditions, particularly under high-temperature, high-pressure, and continuous-flow environments. Furthermore, the mechanisms through which zeolite structure and acidity govern methanol conversion and product selectivity remain a key area of investigation. Elucidating these molecular mechanisms is pivotal for designing high-performance catalysts to enhance the catalytic efficiency, advancing industrial applications, and enriching the catalytic theory in the field of zeolites. Future research should focus on coupling reaction networks with diffusion processes and developing ssNMR techniques with enhanced spatiotemporal resolution to monitor dynamic changes of active sites during reactions. Combining ssNMR with other *operando* techniques and molecular dynamic simulations such as neutron scattering[371] and synchrotron radiation technique[372] is expected to simultaneously study the diffusion mechanism and reaction mechanism in catalytic reactions. Notably, machine learning integration could revolutionize conventional spectroscopic analysis,[373–377] enabling refinement of mechanistic models and optimization of industrial zeolite-catalyzed processes.

The critical challenge in bridging fundamental studies with industrial MTO/DMTO technologies resides in validating the relevance of laboratory-observed phenomena to industrial reactor environments. Currently, it remains difficult to replicate industrial-scale conditions during *in situ* NMR or other *operando* techniques (particularly high-temperature conditions in fluidized-bed reactors). Advancing high-resolution *in situ* methods that can operate under such demanding conditions is both essential and technically challenging. Given the complexity and dynamic nature of MTO reactions, several key issues remain unresolved. These include elucidating the critical role of water (an unavoidable component in MTO systems), developing comprehensive reaction-diffusion network models, and optimizing regeneration strategies to effectively regulate catalytic cycles. We hope that future advancements in characterization technology will help address these challenges. In conclusion, fundamental research provides theoretical references for industrial processes, while practical applications drive the innovation of fundamental research. Fundamental research needs to consult the results of industrial applications to continuously optimize the theoretical system developed in laboratories, thereby promoting technological progress and industrial upgrading.

Author contributions

Jing Niu: investigation, formal analysis, visualization, and writing. Xinzhi Ding: investigation, visualization, original draft, and writing. Shutao Xu: investigation, validation, writing, supervision, and funding acquisition. Yingxu Wei: writing review, validation, and supervision. Zhongmin Liu: supervision, validation, review, and funding acquisition. The manuscript was written and revised through contributions from all authors. All authors have approved the final version of the manuscript.

Data availability

No primary research results, software or code have been included and no new data were generated or analysed as part of this review.

Conflicts of interest

There are no conflicts to declare.

Acknowledgements

This work was financially supported by the National Natural Science Foundation of China (22241801; 22288101; 22022202; 22032005; 21991090; 21991092; and 21991093); the National Key Research and Development Program of China (No. 2022YFE0116000); the Dalian Outstanding Young Scientist Foundation (2021RJ01), and the Liaoning International Joint Laboratory Project (2024JH2/102100005).

References

1 Y. Li and J. Yu, *Nat. Rev. Mater.*, 2021, **6**, 1156–1174.
2 Y. Wang, C. Tong, Q. Liu, R. Han and C. Liu, *Chem. Rev.*, 2023, **123**, 11664–11721.
3 S. H. van Vreeswijk and B. M. Weckhuysen, *Natl. Sci. Rev.*, 2022, **9**, nwac047.
4 G. Tian, X. Liang, H. Xiong, C. Zhang and F. Wei, *EES Catal.*, 2023, **1**, 677–686.
5 H. Cruchade, I. C. Medeiros-Costa, N. Nesterenko, J.-P. Gilson, L. Pinard, A. Beuque and S. Mintova, *ACS Catal.*, 2022, **12**, 14533–14558.
6 P. del Campo, C. Martínez and A. Corma, *Chem. Soc. Rev.*, 2021, **50**, 8511–8595.
7 B. Fan, W. Zhang, P. Gao, G. Hou, R. Liu, S. Xu, Y. Wei and Z. Liu, *J. Phys. Chem. Lett.*, 2022, **13**, 5186–5194.
8 S. A. Chernyak, M. Corda, J.-P. Dath, V. V. Ordomsky and A. Y. Khodakov, *Chem. Soc. Rev.*, 2022, **51**, 7994–8044.
9 W. Zhou, K. Cheng, J. Kang, C. Zhou, V. Subramanian, Q. Zhang and Y. Wang, *Chem. Soc. Rev.*, 2019, **48**, 3193–3228.
10 C. Tu, X. Nie and J. G. Chen, *ACS Catal.*, 2021, **11**, 3384–3401.
11 S. S. Tabibian and M. Sharifzadeh, *Renewable Sustainable Energy Rev.*, 2023, **179**, 113281.
12 Q. Zhang, J. Yu and A. Corma, *Adv. Mater.*, 2020, **32**, 2002927.
13 P. Zhai, Y. Li, M. Wang, J. Liu, Z. Cao, J. Zhang, Y. Xu, X. Liu, Y.-W. Li, Q. Zhu, D. Xiao, X.-D. Wen and D. Ma, *Chem*, 2021, **7**, 3027–3051.
14 S. Xie, W. Ma, X. Wu, H. Zhang, Q. Zhang, Y. Wang and Y. Wang, *Energy Environ. Sci.*, 2021, **14**, 37–89.
15 G. A. Olah, A. Goeppert and G. K. S. Prakash, *Beyond Oil and Gas: The Methanol Economy*, Wiley-VCH, Weinheim, 2006.
16 C. Filosa, X. Gong, A. Bavykina, A. D. Chowdhury, J. M. R. Gallo and J. Gascon, *Acc. Chem. Res.*, 2023, **56**, 3492–3503.
17 U. Olsbye, S. Svelle, M. Bjorgen, P. Beato, T. V. Janssens, F. Joensen, S. Bordiga and K. P. Lillerud, *Angew. Chem., Int. Ed.*, 2012, **51**, 5810–5831.
18 S. Ilias and A. Bhan, *ACS Catal.*, 2013, **3**, 18–31.
19 I. Yarulina, A. D. Chowdhury, F. Meirer, B. M. Weckhuysen and J. Gascon, *Nat. Catal.*, 2018, **1**, 398–411.
20 P. Tian, Y. Wei, M. Ye and Z. Liu, *ACS Catal.*, 2015, **5**, 1922–1938.
21 S. Xu, Y. Zhi, J. Han, W. Zhang, X. Wu, T. Sun, Y. Wei and Z. Liu, *Adv. Catal.*, 2017, **61**, 37–122.
22 M. Yang, D. Fan, Y. Wei, P. Tian and Z. Liu, *Adv. Mater.*, 2019, **31**, 1902181.
23 S. Wang, Z. Qin, M. Dong, J. Wang and W. Fan, *Chem. Catal.*, 2022, **2**, 1657–1685.
24 W. Zhang, Y. Wei and Z. Liu, in *The Chemical Transformations of C1 Compounds*, ed. X. Wu, B. Han, K. Ding and Z. Liu, Wiley-VCH GmbH, 2022, pp. 71–126.
25 D. A. Ruddy, J. E. Hensley, C. P. Nash, E. C. D. Tan, E. Christensen, C. A. Farberow, F. G. Baddour, K. M. Van Allsburg and J. A. Schaidle, *Nat. Catal.*, 2019, **2**, 632–640.
26 T. Li, T. Shoinkhorova, J. Gascon and J. Ruiz-Martínez, *ACS Catal.*, 2021, **11**, 7780–7819.
27 T. Shoinkhorova, T. Cordero-Lanzac, A. Ramirez, S.-H. Chung, A. Dokania, J. Ruiz-Martinez and J. Gascon, *ACS Catal.*, 2021, **11**, 3602–3613.

28 W. Chen, Z. Liu, X. Yi and A. Zheng, *Acc. Chem. Res.*, 2024, **57**, 2804–2815.

29 G. Liu, G. Yang, X. Peng, J. Wu and N. Tsubaki, *Chem. Soc. Rev.*, 2022, **51**, 5606–5659.

30 M. A. Kipnis and E. A. Volnina, *Kinet. Catal.*, 2022, **63**, 129–140.

31 E. Zhan, Z. Xiong and W. Shen, *J. Energy Chem.*, 2019, **36**, 51–63.

32 X. Wu, Y. Wei and Z. Liu, *Acc. Chem. Res.*, 2023, **56**, 2001–2014.

33 H. Zhou, X. Gong, E. Abou-Hamad, Y. Ye, X. Zhang, P. Ma, J. Gascon and A. D. Chowdhury, *Angew. Chem., Int. Ed.*, 2024, **63**, e202318250.

34 M. Boronat, C. Martínez-Sánchez, D. Law and A. Corma, *J. Am. Chem. Soc.*, 2008, **130**, 16316–16323.

35 U. Olsbye, S. Svelle, K. P. Lillerud, Z. H. Wei, Y. Y. Chen, J. F. Li, J. G. Wang and W. B. Fan, *Chem. Soc. Rev.*, 2015, **44**, 7155–7176.

36 X. Wu, Z. Zhang, Z. Pan, X. Zhou, A. Bodi and P. Hemberger, *Angew. Chem., Int. Ed.*, 2022, **61**, e202207777.

37 Y. Ye, E. Abou-Hamad, X. Gong, T. B. Shoinkhorova, A. Dokania, J. Gascon and A. D. Chowdhury, *Angew. Chem., Int. Ed.*, 2023, **62**, e202303124.

38 C. Chizallet, C. Bouchy, K. Larmier and G. Pirngruber, *Chem. Rev.*, 2023, **123**, 6107–6196.

39 P. Gao, Y. Ji and G. Hou, *J. Am. Chem. Soc.*, 2025, **147**, 2919–2937.

40 W. Wang, J. Xu and F. Deng, *Natl. Sci. Rev.*, 2022, **9**, nwac155.

41 G. Qi, Q. Wang, J. Xu and F. Deng, *Chem. Soc. Rev.*, 2021, **50**, 8382–8399.

42 M. Ye, P. Tian and Z. M. Liu, *Engineering*, 2021, **7**, 17–21.

43 Q. Sun, Z. Xie and J. Yu, *Natl. Sci. Rev.*, 2018, **5**, 542–558.

44 A. Hwang and A. Bhan, *Acc. Chem. Res.*, 2019, **52**, 2647–2656.

45 R. Liu, X. Shao, C. Wang, W. Dai and N. Guan, *Chin. J. Catal.*, 2023, **47**, 67–92.

46 N. Hadi and A. Farzi, *Chem. Eng. Commun.*, 2022, **209**, 1664–1710.

47 J. Zhong, J. Han, Y. Wei and Z. Liu, *J. Catal.*, 2021, **396**, 23–31.

48 T. Cordero-Lanzac, A. G. Gayubo, A. T. Aguayo and J. Bilbao, *Chem. Eng. J.*, 2024, **494**, 152906.

49 S. Li, O. Lafon, W. Wang, Q. Wang, X. Wang, Y. Li, J. Xu and F. Deng, *Adv. Mater.*, 2020, **32**, 2002879.

50 M. Zheng, Y. Chu, Q. Wang, Y. Wang, J. Xu and F. Deng, *Prog. Nucl. Magn. Reson. Spectrosc.*, 2024, **140–141**, 1–41.

51 I. I. Ivanova and E. P. Andriako, *Microporous Mesoporous Mater.*, 2023, **358**, 112363.

52 I. I. Ivanova and Y. G. Kolyagin, *Chem. Soc. Rev.*, 2010, **39**, 5018–5050.

53 Y. Nishiyama, G. Hou, V. Agarwal, Y. Su and A. Ramamoorthy, *Chem. Rev.*, 2023, **123**, 918–988.

54 A. Marchetti, J. Chen, Z. Pang, S. Li, D. Ling, F. Deng and X. Kong, *Adv. Mater.*, 2017, **29**, 1605895.

55 S. Lin, H. Li, P. Tian, Y. Wei, M. Ye and Z. Liu, *J. Am. Chem. Soc.*, 2025, **147**, 11585–11607.

56 W. Zhang, S. Xu, X. Han and X. Bao, *Chem. Soc. Rev.*, 2012, **41**, 192–210.

57 J. Xu, Q. Wang and F. Deng, *Acc. Chem. Res.*, 2019, **52**, 2179–2189.

58 T. Blasco, *Chem. Soc. Rev.*, 2010, **39**, 4685–4702.

59 J. Niu, S. Xu, Y. Wei and Z. Liu, *Sci. China: Chem.*, 2024, **68**, 134–151.

60 T. A. Carpenter, J. Klinowski, D. Tennakoon, C. J. Smith and D. C. Edwards, *J. Magn. Reson.*, 1986, **68**, 561–563.

61 T. Xu and J. F. Haw, *Top. Catal.*, 1997, **4**, 109–118.

62 D. W. Hoyt, R. V. F. Turcu, J. A. Sears, K. M. Rosso, S. D. Burton, A. R. Felmy and J. Z. Hu, *J. Magn. Reson.*, 2011, **212**, 378–385.

63 R. V. F. Turcu, D. W. Hoyt, K. M. Rosso, J. A. Sears, J. S. Loring, A. R. Felmy and J. Z. Hu, *J. Magn. Reson.*, 2013, **226**, 64–69.

64 J. Z. Hu, M. Y. Hu, Z. Zhao, S. Xu, A. Vjunov, H. Shi, D. M. Camaioni, C. H. F. Pedena and J. A. Lercher, *Chem. Commun.*, 2015, **51**, 13458–13461.

65 A. Vjunov, M. Y. Hu, J. Feng, D. M. Camaioni, D. Mei, J. Z. Hu, C. Zhao and J. A. Lercher, *Angew. Chem., Int. Ed.*, 2013, **53**, 479–482.

66 E. D. Walter, L. Qi, A. Chamas, H. S. Mehta and D. W. Hoyt, *J. Phys. Chem. C*, 2018, **122**, 8209–8215.

67 X. Yao, Z. Zhao and G. Hou, *Chin. J. Struct. Chem.*, 2022, **41**, 2210045.

68 Z. Zhao, X. Yao and G. Hou, *ACS Catal.*, 2023, **13**, 7978–7986.

69 Q. Han, P. Gao, K. Chen, L. Liang, Z. Zhao, X. Yao, D. Xiao, X. Han and G. Hou, *Chem*, 2023, **9**, 721–738.

70 Y. Ding, F. Jiao, X. Pan, Y. Ji, M. Li, R. Si, Y. Pan, G. Hou and X. Bao, *ACS Catal.*, 2021, **11**, 9729–9737.

71 J. F. Haw, P. W. Goguen, T. Xu, T. W. Skloss and Z. Wang, *Angew. Chem., Int. Ed.*, 1998, **37**, 948–949.

72 P. W. Goguen, T. Xu, D. H. Barich, T. W. Skloss, W. Song, Z. Wang, J. B. Nicholas and J. F. Haw, *J. Am. Chem. Soc.*, 1998, **120**, 2650–2651.

73 Y. Ji, P. Gao, Z. Zhao, D. Xiao, Q. Han, H. Chen, K. Gong, K. Chen, X. Han and X. Bao, *Nat. Catal.*, 2022, **5**, 594–604.

74 M. Hunger and T. Horvath, *Chem. Commun.*, 1995, 1423–1424.

75 M. Hunger and W. Wang, *Chem. Commun.*, 2004, 584–585.

76 M. Hunger and T. Horvath, *J. Catal.*, 1997, **167**, 187–197.

77 S. Xu, W. Zhang, X. Liu, X. Han and X. Bao, *J. Am. Chem. Soc.*, 2009, **131**, 13722–13727.

78 B. Li, J. Xu, B. Han, X. Wang, G. Qi, Z. Zhang, C. Wang and F. Deng, *J. Phys. Chem. C*, 2013, **117**, 5840–5847.

79 T. He, P. Ren, X. Liu, S. Xu, X. Han and X. Bao, *Chem. Commun.*, 2015, **51**, 16868–16870.

80 A. Medek, J. S. Harwood and L. Frydman, *J. Am. Chem. Soc.*, 1995, **117**, 12779–12787.

81 Z. Gan, *J. Am. Chem. Soc.*, 2000, **122**, 3242–3243.

82 A. S. Lilly Thankamony, J. J. Wittmann, M. Kaushik and B. Corzilius, *Prog. Nucl. Magn. Reson. Spectrosc.*, 2017, **102–103**, 120–195.

83 T. Biedenbänder, V. Aladin, S. Saeidpour and B. Corzilius, *Chem. Rev.*, 2022, **122**, 9738–9794.

84 Z. F. Pang, H. X. Guan, L. Gao, W. C. Cao, J. L. Yin and X. Q. Kong, *Acta Phys.-Chim. Sin.*, 2020, **36**, 1906018.

85 K. V. Kovtunov, E. V. Pokochueva, O. G. Salnikov, S. F. Cousin, D. Kurzbach, B. Vuichoud, S. Jannin, E. Y. Chekmenev, B. M. Goodson, D. A. Barskiy and I. V. Koptyug, *Chem. – Asian J.*, 2018, **13**, 1857–1871.

86 W. Wang, R. J. Lewis, B. Lu, Q. Wang, G. J. Hutchings, J. Xu and F. Deng, *ACS Catal.*, 2024, **14**, 2522–2531.

87 A. J. Rossini, A. Zagdoun, M. Lelli, A. Lesage, C. Copéret and L. Emsley, *Acc. Chem. Res.*, 2013, **46**, 1942–1951.

88 W.-C. Liao, B. Ghaffari, C. P. Gordon, J. Xu and C. Copéret, *Curr. Opin. Colloid Interface Sci.*, 2018, **33**, 63–71.

89 Q. Z. Ni, E. Daviso, T. V. Can, E. Markhasin, S. K. Jawla, T. M. Swager, R. J. Temkin, J. Herzfeld and R. G. Griffin, *Acc. Chem. Res.*, 2013, **46**, 1933–1941.

90 A. G. M. Rankin, J. Trébosc, F. Pourpoint, J.-P. Amoureux and O. Lafon, *Solid State Nucl. Magn. Reson.*, 2019, **101**, 116–143.

91 I. B. Moroz and M. Leskes, *Annu. Rev. Mater. Res.*, 2022, **52**, 25–55.

92 F. A. Perras, Z. Wang, P. Naik, I. I. Slowing and M. Pruski, *Angew. Chem., Int. Ed.*, 2017, **56**, 9165–9169.

93 P. Gao, D. Xiao, Z. Zhao, S. Paul, F. Blanc, X. Han, G. Hou and X. Bao, *J. Energy Chem.*, 2022, **67**, 640–644.

94 D. Fu, A. Lucini Paioni, C. Lian, O. van der Heijden, M. Baldus and B. M. Weckhuysen, *Angew. Chem., Int. Ed.*, 2020, **59**, 20024–20030.

95 D. Xiao, S. Xu, N. J. Brownbill, S. Paul, L. H. Chen, S. Pawsey, F. Aussenac, B. L. Su, X. Han, X. Bao, Z. Liu and F. Blanc, *Chem. Sci.*, 2018, **9**, 8184–8193.

96 A. V. Yakimov, D. Mance, K. Searles and C. Copéret, *J. Phys. Chem. Lett.*, 2020, **11**, 3401–3407.

97 A. Dutta Chowdhury, I. Yarulina, E. Abou-Hamad, A. Gurinov and J. Gascon, *Chem. Sci.*, 2019, **10**, 8946–8954.

98 T. C. Ong, W. C. Liao, V. Mougel, D. Gajan, A. Lesage, L. Emsley and C. Copéret, *Angew. Chem., Int. Ed.*, 2016, **55**, 4743–4747.

99 D. Xiao, S. Xu, X. Han, X. Bao, Z. Liu and F. Blanc, *Chem. Sci.*, 2017, **8**, 8309–8314.

100 D. Xiao, X. Han, X. Bao, G. Hou and F. Blanc, *RSC Adv.*, 2019, **9**, 12415–12418.

101 B. Fan, S. Xu, Y. Wei and Z. Liu, *Magn. Reson. Lett.*, 2021, **1**, 11–27.

102 V. Batarchuk, Y. Shepelytskyi, V. Grynko, A. H. Kovacs, A. Hodgson, K. Rodriguez, R. Aldossary, T. Talwar, C. Hasselbrink, I. C. Ruset, B. DeBoef and M. S. Albert, *Int. J. Mol. Sci.*, 2024, **25**, 1939–1975.

103 D. Wisser and M. Hartmann, *Adv. Mater. Interfaces*, 2020, **8**, 2001266.

104 E. Weiland, M.-A. Springuel-Huet, A. Nossov and A. Gédéon, *Microporous Mesoporous Mater.*, 2016, **225**, 41–65.

105 S. Gao, S. Xu, Y. Wei, Q. Qiao, Z. Xu, X. Wu, M. Zhang, Y. He, S. Xu and Z. Liu, *J. Catal.*, 2018, **367**, 306–314.

106 S. Gao, S. Xu, Y. Wei, Z. Liu, A. Zheng, P. Wu and Z. Liu, *Chem. Commun.*, 2019, **55**, 10693–10696.

107 T. He, X. Liu, S. Xu, X. Han, X. Pan, G. Hou and X. Bao, *J. Phys. Chem. C*, 2016, **120**, 22526–22531.

108 J. Zhao, W. Qian, H. Ma, W. Ying, P. Yuan and H. Zhang, *ACS Omega*, 2023, **8**, 22067–22076.

109 J. Xu, Q. Wang, S. Li and F. Deng, in *Solid-State NMR in Zeolite Catalysis*, ed. J. Xu, Q. Wang, S. Li and F. Deng, Springer, Singapore, 2019, pp. 159–197.

110 A. M. Gronenborn and T. Polenova, *Chem. Rev.*, 2022, **122**, 9265–9266.

111 Y. Ji, L. Liang, X. Bao and G. Hou, *Solid State Nucl. Magn. Reson.*, 2021, **112**, 101711.

112 G. De Paëpe, *Annu. Rev. Phys. Chem.*, 2012, **63**, 661–684.

113 G. Hou, S. Yan, J. Trébosc, J.-P. Amoureux and T. Polenova, *J. Magn. Reson.*, 2013, **232**, 18–30.

114 L. B. Krivdin and E. W. Della, *Prog. Nucl. Magn. Reson. Spectrosc.*, 1991, **23**, 301–610.

115 V. Ladizhansky, R. S. Palani, M. Mardini and R. G. Griffin, *Chem. Rev.*, 2024, **124**, 12844–12917.

116 A. A. Shcherbakov, J. Medeiros-Silva, N. Tran, M. D. Gelenter and M. Hong, *Chem. Rev.*, 2021, **122**, 9848–9879.

117 M. Veshtort and R. G. Griffin, *J. Chem. Phys.*, 2011, **135**, 134509.

118 M. Weingarth, D. E. Demco, G. Bodenhausen and P. Tekely, *Chem. Phys. Lett.*, 2009, **469**, 342–348.

119 X. Wu, S. Xu, Y. Wei, W. Zhang, J. Huang, S. Xu, Y. He, S. Lin, T. Sun and Z. Liu, *ACS Catal.*, 2018, **8**, 7356–7361.

120 A. D. Chowdhury, A. L. Paioni, K. Houben, G. T. Whiting, M. Baldus and B. M. Weckhuysen, *Angew. Chem., Int. Ed.*, 2018, **57**, 8095–8099.

121 T. Sun, W. Chen, S. Xu, A. Zheng, X. Wu, S. Zeng, N. Wang, X. Meng, Y. Wei and Z. Liu, *Chem*, 2021, **7**, 2415–2428.

122 Y. Sun, L. Liang, M. Yang, Y. Ji, G. Hou and K. Chen, *J. Am. Chem. Soc.*, 2025, **147**, 10160–10171.

123 Z. Yu, S. Li, Q. Wang, A. Zheng, X. Jun, L. Chen and F. Deng, *J. Phys. Chem. C*, 2011, **115**, 22320–22327.

124 E. Dib, J. Grand, A. Gedeon, S. Mintova and C. Fernandez, *Microporous Mesoporous Mater.*, 2021, **315**, 110899.

125 Y. Tong, L. Zhang, H. Ma, Y. Wang and X. Liu, *Materials*, 2024, **17**, 2824.

126 S. Li, A. Zheng, Y. Su, H. Zhang, L. Chen, J. Yang, C. Ye and F. Deng, *J. Am. Chem. Soc.*, 2007, **129**, 11161–11171.

127 R. M. Shayib, N. C. George, R. Seshadri, A. W. Burton, S. I. Zones and B. F. Chmelka, *J. Am. Chem. Soc.*, 2011, **133**, 18728–18741.

128 S. Li, S.-J. Huang, W. Shen, H. Zhang, H. Fang, A. Zheng, S.-B. Liu and F. Deng, *J. Phys. Chem. C*, 2008, **112**, 14486–14494.

129 G. Brunklaus, H. Koller and S. I. Zones, *Angew. Chem., Int. Ed.*, 2016, **55**, 14459–14463.

130 J. Dědeček, E. Tabor and S. Sklenak, *ChemSusChem*, 2019, **12**, 556–576.

131 A. Lesage, M. Bardet and L. Emsley, *J. Am. Chem. Soc.*, 1999, **121**, 10987–10993.

132 R. Giovine, J. Trébosc, F. Pourpoint, O. Lafon and J.-P. Amoureux, *J. Magn. Reson.*, 2019, **299**, 109–123.

133 J. Trebosc, B. Hu, J. P. Amoureux and Z. Gan, *J. Magn. Reson.*, 2007, **186**, 220–227.

134 G. Tricot, J. Trébosc, F. Pourpoint, R. Gauvin and L. Delevoye, *Annu. Rep. NMR Spectrosc.*, 2014, **81**, 145–184.

135 R. Zhang, K. H. Mroue and A. Ramamoorthy, *J. Magn. Reson.*, 2016, **266**, 59–66.

136 R. Zhang and A. Ramamoorthy, *J. Magn. Reson.*, 2014, **243**, 85–92.

137 M. B. Schmithorst, S. Prasad, A. Moini and B. F. Chmelka, *J. Am. Chem. Soc.*, 2023, **145**, 18215–18220.

138 T. Gullion and J. Schaefer, *J. Magn. Reson.*, 1989, **81**, 196–200.

139 C. P. Grey and A. J. Vega, *J. Am. Chem. Soc.*, 1995, **117**, 8232–8242.

140 A. Goldbourt, S. Vega, T. Gullion and A. J. Vega, *J. Am. Chem. Soc.*, 2003, **125**, 11194–11195.

141 T. Gullion, *Chem. Phys. Lett.*, 1995, **246**, 325–330.

142 A. Brinkmann and A. P. M. Kentgens, *J. Am. Chem. Soc.*, 2006, **128**, 14758–14759.

143 L. Chen, Q. Wang, B. Hu, O. Lafon, J. Trébosc, F. Deng and J.-P. Amoureux, *Phys. Chem. Chem. Phys.*, 2010, **12**, 9395–9405.

144 J. Kärger, *ChemPhysChem*, 2015, **16**, 24–51.

145 Z. Qin, S. Zeng, G. Melinte, T. Bučko, M. Badawi, Y. Shen, J.-P. Gilson, O. Ersen, Y. Wei, Z. Liu, X. Liu, Z. Yan, S. Xu, V. Valtchev and S. Mintova, *Adv. Sci.*, 2021, **8**, 2100001.

146 S. Gao, F. Ye, S. Xu, Y. Wei and Z. Liu, *Chem. Commun.*, 2025, **61**, 3636–3648.

147 S. Gao, J. Yuan, Z. Liu, C. Lou, Z. Yu, S. Xu, A. Zheng, P. Wu, Y. Wei and Z. Liu, *J. Phys. Chem. C*, 2021, **125**, 6832–6838.

148 S. Gao, Z. Liu, S. Xu, A. Zheng, P. Wu, B. Li, X. Yuan, Y. Wei and Z. Liu, *J. Catal.*, 2019, **377**, 51–62.

149 Z. Liu, J. Yuan, J. M. van Baten, J. Zhou, X. Tang, C. Zhao, W. Chen, X. Yi, R. Krishna, G. Sastre and A. Zheng, *Sci. Adv.*, 2021, **7**, eabf0775.

150 Z. Liu, J. Zhou, X. Tang, F. Liu, J. Yuan, G. Li, L. Huang, R. Krishna, K. Huang and A. Zheng, *AIChE J.*, 2020, **66**, e16269.

151 J. Yuan, Z. Liu, Y. Wu, J. Han, X. Tang, C. Li, W. Chen, X. Yi, J. Zhou, R. Krishna, G. Sastre and A. Zheng, *Proc. Natl. Acad. Sci. U. S. A.*, 2021, **118**, e2102097118.

152 Z. Liu, C. Lou, J. Yuan, X. Tang, Y. Fan, J. Qi, R. Zhang, P. Peng, G. Liu, S. Xu and A. Zheng, *J. Am. Chem. Soc.*, 2025, **147**, 6126–6136.

153 C. D. Chang and A. J. Silvestri, *J. Catal.*, 1977, **47**, 249–259.

154 S. Lin, Y. Zhi, Z. Liu, J. Yuan, W. Liu, W. Zhang, Z. Xu, A. Zheng, Y. Wei and Z. Liu, *Natl. Sci. Rev.*, 2022, **9**, nwac151.

155 J. Liang, H. Li, S. Zhao, W. Guo, R. Wang and M. Ying, *Appl. Catal.*, 1990, **64**, 31–40.

156 Y.-H. Chen, W. Hsieh, H. Chang and C.-D. Ho, *J. Taiwan Inst. Chem. Eng.*, 2022, **130**, 103893.

157 J. Q. Chen, A. Bozzano, B. Glover, T. Fuglerud and S. Kvisle, *Catal. Today*, 2005, **106**, 103–107.

158 J. Haggin, *Chem. Eng. News*, 1985, **63**, 39–41.

159 M. R. Gogate, *Pet. Sci. Technol.*, 2019, **37**, 559–565.

160 S. Lin, Y. Wei and Z. Liu, *Chem. Catal.*, 2023, **3**, 100597.

161 X. Gong, M. Çağlayan, Y. Ye, K. Liu, J. Gascon and A. Dutta Chowdhury, *Chem. Rev.*, 2022, **122**, 14275–14345.

162 W. Song, D. M. Marcus, H. Fu, J. O. Ehresmann and J. F. Haw, *J. Am. Chem. Soc.*, 2002, **124**, 3844–3845.

163 W. Wang, A. Buchholz, M. Seiler and M. Hunger, *J. Am. Chem. Soc.*, 2003, **125**, 15260–15267.

164 J. Li, Z. Wei, Y. Chen, B. Jing, Y. He, M. Dong, H. Jiao, X. Li, Z. Qin, J. Wang and W. Fan, *J. Catal.*, 2014, **317**, 277–283.

165 A. D. Chowdhury, K. Houben, G. T. Whiting, M. Mokhtar, A. M. Asiri, S. A. Al-Thabaiti, S. N. Basahel, M. Baldus and B. M. Weckhuysen, *Angew. Chem., Int. Ed.*, 2016, **55**, 15840–15845.

166 Y. Liu, S. Muller, D. Berger, J. Jelic, K. Reuter, M. Tonigold, M. Sanchez-Sanchez and J. A. Lercher, *Angew. Chem., Int. Ed.*, 2016, **55**, 5723–5726.

167 C. Wang, Y. Chu, J. Xu, Q. Wang, G. Qi, P. Gao, X. Zhou and F. Deng, *Angew. Chem., Int. Ed.*, 2018, **57**, 10197–10201.

168 X. Wu, S. Xu, W. Zhang, J. Huang, J. Li, B. Yu, Y. Wei and Z. Liu, *Angew. Chem., Int. Ed.*, 2017, **56**, 9039–9043.

169 W. Chen, K. A. Tarach, K. Góra-Marek and A. Zheng, *Appl. Catal., B*, 2024, **357**, 124306.

170 Y. Jiang, M. Hunger and W. Wang, *J. Am. Chem. Soc.*, 2006, **128**, 11679–11692.

171 M. Hu, C. Wang, Y. Chu, Q. Wang, S. Li, J. Xu and F. Deng, *Angew. Chem., Int. Ed.*, 2022, **61**, e202207400.

172 G. Li, C. Foo, X. Yi, W. Chen, P. Zhao, P. Gao, T. Yoskamtorn, Y. Xiao, S. Day, C. C. Tang, G. Hou, A. Zheng and S. C. E. Tsang, *J. Am. Chem. Soc.*, 2021, **143**, 8761–8771.

173 F. Liu, X. Yi, T. Liu, W. Chen, J. Yang, Y. Xiao, Y. Qin, L. Song and A. Zheng, *Sci. Adv.*, 2025, **11**, eads4018.

174 X. Wu, W. Chen, S. Xu, S. Lin, T. Sun, A. Zheng, Y. Wei and Z. Liu, *ACS Cent. Sci.*, 2021, **7**, 681–687.

175 V. Paunović, P. Hemberger, A. Bodi, R. Hauert and J. A. van Bokhoven, *ACS Catal.*, 2022, **12**, 13426–13434.

176 S. Lin, Y. Zhi, W. Zhang, X. Yuan, C. Zhang, M. Ye, S. Xu, Y. Wei and Z. Liu, *Chin. J. Catal.*, 2023, **46**, 11–27.

177 X. Wu, *Process and Engineering of Low Carbon Olefins from Coal*, Chemical Industry Press, China, 2014, pp. 357–358.

178 A. Comas-Vives, M. Valla, C. Coperet and P. Sautet, *ACS Cent. Sci.*, 2015, **1**, 313–319.

179 P. N. Plessow and F. Studt, *ACS Catal.*, 2017, **7**, 7987–7994.

180 P. N. Plessow, A. Smith, S. Tischer and F. Studt, *J. Am. Chem. Soc.*, 2019, **141**, 5908–5915.

181 A. Cesarini, S. Mitchell, G. Zichittella, M. Agrachev, S. P. Schmid, G. Jeschke, Z. Pan, A. Bodi, P. Hemberger and J. Pérez-Ramírez, *Nat. Catal.*, 2022, **5**, 605–614.

182 L. Yang, T. Yan, C. Wang, W. Dai, G. Wu, M. Hunger, W. Fan, Z. Xie, N. Guan and L. Li, *ACS Catal.*, 2019, **9**, 6491–6501.

183 M. Ravi, V. L. Sushkevich and J. A. van Bokhoven, *Nat. Mater.*, 2020, **19**, 1047–1056.

184 X. Yi, K. Liu, W. Chen, J. Li, S. Xu, C. Li, Y. Xiao, H. Liu, X. Guo, S.-B. Liu and A. Zheng, *J. Am. Chem. Soc.*, 2018, **140**, 10764–10774.

185 X. Yi, H.-H. Ko, F. Deng, S.-B. Liu and A. Zheng, *Nat. Protoc.*, 2020, **15**, 3527–3555.

186 S. Müller, Y. Liu, F. M. Kirchberger, M. Tonigold, M. Sanchez-Sanchez and J. A. Lercher, *J. Am. Chem. Soc.*, 2016, **138**, 15994–16003.

187 Y. Chu, X. Yi, C. Li, X. Sun and A. Zheng, *Chem. Sci.*, 2018, **9**, 6470–6479.

188 F. Pourpoint, J. Trébosc, R. M. Gauvin, Q. Wang, O. Lafon, F. Deng and J.-P. Amoureux, *ChemPhysChem*, 2012, **13**, 3605–3615.

189 C. W. P. Pare, P. Rzepka, P. Hemberger, A. Bodi, R. Hauert, J. A. van Bokhoven and V. Paunović, *ACS Catal.*, 2023, **14**, 463–474.

190 Y. Liu, F. M. Kirchberger, S. Müller, M. Eder, M. Tonigold, M. Sanchez-Sanchez and J. A. Lercher, *Nat. Commun.*, 2019, **10**, 1462.

191 X. Zhang, X. Gong, E. Abou-Hamad, H. Zhou, X. You, J. Gascon and A. Dutta Chowdhury, *Angew. Chem., Int. Ed.*, 2024, **136**, e202411197.

192 B. L. Foley, B. A. Johnson and A. Bhan, *ACS Catal.*, 2021, **11**, 3628–3637.

193 P. Bollini, T. T. Chen, M. Neurock and A. Bhan, *Catal. Sci. Technol.*, 2019, **9**, 4374–4383.

194 S. Bailleul, I. Yarulina, A. E. J. Hoffman, A. Dokania, E. Abou-Hamad, A. D. Chowdhury, G. Pieters, J. Hajek, K. De Wispelaere, M. Waroquier, J. Gascon and V. Van Speybroeck, *J. Am. Chem. Soc.*, 2019, **141**, 14823–14842.

195 A. E. Enss, P. Huber, P. N. Plessow and F. Studt, *J. Phys. Chem. C*, 2024, **128**, 15367–15379.

196 H. Wang, B. Shen, X. Chen, H. Xiong, H. Wang, W. Song, C. Cui, F. Wei and W. Qian, *Nat. Commun.*, 2022, **13**, 2924.

197 X. Sun, S. Mueller, H. Shi, G. L. Haller, M. Sanchez-Sanchez, A. C. van Veen and J. A. Lercher, *J. Catal.*, 2014, **314**, 21–31.

198 Y. Zuo, Y. Zhang, Q. Ren, Y. Xu, Y. Luo and X. Shu, *Catal. Commun.*, 2022, **168**, 106461.

199 R. M. Dessau and R. B. LaPierre, *J. Catal.*, 1982, **78**, 136–141.

200 J. Ke, W.-D. Hu, Y.-J. Du, Y.-D. Wang, C.-M. Wang and Z.-K. Xie, *ACS Catal.*, 2023, **13**, 8642–8661.

201 C. Liu, E. A. Uslamin, E. A. Pidko and F. Kapteijn, *ACS Catal.*, 2023, **13**, 5205–5212.

202 W. Song, J. B. Nicholas and J. F. Haw, *J. Phys. Chem. B*, 2001, **105**, 4317–4323.

203 F. G. Oliver, E. J. Munson and J. F. Haw, *J. Phys. Chem.*, 1992, **96**, 8106–8111.

204 J. F. Haw, J. B. Nicholas, W. Song, F. Deng, Z. Wang, T. Xu and C. S. Heneghan, *J. Am. Chem. Soc.*, 2000, **122**, 4763–4775.

205 W. Song, J. B. Nicholas, A. Sassi and J. F. Haw, *Catal. Lett.*, 2002, **81**, 49–53.

206 C. Wang, X. Yi, J. Xu, G. Qi, P. Gao, W. Wang, Y. Chu, Q. Wang, N. Feng, X. Liu, A. Zheng and F. Deng, *Chem. – Eur. J.*, 2015, **21**, 12061–12068.

207 M. Seiler, W. Wang, A. Buchholz and M. Hunger, *Catal. Lett.*, 2003, **88**, 187–191.

208 J. Li, Y. Wei, J. Chen, P. Tian, X. Su, S. Xu, Y. Qi, Q. Wang, Y. Zhou, Y. He and Z. Liu, *J. Am. Chem. Soc.*, 2012, **134**, 836–839.

209 S. Xu, A. Zheng, Y. Wei, J. Chen, J. Li, Y. Chu, M. Zhang, Q. Wang, Y. Zhou, J. Wang, F. Deng and Z. Liu, *Angew. Chem., Int. Ed.*, 2013, **52**, 11778–11782.

210 C. Wang, Q. Wang, J. Xu, G. Qi, P. Gao, W. Wang, Y. Zou, N. Feng, X. Liu and F. Deng, *Angew. Chem., Int. Ed.*, 2016, **55**, 2507–2511.

211 C. Wang, J. Xu, Q. Wang, X. Zhou, G. Qi, N. Feng, X. Liu, X. Meng, F. Xiao and F. Deng, *ACS Catal.*, 2017, **7**, 6094–6103.

212 C. Wang, Y. Chu, M. Hu, W. Cai, Q. Wang, G. Qi, S. Li, J. Xu and F. Deng, *Angew. Chem., Int. Ed.*, 2021, **60**, 26847–26854.

213 S. Wang, Y. Chen, Z. Qin, T.-S. Zhao, S. Fan, M. Dong, J. Li, W. Fan and J. Wang, *J. Catal.*, 2019, **369**, 382–395.

214 M. Vandichel, D. Lesthaeghe, J. V. D. Mynsbrugge, M. Waroquier and V. Van Speybroeck, *J. Catal.*, 2010, **271**, 67–78.

215 W. Dai, C. Wang, M. Dyballa, G. Wu, N. Guan, L. Li, Z. Xie and M. Hunger, *ACS Catal.*, 2014, **5**, 317–326.

216 I. B. Minova, S. K. Matam, A. Greenaway, C. R. A. Catlow, M. D. Frogley, G. Cinque, P. A. Wright and R. F. Howe, *ACS Catal.*, 2019, **9**, 6564–6570.

217 W. Zhang, M. Zhang, S. Xu, S. Gao, Y. Wei and Z. Liu, *ACS Catal.*, 2020, **10**, 4510–4516.

218 M. Westgård Erichsen, S. Svelle and U. Olsbye, *Catal. Today*, 2013, **215**, 216–223.

219 M. Hu, C. Wang, X. Gao, Y. Chu, G. Qi, Q. Wang, G. Xu, J. Xu and F. Deng, *ACS Catal.*, 2020, **10**, 4299–4305.

220 S. Fan, H. Wang, S. He, K. Yuan, P. Wang, J. Li, S. Wang, Z. Qin, M. Dong, W. Fan and J. Wang, *ACS Catal.*, 2022, **12**, 12477–12487.

221 W. Zhang, Y. Zhi, J. Huang, X. Wu, S. Zeng, S. Xu, A. Zheng, Y. Wei and Z. Liu, *ACS Catal.*, 2019, **9**, 7373–7379.

222 S. Lin, Y. Zhi, W. Chen, H. Li, W. Zhang, C. Lou, X. Wu, S. Zeng, S. Xu, J. Xiao, A. Zheng, Y. Wei and Z. Liu, *J. Am. Chem. Soc.*, 2021, **143**, 12038–12052.

223 S. Zeng, W. Zhang, J. Li, S. Lin, S. Xu, Y. Wei and Z. Liu, *J. Catal.*, 2022, **413**, 517–526.

224 A. D. Chowdhury, A. Lucini Paioni, G. T. Whiting, D. Fu, M. Baldus and B. M. Weckhuysen, *Angew. Chem., Int. Ed.*, 2019, **58**, 3908–3912.

225 Y. Wu, J. Han, W. Zhang, Z. Yu, K. Wang, X. Fang, Y. Wei and Z. Liu, *J. Am. Chem. Soc.*, 2024, **146**, 8086–8097.

226 C. Wang, L. Yang, M. Gao, X. Shao, W. Dai, G. Wu, N. Guan, Z. Xu, M. Ye and L. Li, *J. Am. Chem. Soc.*, 2022, **144**, 21408–21416.

227 J. Zhou, Y. Zhi, J. Zhang, Z. Liu, T. Zhang, Y. He, A. Zheng, M. Ye, Y. Wei and Z. Liu, *J. Catal.*, 2019, **377**, 153–162.

228 J. Zhou, M. Gao, J. Zhang, W. Liu, T. Zhang, H. Li, Z. Xu, M. Ye and Z. Liu, *Nat. Commun.*, 2021, **12**, 17.

229 Y. Ni, W. Zhu and Z. Liu, *ACS Catal.*, 2019, **9**, 11398–11403.

230 L. Maggiulli, V. L. Sushkevich, O. Kröcher, J. A. van Bokhoven and D. Ferri, *ACS Catal.*, 2024, **14**, 11477–11489.

231 P. Cnudde, R. Demuynck, S. Vandenbrande, M. Waroquier, G. Sastre and V. V. Speybroeck, *J. Am. Chem. Soc.*, 2020, **142**, 6007–6017.
232 P. Ferri, C. Li, C. Paris, A. Vidal-Moya, M. Moliner, M. Boronat and A. Corma, *ACS Catal.*, 2019, **9**, 11542–11551.
233 P. Ferri, C. Li, C. Paris, A. Rodríguez-Fernández, M. Moliner, M. Boronat and A. Corma, *ChemCatChem*, 2021, **13**, 1578–1586.
234 W. Zhang, S. Lin, Y. Wei, P. Tian, M. Ye and Z. Liu, *Natl. Sci. Rev.*, 2023, **10**, nwad120.
235 M. Yang, B. Li, M. Gao, S. Lin, Y. Wang, S. Xu, X. Zhao, P. Guo, Y. Wei, M. Ye, P. Tian and Z. Liu, *ACS Catal.*, 2020, **10**, 3741–3749.
236 J. Goetze, I. Yarulina, J. Gascon, F. Kapteijn and B. M. Weckhuysen, *ACS Catal.*, 2018, **8**, 2060–2070.
237 J. H. Kang, F. H. Alshafei, S. I. Zones and M. E. Davis, *ACS Catal.*, 2019, **9**, 6012–6019.
238 P. Vinaches and S. Pergher, *Appl. Sci.*, 2020, **10**, 303–315.
239 C. Li, C. Paris, J. Martínez-Triguero, M. Boronat, M. Moliner and A. Corma, *Nat. Catal.*, 2018, **1**, 547–554.
240 E. T. C. Vogt, D. Fu and B. M. Weckhuysen, *Angew. Chem., Int. Ed.*, 2023, **62**, e202300319.
241 D. Rojo-Gama, M. Nielsen, D. S. Wragg, M. Dyballa, J. Holzinger, H. Falsig, L. F. Lundegaard, P. Beato, R. Y. Brogaard, K. P. Lillerud, U. Olsbye and S. Svelle, *ACS Catal.*, 2017, **7**, 8235–8246.
242 S. Fan, H. Wang, S. Wang, M. Dong and W. Fan, *Sci. China: Chem.*, 2024, **67**, 3934–3943.
243 H. An, F. Zhang, Z. Guan, X. Liu, F. Fan and C. Li, *ACS Catal.*, 2018, **8**, 9207–9215.
244 I. Lezcano-Gonzalez, E. Campbell, A. E. J. Hoffman, M. Bocus, I. V. Sazanovich, M. Towrie, M. Agote-Aran, E. K. Gibson, A. Greenaway, K. De Wispelaere, V. Van Speybroeck and A. M. Beale, *Nat. Mater.*, 2020, **19**, 1081–1087.
245 S. Fan, H. Wang, P. Wang, W. Jiao, S. Wang, Z. Qin, M. Dong, J. Wang and W. Fan, *Chem. Catal.*, 2024, **4**, 100927.
246 N. Wang, L. Wang, Y. Zhi, J. Han, C. Zhang, X. Wu, J. Zhang, L. Wang, B. Fan, S. Xu, Y. Zheng, S. Lin, R. Wu, Y. Wei and Z. Liu, *J. Energy Chem.*, 2023, **76**, 105–116.
247 N. Wang, Y. Zhi, Y. Wei, W. Zhang, Z. Liu, J. Huang, T. Sun, S. Xu, S. Lin, Y. He, A. Zheng and Z. Liu, *Nat. Commun.*, 2020, **11**, 1079.
248 J. T. C. Wennmacher, S. Mahmoudi, P. Rzepka, S. Sik Lee, T. Gruene, V. Paunović and J. A. van Bokhoven, *Angew. Chem., Int. Ed.*, 2022, **61**, e202205413.
249 K. H. Cats, J. C. Andrews, O. Stéphan, K. March, C. Karunakaran, F. Meirer, F. M. F. de Groot and B. M. Weckhuysen, *Catal. Sci. Technol.*, 2016, **6**, 4438–4449.
250 J. E. Schmidt, J. D. Poplawsky, B. Mazumder, Ö. Attila, D. Fu, D. A. M. de Winter, F. Meirer, S. R. Bare and B. M. Weckhuysen, *Angew. Chem., Int. Ed.*, 2016, **55**, 11173–11177.
251 S. H. van Vreeswijk, L. A. Parker, J. J. E. Maris, J. D. Poplawsky and B. M. Weckhuysen, *ChemPhysChem*, 2023, **24**, e202300094.
252 M. Gao, H. Li, W. Liu, Z. Xu, S. Peng, M. Yang, M. Ye and Z. Liu, *Nat. Commun.*, 2020, **11**, 3641.
253 G. T. Whiting, N. Nikolopoulos, I. Nikolopoulos, A. D. Chowdhury and B. M. Weckhuysen, *Nat. Chem.*, 2018, **11**, 23–31.
254 B. Luna-Murillo, M. Pala, A. L. Paioni, M. Baldus, F. Ronsse, W. Prins, P. C. A. Bruijnincx and B. M. Weckhuysen, *ACS Sustainable Chem. Eng.*, 2021, **9**, 291–304.
255 S. H. van Vreeswijk, L. A. Parker, A. T. Sanderse, R. Oord, F. Meirer and B. M. Weckhuysen, *Chem. Catal.*, 2024, **4**, 101134.
256 C. Yuan, Y. Wei, J. Li, S. Xu, J. Chen, Y. Zhou, Q. Wang, L. Xu and Z. Liu, *Chin. J. Catal.*, 2013, **33**, 367–374.
257 Y. Wei, J. Li, C. Yuan, S. Xu, Y. Zhou, J. Chen, Q. Wang, Q. Zhang and Z. Liu, *Chem. Commun.*, 2012, **48**, 3082–3084.
258 P. Rzepka, D. Sheptyakov, C. Wang, J. A. van Bokhoven and V. Paunović, *ACS Catal.*, 2024, **14**, 5593–5604.
259 D. Mance, J. van der Zwan, M. E. Z. Velthoen, F. Meirer, B. M. Weckhuysen, M. Baldus and E. T. C. Vogt, *Chem. Commun.*, 2017, **53**, 3933–3936.
260 C. Wang, M. Hu, Y. Chu, X. Zhou, Q. Wang, G. Qi, S. Li, J. Xu and F. Deng, *Angew. Chem., Int. Ed.*, 2020, **59**, 7198–7202.
261 W. Dai, G. Wu, L. Li, N. Guan and M. Hunger, *ACS Catal.*, 2013, **3**, 588–596.
262 C. Wang, T. Aztiria, P. Rzepka, R. Verel, J. Xu, F. Deng, J. A. van Bokhoven and V. Paunović, *ACS Catal.*, 2024, **14**, 12410–12424.
263 Y. Wu, J. Zhang, Z. Shi, C. Chen, X. Yue and Q. Sun, *Chem. – Asian J.*, 2024, **19**, e202400436.
264 B. Shen, X. Chen, X. Fan, H. Xiong, H. Wang, W. Qian, Y. Wang and F. Wei, *Nat. Commun.*, 2021, **12**, 2212.
265 T. T. Le, W. Qin, A. Agarwal, N. Nikolopoulos, D. Fu, M. D. Patton, C. Weiland, S. R. Bare, J. C. Palmer, B. M. Weckhuysen and J. D. Rimer, *Nat. Catal.*, 2023, **6**, 254–265.
266 K. De Wispelaere, C. S. Wondergem, B. Ensing, K. Hemelsoet, E. J. Meijer, B. M. Weckhuysen, V. Van Speybroeck and J. Ruiz-Martínez, *ACS Catal.*, 2016, **6**, 1991–2002.
267 J. Valecillos, G. Elordi, A. T. Aguayo and P. Castaño, *Catal. Sci. Technol.*, 2021, **11**, 1269–1281.
268 C. Zhang, X. Wu, Y. Zhang, L. Wang, Y. Jin, M. Gao, M. Ye, Y. Wei and Z. Liu, *ACS Catal.*, 2025, **15**, 1553–1562.
269 C. Zhang, X. Wu, Y. Zhang, W. Zhang, S. Lin, C. Lou, S. Xu, D. He, L. Wang, Y. Wei and Z. Liu, *Chem. Catal.*, 2024, **4**, 101025.
270 T. Sun, S. Xu, D. Xiao, Z. Liu, G. Li, A. Zheng, W. Liu, Z. Xu, Y. Cao, Q. Guo, N. Wang, Y. Wei and Z. Liu, *Angew. Chem., Int. Ed.*, 2020, **59**, 20672–20681.
271 L. Yang, C. Wang, L. Zhang, W. Dai, Y. Chu, J. Xu, G. Wu, M. Gao, W. Liu, Z. Xu, P. Wang, N. Guan, M. Dyballa, M. Ye, F. Deng, W. Fan and L. Li, *Nat. Commun.*, 2021, **12**, 4661.
272 Y. Chen, X. Ma, J. H. Hack, S. Zhang, A. Peng, J. P. Dombrowski, G. A. Voth, A. Tokmakoff, M. C. Kung and H. H. Kung, *J. Am. Chem. Soc.*, 2024, **146**, 10342–10356.

273 C. Wang, Y. Chu, D. Xiong, H. Wang, M. Hu, Q. Wang, J. Xu and F. Deng, *Angew. Chem., Int. Ed.*, 2023, **63**, e202313974.

274 C. Wang, M. Zheng, M. Hu, W. Cai, Y. Chu, Q. Wang, J. Xu and F. Deng, *J. Am. Chem. Soc.*, 2024, **146**, 8688–8696.

275 A. Akbari, H. Haji Andevary and M. Omidkhah, *Chem. Eng. Process.*, 2024, **201**, 109821.

276 J. Zhou, J. Zhao, J. Zhang, T. Zhang, M. Ye and Z. Liu, *Chin. J. Catal.*, 2020, **41**, 1048–1061.

277 Q. Liu and J. A. van Bokhoven, *Chem. Soc. Rev.*, 2024, **53**, 3065–3095.

278 X. Zhao, J. Li, P. Tian, L. Wang, X. Li, S. Lin, X. Guo and Z. Liu, *ACS Catal.*, 2019, **9**, 3017–3025.

279 P. Cheung, A. Bhan, G. J. Sunley and E. Iglesia, *Angew. Chem., Int. Ed.*, 2006, **118**, 1647–1650.

280 K. Fujimoto, T. Shikada, K. Omata and H.-O. Tominaga, *Chem. Lett.*, 1984, 2047–2050.

281 A. Bhan, A. D. Allian, G. J. Sunley, D. J. Law and E. Iglesia, *J. Am. Chem. Soc.*, 2007, **129**, 4919–4924.

282 J. Liu, H. Xue, X. Huang, P. Wu, S. Huang, S. Liu and W. Shen, *Chin. J. Catal.*, 2010, **31**, 729–738.

283 L. Feng, J. Guo, J. Pang, M. Yin, Y. Zhao, P. Wu and M. Zheng, *Green Chem.*, 2024, **26**, 8564–8582.

284 A. Bhan and E. Iglesia, *Acc. Chem. Res.*, 2008, **41**, 559–567.

285 P. Cheung, A. Bhan, G. J. Sunley, D. J. Law and E. Iglesia, *J. Catal.*, 2007, **245**, 110–123.

286 W. Chen, G. Li, X. Yi, S. J. Day and A. Zheng, *J. Am. Chem. Soc.*, 2021, **143**, 15440–15452.

287 H. Zhou, W. Zhu, L. Shi, H. Liu, S. Liu, Y. Ni, Y. Liu, Y. He, S. Xu, L. Li and Z. Liu, *J. Mol. Catal. A: Chem.*, 2016, **417**, 1–9.

288 F. Jiao, X. Pan, K. Gong, Y. Chen, G. Li and X. Bao, *Angew. Chem., Int. Ed.*, 2018, **57**, 4692–4696.

289 Z. Cheng, S. Huang, Y. Li, K. Cai, Y. Wang, M.-Y. Wang, J. Lv and X. Ma, *ACS Catal.*, 2021, **11**, 5647–5657.

290 D. B. Rasmussen, J. M. Christensen, B. Temel, F. Studt, P. G. Moses, J. Rossmeisl, A. Riisager and A. D. Jensen, *Angew. Chem., Int. Ed.*, 2015, **54**, 7261–7264.

291 Y. Zhang, P. Gao, F. Jiao, Y. Chen, Y. Ding, G. Hou, X. Pan and X. Bao, *J. Am. Chem. Soc.*, 2022, **144**, 18251–18258.

292 X. Feng, F. Chen, Z.-M. He, X. Zhao and J. Cao, *Energy Fuels*, 2022, **36**, 14341–14348.

293 Z. Xiong, G. Qi, E. Zhan, Y. Chu, J. Xu, J. Wei, N. Ta, A. Hao, Y. Zhou and F. Deng, *Chem*, 2023, **9**, 76–92.

294 R. Gounder and E. Iglesia, *J. Am. Chem. Soc.*, 2009, **131**, 1958–1971.

295 R. Gounder and E. Iglesia, *Angew. Chem., Int. Ed.*, 2010, **49**, 808–811.

296 R. Gounder and E. Iglesia, *Acc. Chem. Res.*, 2012, **45**, 229–238.

297 R. Gounder and E. Iglesia, *Chem. Commun.*, 2013, **49**, 3491–3509.

298 K. Cao, D. Fan, M. Gao, B. Fan, N. Chen, L. Wang, P. Tian and Z. Liu, *ACS Catal.*, 2021, **12**, 1–7.

299 J. Liu, H. Xue, X. Huang, Y. Li and W. Shen, *Catal. Lett.*, 2010, **139**, 33–37.

300 Z. Cheng, S. Huang, Y. Li, K. Cai, D. Yao, J. Lv, S. Wang and X. Ma, *Appl. Catal., A*, 2019, **576**, 1–10.

301 X. Wang, R. Li, C. Yu, Y. Liu, C. Xu and C. Lu, *Fuel*, 2021, **286**, 119480.

302 M. Xie, X. Fang, H. Liu, Z. Chen, B. Li, L. Yang and W. Zhu, *ACS Catal.*, 2023, **13**, 14327–14333.

303 W. Chen, K. A. Tarach, X. Yi, Z. Liu, X. Tang, K. GóraMarek and A. Zheng, *Nat. Commun.*, 2022, **13**, 7106.

304 Z. Liu, X. Yi, G. Wang, X. Tang, G. Li, L. Huang and A. Zheng, *J. Catal.*, 2019, **369**, 335–344.

305 W. Liu, Y. Wang, L. Bu, K. Chu, Y. Huang, N. Guo, L. Qu, J. Sang, X. Su, X. Zhang and Y. Li, *Materials*, 2024, **17**, 17–34.

306 R. Pengyu, L. Zhuo, Q. Yanhong, G. Junjun, M. Hong, W. Jianbing and W. Yongzhao, *J. Fuel Chem. Technol.*, 2024, **52**, 323–334.

307 Y. Li, M. Yu, G. Qi, Y. Liu, J. Lv, S. Huang and X. Ma, *Engineering*, 2024, **35**, 104–114.

308 M. A. Kipnis, R. S. Galkin, E. A. Volnina, I. A. Belostotskii, G. N. Bondarenko and O. V. Arapova, *Kinet. Catal.*, 2023, **64**, 849–861.

309 F. Xu, Z. Hong, J. Lv, C. Chen, G. Zhao, L. Miao, W. Yang and Z. Zhu, *Appl. Catal., A*, 2022, **648**, 118928.

310 Z. P. Hu, G. Qin, J. Han, W. Zhang, N. Wang, Y. Zheng, Q. Jiang, T. Ji, Z. Y. Yuan, J. Xiao, Y. Wei and Z. Liu, *J. Am. Chem. Soc.*, 2022, **144**, 12127–12137.

311 H. Bai, M. Ma, B. Bai, L. Bai, Y. Bai, J. Zuo, V. Vinokurov and W. Huang, *Fuel*, 2022, **310**, 122225.

312 R. Poreddy, S. Mossin, A. D. Jensen and A. Riisager, *Catalysts*, 2021, **11**, 696.

313 P. Zhao, W. Qian, H. Ma, H. Sheng, H. Zhang and W. Ying, *Catal. Lett.*, 2021, **151**, 940–954.

314 C. Dong, Y. Liu, Y. Xia, H. Liu, Y. Zhang, S. Huang and X. Ma, *Catalysts*, 2023, **13**, 1049.

315 X. Wang, S. Liu, H. Wang, Y. Liu, Y. Zhang, R. Li, C. Yu, K. Ren and P. Yang, *RSC Adv.*, 2024, **14**, 4734–4741.

316 F. Chen, X. Feng, P. Deng, L. Zhang, J. Zhao, Y. Wang, B. Tao, X. Zhao, J. Cao and H. Bai, *Chem. Eng. J.*, 2024, **498**, 155451.

317 K. Cao, W. Chen, D. Fan, Z. Jia, N. Chen, D. Zhu, S. Xu, A. Zheng, P. Tian and Z. Liu, *Chem. Eng. J.*, 2024, **487**, 150344.

318 W. Liu, Y. Wang, L. Bu, Y. Zhi, Z. Wang, M. Yang, K. Chu, Y. Huang, N. Guo and L. Qu, *ACS Appl. Nano Mater.*, 2023, **6**, 18005–18015.

319 F. Chen, X. Feng, J. Zhao, Z. He, L. Zhang, Y. Wang, P. Deng, X.-H. Gao, X.-Y. Zhao and J. Cao, *Chem. Eng. Sci.*, 2023, **282**, 119250.

320 X. Zhang, K. Cai, Y. Li, J. Qi, Y. Wang, Y. Liu, M.-Y. Wang, S. Huang and X. Ma, *Chin. J. Catal.*, 2024, **61**, 301–311.

321 X. Liu, S. Huang, Y. Liu, H. Liu, X. Zhang, J. Lv, J. Qi, Y. Wang, S. Wang and X. Ma, *Chem. Eng. Sci.*, 2024, **297**, 120247.

322 Y. Jiang, A. Hao, E. Zhan, P. Beato, S. Chen, F. Fan and C. Li, *Chem. Commun.*, 2024, **60**, 5727–5730.

323 J. Fan, J. Yao, X. Feng, C. Wang, Y. Shi, H. Feng, W. Gao, Y. He, X. Guo, S. Yasuda, G. Yang and N. Tsubaki, *Chem Bio Eng.*, 2024, **1**, 141–149.

324 H. S. Jung, J. Kim, C. Park, W. B. Lee and J. W. Bae, *Chem. Eng. J.*, 2024, **481**, 148657.

325 X. Feng, J. Cao, C. Su, Z. He and X. Zhao, *Fuel*, 2022, **315**, 123267.

326 A. Alberti, P. Davoli and G. Vezzalini, *Z. Kristallogr. – Cryst. Mater.*, 1986, **175**, 249–256.

327 A. Zheng, S. Li, S.-B. Liu and F. Deng, *Acc. Chem. Res.*, 2016, **49**, 655–663.

328 A. Zheng, S.-B. Liu and F. Deng, *Chem. Rev.*, 2017, **117**, 12475–12531.

329 X. Yi, Y. Xiao, G. Li, Z. Liu, W. Chen, S.-B. Liu and A. Zheng, *Chem. Mater.*, 2020, **32**, 1332–1342.

330 R. Liu, B. Fan, W. Zhang, L. Wang, L. Qi, Y. Wang, S. Xu, Z. Yu, Y. Wei and Z. Liu, *Angew. Chem., Int. Ed.*, 2022, **134**, e202116990.

331 A. Martucci, G. Cruciani, A. Alberti, C. Ritter, P. Ciambelli and M. Rapacciuolo, *Microporous Mesoporous Mater.*, 2000, **35**, 405–412.

332 H. Huo, L. Peng, Z. Gan and C. P. Grey, *J. Am. Chem. Soc.*, 2012, **134**, 9708–9720.

333 M. Boronat, C. Martínez and A. Corma, *Phys. Chem. Chem. Phys.*, 2011, **13**, 2603–2612.

334 M. Ravi, V. L. Sushkevich and J. A. V. Bokhoven, *Chem. Sci.*, 2021, **12**, 4094–4103.

335 X. Ding, C. Liu, J. Niu, N. Chen, S. Xu, Y. Wei and Z. Liu, *Chin. J. Struct. Chem.*, 2024, **43**, 100247.

336 H. Xue, X. Huang, E. Zhan, M. Ma and W. Shen, *Catal. Commun.*, 2013, **37**, 75–79.

337 A. Zecchina, F. Geobaldo, G. Spoto, S. Bordiga, G. Ricchiardi, R. Buzzoni and G. Petrini, *J. Phys. Chem.*, 1996, **100**, 16584–16599.

338 S. Liu, H. Liu, X. Ma, Y. Liu, W. Zhu and Z. Liu, *Catal. Sci. Technol.*, 2020, **10**, 4663–4672.

339 W. Fang, C. Wang, Z. Liu, L. Wang, L. Liu, H. Li, S. Xu, A. Zheng, X. Qin, L. Liu and F.-S. Xiao, *Science*, 2022, **377**, 406–410.

340 N. Chen, J. Zhang, Y. Gu, W. Zhang, K. Cao, W. Cui, S. Xu, D. Fan, P. Tian and Z. Liu, *J. Mater. Chem. A*, 2022, **10**, 8334–8343.

341 Y. Li, M. Yu, K. Cai, M. Wang, J. Lv, R. F. Howe, S. Huang and X. Ma, *Phys. Chem. Chem. Phys.*, 2020, **22**, 11374–11381.

342 L. Li, Q. Wang, H. Liu, T. Sun, D. Fan, M. Yang, P. Tian and Z. Liu, *ACS Appl. Mater. Interfaces*, 2018, **10**, 32239–32246.

343 L. Chen, Y. Wang, J. Lv and W. Yang, *Chem. Res. Chin. Univ.*, 2025, **41**, 59–65.

344 Y. Liu, S. Liu, X. Wang, H. Wang, R. Li, C. Yu, C. Xu, Y. Liu, Z. Xie, Y. Wang and P. Tang, *Chin. J. Chem. Eng.*, 2024, **66**, 216–223.

345 F. Chen, X. Feng, L. Zhang, J. Zhao, Z. He, F.-J. Yi, X. Zhao and J. Cao, *Chem. Eng. Sci.*, 2022, **263**, 118110.

346 W. Liu, Y. Wang, C. Sun, J. Lu, S. Wu, M. Shi, L. Bu, Z. Wang, Y. Zhi and M. Yang, *Mater. Chem. Phys.*, 2022, **292**, 126823.

347 P. He, J. Wang, Y. Li, S. Huang, M.-Y. Wang, Y. Wang, J. Lv and X. Ma, *Ind. Eng. Chem. Res.*, 2021, **60**, 8085–8093.

348 J. Yao, X. Feng, J. Fan, Y. He, R. Kosol, Y. Zeng, G. Liu, Q. Ma, G. Yang and N. Tsubaki, *Microporous Mesoporous Mater.*, 2020, **306**, 110431.

349 X. Huang, M. Ma, M. Li and W. Shen, *Catal. Sci. Technol.*, 2020, **10**, 7280–7290.

350 X. Wang, R. Li, C. Yu, Y. Liu, L. Liu, C. Xu, H. Zhou and C. Lu, *Ind. Eng. Chem. Res.*, 2019, **58**, 18065–18072.

351 X. Wang, R. Li, C. Yu and Y. Liu, *Microporous Mesoporous Mater.*, 2021, **311**, 110665.

352 R. Liu, S. Zeng, T. Sun, S. Xu, Z. Yu, Y. Wei and Z. Liu, *ACS Catal.*, 2022, **12**, 4491–4500.

353 F. Xu, J. Zheng, J. Li and Z. Zhu, *iScience*, 2025, **28**, 112102.

354 P. Lu, W. Yu, K. Wang, X. Wu, W. Zhang, C. Xing, Q. Wei, Y. Wang and C. Du, *Fuel*, 2024, **376**, 132714.

355 X. Wang, Y. Liu, Y. Liu, H. Wang, R. Li, C. Yu, K. Ren and C. Xu, *Microporous Mesoporous Mater.*, 2024, **370**, 113052.

356 A. A. Reule, J. A. Sawada and N. Semagina, *J. Catal.*, 2017, **349**, 98–109.

357 M. Wang, S. Huang, J. Lü, Z. Cheng, Y. Li, S. Wang and X. Ma, *Chin. J. Catal.*, 2016, **37**, 1530–1537.

358 F. Xu, J. Lv, C. Chen, Z. Hong, G. Zhao, L. Miao, W. Yang and Z. Zhu, *Ind. Eng. Chem. Res.*, 2022, **61**, 1258–1266.

359 N. Zhao, Y. Tian, L. Zhang, Q. Cheng, S. Lyu, T. Ding, Z. Hu, X. Ma and X. Li, *Chin. J. Catal.*, 2019, **40**, 895–904.

360 K. Cao, D. Fan, L. Li, B. Fan, L. Wang, D. Zhu, Q. Wang, P. Tian and Z. Liu, *ACS Catal.*, 2020, **10**, 3372–3380.

361 R. Liu, B. Fan, Y. Zhi, C. Liu, S. Xu, Z. Yu and Z. Liu, *Angew. Chem., Int. Ed.*, 2022, **61**, e202210658.

362 E. Dib, T. Mineva, E. Veron, V. Sarou-Kanian, F. Fayon and B. Alonso, *J. Phys. Chem. Lett.*, 2018, **9**, 19–24.

363 R. E. Fletcher, S. Ling and B. Slater, *Chem. Sci.*, 2017, **8**, 7483–7491.

364 G. Li, C. Foo, R. Fan, M. Zheng, Q. Wang, Y. Chu, J. Li, S. Day, P. Steadman, C. Tang, T. W. B. Lo, F. Deng and S. C. E. Tsang, *Science*, 2025, **387**, 388–393.

365 J. Ye, N. Dimitratos, L. M. Rossi, N. Thonemann, A. M. Beale and R. Wojcieszak, *Science*, 2025, **387**, eadn9388.

366 J. Zhong, X. Yang, Z. Wu, B. Liang, Y. Huang and T. Zhang, *Chem. Soc. Rev.*, 2020, **49**, 1385–1413.

367 F. Marques Mota and D. H. Kim, *Chem. Soc. Rev.*, 2019, **48**, 205–259.

368 S. Navarro-Jaén, M. Virginie, J. Bonin, M. Robert, R. Wojcieszak and A. Y. Khodakov, *Nat. Rev. Chem.*, 2021, **5**, 564–579.

369 J. Xie and U. Olsbye, *Chem. Rev.*, 2023, **123**, 11775–11816.

370 H. Wang, F. Jiao, Y. Ding, W. Liu, Z. Xu, X. Pan and X. Bao, *Natl. Sci. Rev.*, 2022, **9**, nwac146.

371 X. Yu, Y. Cheng, Y. Li, F. Polo-Garzon, J. Liu, E. Mamontov, M. Li, D. Lennon, S. F. Parker, A. J. Ramirez-Cuesta and Z. Wu, *Chem. Rev.*, 2023, **123**, 8638–8700.

372 W. Wen, S. Yu, C. Zhou, H. Ma, Z. Zhou, C. Cao, J. Yang, M. Xu, F. Qi, G. Zhang and Y. Pan, *Angew. Chem., Int. Ed.*, 2020, **59**, 4873–4878.

373 X. Wang, S. Jiang, W. Hu, S. Ye, T. Wang, F. Wu, L. Yang, X. Li, G. Zhang, X. Chen, J. Jiang and Y. Luo, *J. Am. Chem. Soc.*, 2022, **144**, 16069–16076.

374 S. Ye, K. Zhong, J. Zhang, W. Hu, J. D. Hirst, G. Zhang, S. Mukamel and J. Jiang, *J. Am. Chem. Soc.*, 2020, **142**, 19071–19077.

375 J. Zhou, X. Li, D. Liu, F. Wang, T. Zhang, M. Ye and Z. Liu, *Front. Chem. Sci. Eng.*, 2024, **18**, 42.

376 M. Pirdashti, S. Curteanu, M. H. Kamangar, M. H. Hassim and M. A. Khatami, *Rev. Chem. Eng.*, 2013, **29**, 205–239.

377 L.-T. Zhu, X.-Z. Chen, B. Ouyang, W.-C. Yan, H. Lei, Z. Chen and Z.-H. Luo, *Ind. Eng. Chem. Res.*, 2022, **61**, 9901–9949.